Changes of air pollutant emissions in China during two clean air action periods derived from the newly developed Inversed Emission Inventory for Chinese Air Quality (CAQIEI)

Lei Kong[1,3], Xiao Tang[*,1,3], Zifa Wang[*,1,3,4], Jiang Zhu[1,2], Jianjun Li[5], Huangjian Wu[1,3], Qizhong Wu[6], Huansheng Chen[1,3], Lili Zhu[5], Wei Wang[5], Bing Liu[5], Qian Wang[7], Duohong Chen[8], Yuepeng Pan[1,3], Jie Li[1,3], Lin Wu[1,3], and Gregory R. Carmichael[9]

[1]State Key Laboratory of Atmospheric Boundary Layer Physics and Atmospheric Chemistry (LAPC), Institute of Atmospheric Physics, Chinese Academy of Sciences, Beijing 100029, China
[2]CAS-TWAS Center of Excellence for Climate and Environment Sciences (ICCES), Institute of Atmospheric Physics, Chinese Academy of Sciences, Beijing 100029, China
[3]College of Earth and Planetary Sciences, University of Chinese Academy of Sciences, Beijing 100049, China
[4]Center for Excellence in Regional Atmospheric Environment, Institute of Urban Environment, Chinese Academy of Sciences, Xiamen 361021, China
[5]China National Environmental Monitoring Centre, Beijing, 100012, China
[6] College of Global Change and Earth System Science, Faculty of Geographical Science, Beijing Normal University, Beijing 100875, China
[7]Shanghai Environmental Monitoring Centre, Shanghai, 200030, China
[8]Guangdong Ecological Environment Monitoring Centre, National Key Laboratory of Regional Air Quality Monitoring for Environmental Protection, Guangzhou 510308, China
[9]Center for Global and Regional Environmental Research, University of Iowa, Iowa City, IA 52242, USA

Correspondence to: Xiao Tang (tangxiao@mail.iap.ac.cn) and Zifa Wang (zifawang@mail.iap.ac.cn)

Abstract

A new long-term emission inventory called the Inversed Emission Inventory for Chinese Air Quality (CAQIEI) was developed in this study by assimilating surface observations from the China National Environmental Monitoring Centre (CNEMC) using the ensemble Kalman filter and the Nested Air Quality Prediction Modeling System. This inventory contains the constrained monthly emissions of NO_x, SO_2, CO, primary $PM_{2.5}$, primary PM_{10}, and NMVOCs in China from 2013 to 2020, with a horizontal resolution of 15 km × 15 km. This paper documents detailed descriptions of the assimilation system and the evaluation results for the emission inventory. The results suggest that CAQIEI can effectively reduce the biases in the *a priori* emission inventory, with the normalized mean biases ranging from −9.1% to 9.5% in the *a posteriori* simulation, which are significantly reduced from the biases in the *a priori* simulations (−45.6% to 93.8%). The calculated RMSE (0.3 mg/m^3 for CO and 9.4–21.1 μg/m^3 for other species, on the monthly scale) and correlation coefficients (0.76–0.94) were also improved from the *a priori* simulations, demonstrating good performance of the data assimilation system. Based on CAQIEI, we estimated China's total emissions (including both natural and anthropogenic emissions) of the 6 species in 2015 to be as follows: 25.2 Tg of NO_x, 17.8 Tg of SO_2, 465.4 Tg of CO, 15.0 Tg of $PM_{2.5}$, 40.1 Tg of PM_{10}, and 46.0 Tg of NMVOCs. From 2015 to 2020, the total emissions reduced by 54.1% for SO_2, 44.4% for $PM_{2.5}$, 33.6% for PM_{10}, 35.7% for CO, and 15.1% for NO_x, but increased by 21.0% for NMVOCs. It is also estimated that the emission reductions were larger during 2018–2020 (from -26.6% to -4.5%) than during 2015–2017 (from -23.8% to 27.6%) for most species. Particularly, the total Chinese NO_x and NMVOC emissions were shown to increase during 2015–2017, especially over the Fenwei Plain area (FW) where the emissions of particulate matter (PM) also increased. The situation changed during 2018–2020 when the upward trends were contained and reversed to downward trends for both the total emissions of NO_x and NMVOC, and the PM emissions over FW. This suggests that the emission control policies may be improved in 2018–2020 action plan. We also compared the CAQIEI with other air pollutant emission inventories in China, which verified our inversion results in terms of total emissions of NO_x, SO_2 and NMVOCs, and more importantly identified the potential uncertainties in current emission inventories. Firstly, the CAQIEI suggested higher CO emissions in China, with CO emissions estimated by CAQIEI (426.8 Tg) being more than twice the

45 amount in previous inventories (120.7–237.7 Tg). Significantly higher emissions were also suggested over the western and

46 northeastern China for other air pollutants. Secondly, the CAQIEI suggested higher NMVOC emissions than previous emission

47 inventories by about 30.4–81.4% over the North China Plain (NCP) but suggested lower NMVOC emissions by about 27.6–

48 0.0% over the Southeast China (SE). Thirdly, the CAQIEI suggested smaller emission reduction rates during 2015–2018 than

49 previous emission inventories for most species except of CO. Particularly, China's NMVOC emissions were shown to have

50 increased by 26.6% from 2015 to 2018, especially over the NCP (by 38.0%), northeast China (by 38.3%), and central China

51 (60.0%). These results provide us with new insight into the complex variations of the air pollutant emissions in China during

52 two recent clean air actions, which has the potential to improve our understanding of air pollutant emissions in China and their

53 impacts on air quality. The whole datasets are available at https://doi.org/10.57760/sciencedb.13151 (Kong et al., 2023).

54 **1 Introduction**

55   Air pollution is a serious environmental issue owing to its substantial impacts on human health, ecosystems, and climate

56 change (Von Schneidemesser et al., 2015; Cohen et al., 2017; Bobbink et al., 1998). According to the World Health

57 Organization, air pollution–induced strokes, lung cancer, and heart disease are causing millions of premature deaths worldwide

58 every year (WHO, 2016). The fine particulate matter ($PM_{2.5}$) in the atmosphere not only degrades visibility but also affects the

59 radiative forcing of the climate, both directly and indirectly (Martin et al., 2004). After removal from the atmosphere through

60 dry and wet deposition, air pollutants such as sulfur, nitrate, and ammonium contribute significantly to soil acidification,

61 eutrophication, and even biodiversity reduction (Krupa, 2003; Hernández et al., 2016).

62   China has experienced severe $PM_{2.5}$ pollution in recent decades, due to its large emissions of air pollutants associated

63 with rapid urbanization and high consumption of fossil fuels (Kan et al., 2012; Song et al., 2017). The annual concentrations

64 of $PM_{2.5}$ in 2013 reached 106, 67 and 47 $\mu g/m^3$ over the Beijing–Tianjin–Heibei, Yangtze River Delta, and Peral River Delta

65 region, respectively, which were all higher than China's national standard (35 $\mu g/m^3$), and 5–10 times higher than that of the

66 World Health Organization (10 $\mu g/m^3$). To tackle this problem, strict emission control policies (so-called "clean air action

67 plans") have been proposed by China's government, including the "Action Plan on the Prevention and Control of Air Pollution"

68 from 2013 to 2017 (hereinafter called the "2013–2017 action plan"), and the "Three-year Action Plan for Winning the Bule

69 Sky War" from 2018–2020 (hereinafter called the "2018–2020 action plan"). With the successful implementation of these two

70 action plans, the air quality was substantially improved in China, as evidenced in both observational and reanalysis datasets

71 (Li et al., 2020b; Zheng et al., 2017; Krotkov et al., 2016; Zhong et al., 2021; Li et al., 2017a; Kong et al., 2021). However,

72 with the deepening of air pollution control, unexpected changes have occurred in China, bringing about new challenges for the

73 mitigation of air pollution in the future. On the one hand, despite a significant decline in $PM_{2.5}$ concentrations in China, severe

74 haze still occasionally occurs during the wintertime (Zhou et al., 2022b; Li et al., 2017c). In addition, field measurements in

75 cities over different regions of China consistently show different responses of aerosol chemical compositions to the emission

76 control policies (Tang et al., 2021; Zhou et al., 2019; Wang et al., 2022; Zhang et al., 2020; Li et al., 2019a; Xu et al., 2019b;

77 Lei et al., 2021; Zhou et al., 2022a). Compared with other aerosol species that showed substantial decreases during the clean

78 air action plans, nitrate has shown a weaker response to the control measures, remaining at high levels and in some cases

79 having even increased slightly. As a result, nitrate is playing an increasingly important role in heavy haze episodes in winter,

80 and dominates the chemical composition of $PM_{2.5}$ (Fu et al., 2020; Xu et al., 2019a), leading to a rapid transition from sulphate-

81 to nitrate-driven aerosol pollution (Li et al., 2019a; Wang et al., 2019b). On the other hand, photochemical pollution has

82 deteriorated in China, with ozone (O_3) concentrations having increased substantially in eastern China during 2013–2017 (Li et

83 al., 2019b; Lu et al., 2018; Lu et al., 2020; Wang et al., 2020b).

84   These unexpected changes have raised considerable concern among the scientific community and policymakers regarding

85 the overall effects of the clean air action plans, and how to coordinate the control of $PM_{2.5}$ and O_3 pollution. Addressing this

86 problem requires a comprehensive understanding of the effects of the clean air action plans on the emissions of different air
87 pollutants. In this respect, previous studies have compiled several long-term air pollutant emission inventories in China using
88 the bottom-up approach – for example, the Multi-resolution Emission Inventory for China (MEIC) developed by Tsinghua
89 University for 2010–2020 (Zheng et al., 2018); the Air Benefit and Cost and Attainment Assessment System-Emission
90 Inventory version 2.0 (ABaCAS-EI v2.0) developed by Tsinghua University for 2005–2021 (Li et al., 2023); the Regional
91 Emission Inventory in Asia (REAS) for 1950–2015 developed by Kurokawa and Ohara (2020); the Emissions Database for
92 Global Atmospheric Research (EDGAR) for 1970–2018 developed by Jalkanen et al. (2012); the Hemispheric Transport of
93 Air Pollution (HTAP) Inventory for 2000–2018 developed by Crippa et al. (2023); and the Community Emissions Data System
94 (CEDS) Inventory for 1970–2019 developed by Mcduffie et al. (2020). These emission inventories have provided the
95 community with important insights into the long-term changes in the air pollutant emissions in China, thus playing an
96 indispensable role in our understanding of the effects of the country's clean air action plans on emissions and air quality.
97 However, due to the lack of accurate activity data and emission factors, bottom-up emission inventories are subject to large
98 uncertainties, particularly during the clean air action periods when the activity data and emission factors changed considerably
99 and were difficult to track. Consequently, the estimated emission rates from different bottom-up emission inventories could
100 differ by more than a factor of 2 (Elguindi et al., 2020). For example, the estimated emissions for the year 2010 from different
101 bottom-up inventories were 104.9–194.5 Tg for carbon monoxide (CO), 15.6–25.4 Tg for nitrogen oxides (NO_x), 22.9–27.0
102 Tg for non-methane volatile organic compounds (NMVOCs), 15.7–35.5 Tg for sulfur dioxide (SO_2), 1.28–2.34 Tg for black
103 carbon (BC), and 2.78–4.66 Tg for organic carbon (OC), reflecting the large uncertainty in current bottom-up estimates of air
104 pollutant emissions in China, which hinders the proper assessment of the effects of the clean air action plans.

105   Inverse modeling of multiple air pollutant emissions (i.e., a top-down approach) provides an attractive way to constrain
106 bottom-up emissions by reducing the discrepancy between the model and observation through the use of data assimilation.
107 Numerous studies have confirmed the effectiveness of such a top-down method in verifying bottom-up emission estimates and
108 reducing their uncertainties (e.g., Elbern et al., 2007; Henze et al., 2009; Miyazaki and Eskes, 2013; Tang et al., 2013; Koohkan
109 et al., 2013; Koukouli et al., 2018; Jiang et al., 2017; Muller et al., 2018; Paulot et al., 2014; Qu et al., 2017. Based on long-
110 term satellite observations, the top-down method has also been used to track the long-term variations of emissions. For example,
111 Zheng et al. (2019) estimated the global emissions of CO for the period 2000–2017 based on a multi-species atmospheric
112 Bayesian inversion approach; Qu et al. (2019) constrained global SO_2 emissions for the period 2005–2017 by assimilating
113 satellite retrievals of SO_2 columns using a hybrid 4DVar/mass balance emission inversion method; by assimilating satellite
114 observations of multiple species, Miyazaki et al. (2020b) simultaneously estimated global emissions of CO, NO_x, and SO_2 for
115 the period 2005–2018; and, most recently, a regional top-down estimation of $PM_{2.5}$ emissions in China during 2016–2020 was
116 carried out by Peng et al. (2023) by assimilating surface observations. These studies provide us with valuable clues for
117 evaluating bottom-up emissions and improving our knowledge on the changes in emissions of different species in China during
118 the clean air action plans. However, most of these studies focused on emission trends at the global scale, which involved the
119 use of coarse model resolutions (>1°) that may be insufficient to capture the spatial variability of emission variations at the
120 regional scale. Meanwhile, current long-term, top-down estimates mainly focus on single species and do not fully cover the
121 two clean air action periods in China. Indeed, to date, there are still no long-term, top-down estimates of major air pollutant
122 emissions in China that fully cover the two clean air action periods.

123   In a previous study performed by our group, we developed a high-resolution air quality reanalysis dataset over China
124 (CAQRA) for the period 2013–2020 to track the air quality trends in China during the clean air action periods (Kong et al.,
125 2021). In the present study, as a follow up to this work, we constrained the long-term emission trends of major air pollutants
126 in China for 2013–2020 (which will be extended in the future on a yearly basis) by assimilating surface observations of air
127 pollutants from the China National Environmental Monitoring Centre (CNEMC) using an ensemble Kalman filter and the
128 Nested Air Quality Prediction and Forecasting System (NAQPMS). In the following sections, we present detailed descriptions

129 of the chemical data assimilation, the evaluation results of the inversed emission inventory, and the estimated emission trends

130 of different air pollutants in China during the clean air action periods.

2 The chemical data assimilation system

132   We used the chemical data assimilation system (ChemDAS) developed by the Institute of Atmospheric Physics, Chinese

133 Academy of Sciences, to constrain the long-term emission changes of different air pollutants in China, which was used in the

134 development of CAQRA in our previous work (Kong et al., 2021). Since the chemical transport model (CTM) and the

135 observations used in the top-down estimation were the same as those used in CAQRA, we only briefly describe these two

136 components in the following two subsections, instead concentrating on providing a fuller description (in the third subsection)

137 of the inversion scheme in ChemDAS.

2.1 Chemical transport model

139   The NAQPMS model was used as the forecast model to represent the atmospheric chemistry in this study, and the Weather

140 Research and Forecasting (WRF) model was used as the meteorological model to provide the meteorological input data.

141 NAQPMS contains comprehensive modules for the emission, diffusion, transportation, deposition, and chemistry processes in

142 the atmosphere, and has been used in previous inversion studies (Tang et al., 2013; Kong et al., 2019; Wu et al., 2020a; Kong

143 et al., 2023). Detailed configurations of the different modules used in NAQPMS are available in these publications.

144   Figure 1 shows the domain of the inverse model, which is the same as that used in CAQRA, with a fine-scale horizontal

145 resolution of 15 km. The HTAPv2.2 emission inventory was used as the a priori estimate of anthropogenic emissions in China,

146 which includes emissions from the energy, industry, transport, residential, agriculture, air and ship sectors with a base year of

147 2010 (Janssens-Maenhout et al., 2015). It is a harmonized global emission inventory that comprises of different regional

148 gridded inventories. Within the region of China, the air pollutant emissions were mainly provided by the MEIC emission

149 inventory (Janssens-Maenhout et al., 2015). The *a priori* estimates of emissions from other sources includes the biogenic

150 emissions obtained from the Monitoring Atmospheric Composition and Climate (MACC) project (Sindelarova et al., 2014);

151 biomass burning emissions obtained from the Global Fire Emissions Database (GFED), version 4 (Van Der Werf et al., 2010;

152 Randerson et al., 2017); soil and lightning NO_x emissions obtained from Yan et al. (2003) and Price et al. (1997); and marine

153 volatile organic compound emissions obtained from the POET database (Granier et al., 2005). The dust emissions were

154 calculated online in NAQPMS as a function of the relative humidity, frictional velocity, mineral particle size distribution, and

155 the surface roughness (Li et al., 2012), while the sea salt emissions were calculated using the scheme of Athanasopoulou et al.

156 (2008). Note that since we aimed to estimate the air pollutant emissions and their changes from the surface observation, we

157 did not consider the temporal variation in the *a priori* emission inventory. This would ensure that the top-down estimated

158 emission trends were only derived from the surface observations, without being influenced by the trends in the prior emission

159 inventory. In this way, our top-down estimation can serve as an independent estimation of the air pollutant emission changes

160 in China. Meanwhile, we used the constant diurnal variation of the emissions in this study due to the lack of information on

161 the diurnal variation of the emissions from different sectors, which is a potential limitation in our current work. However, since

162 the emission inversion was performed on the daily basis (Sect. 2.3.3), the diurnal variations of the emission may not

163 significantly influence the simulation results of the daily mean concentrations of air pollutants (less than 1 ppbv for SO_2, NO_2

164 and O_3) according to the sensitivity experiments conducted by Wang et al. (2010). The initial condition was treated as clean

165 air in NAQPMS, with a 2-week spin-up time. Top and boundary conditions were provided by the Model for Ozone and Related

166 Chemical Tracers (MOZART) (Brasseur et al., 1998; Hauglustaine et al., 1998) data products provided by National Center for

167 Atmospheric Research (NCAR). Note that since the MOZART data products were not available for years after 2018, the multi-

168 year average results from 2013 to 2017 were used for the simulations after 2018. Because most of the model boundaries were

4

169 set in the clean areas and are located at distance from China, we assumed that the differences in boundary conditions would
170 not significantly affect the modeling results over the China. To improve the performance of meteorological simulation, a 36-
171 h free run of the WRF model was conducted for each day by using the NCAR/NCEP 1°×1° reanalysis data. The simulation
172 results of the first 12 h were treated as the spin-up run, and the remaining 24 h were used to provide the meteorological inputs
173 for the NAQPMS model. The evaluation results for the WRF simulation are available in Text S1 in the Supplement, which
174 suggests acceptable performance of the WRF simulation for the inversion estimates (Table S1).

175 **2.2 Assimilated observations**

176   The assimilated observational dataset in this study was the same as that used in CAQRA, which includes surface
177 concentrations of $PM_{2.5}$, PM_{10} (coarse particulate matter), SO_2, NO_2 (nitrogen dioxide), CO, and O_3, from 2013 to 2020,
178 obtained from CNEMC (Fig. 1). Before the assimilation, outliers of the observations were filtered out by using an automatic
179 quality control method developed by Wu et al. (2018). Four types of outliers characterized by temporal and spatial
180 inconsistencies, instrument-induced low variances, periodic calibration exceptions, and lower PM_{10} concentrations than those
181 of $PM_{2.5}$, were filtered out to prevent adverse impacts on the inversion process. As estimated in Kong et al. (2021), about 1.5%
182 of observational data were filtered out after quality control, but further assessment showed that it had few effects on the average
183 concentrations of different species, which were estimated to be less than 1 $\mu g/m^3$ for the gaseous air pollutants and less than
184 5 $\mu g/m^3$ for the particulate matter. Estimation of observation error is also important for the inversion of emissions since the
185 observational error and background errors determine the degree of adjustment to the emissions. The observational error
186 comprises the measurement error and the representativeness error induced by the different spatial scales that the model and
187 observations represent. The estimations of these two components of observational error were the same as those used in CAQRA,
188 detailed descriptions of which are available in Kong et al. (2021).

189   It should be noted that the number of observation sites were not constant throughout the whole inversion period, being
190 approximately 510 in 2013 and then increasing to 1436 in 2015. According to Fig. S1, the observation sites were mainly
191 concentrated in the megacity clusters (e.g., North China Plain, Yangtze River Delta and Pearl River Delta) and the capital
192 cities of each province in 2013. The number of observation sites continued to increase across the China in 2014 and 2015. In
193 particular, many areas that were previously unobserved have added monitoring stations in 2014 and 2015, which significantly
194 increased the observation coverage of China and could lead to spurious trends in the top-down estimated emissions. Figure 2
195 shows the changes in the observational coverage over different regions of China from 2013 to 2020 indicated by the ratio of
196 areas that were influenced by observations to the total area of each region. It can be clearly seen that the observational coverage
197 increased from 2013 to 2015 with the expansion of the air quality monitoring network in China, and became stable after 2015.
198 However, the influence of the variation in the number of observation sites varied among different regions. Over the North
199 China Plain (NCP) region, the observational coverage was approximately 90% in 2013, and reached 100% in 2014, suggesting
200 that the variation in the observation sites may have little influence on the estimated emission changes there. A similar
201 conclusion can be drawn for the Southeast China (SE) region, where the observational coverage was about 75% in 2013 and
202 reached 100% in 2015. Elsewhere, in the other four regions, the influence of the variation in observation sites is expected to
203 be larger because of the low observational coverage in both 2013 and 2014. For example, the observational coverage over the
204 Northwest China (NW) region was less than 10% in 2013, but increased to about 60% in 2015. To better illustrate the impact
205 of changes in observational coverage on the inversions, a sensitivity analysis of the emission increments with the fixed
206 observation sites or varying observation sites is performed in this study (Text S2 and Fig. S2). It shows that the additional
207 emission increments caused by the increases of observation sites would weaken the decreasing trends estimated in the fixed-
208 site scenario for the emissions of $PM_{2.5}$, NO_x and NMVOC and even lead to increasing trends for the emissions of PM_{10} and
209 CO. In contrast, the increases of observation sites would enhance the decreasing trends of SO_2 estimated in the fixed-site
210 scenario. Such different behaviors are mainly related to the different sign of the emission increment of different species as we

illustrated in Text S2. These results highlighted the significant influences of the site differences on the estimated emissions and their trends, which should be noted by the potential users. Therefore, in order to reduce this influence on the estimated emission trends, in our following analysis we mainly analyze the emission trends after 2015, when the observational coverage had stabilized in all regions.

2.3 Data assimilation algorithm

We used the modified EnKF coupled with state augmentation method to constrain the long-term emissions of different air pollutants. EnKF is an advanced data assimilation method proposed by Evensen (1994) that features representing the background error covariance matrix with a stochastic ensemble of model realizations. Through the use of ensemble simulations, it has the ability to consider the indirect relationship between the emissions and chemical concentrations caused by the complex physical and chemical processes in the atmosphere. It also allows for the estimation of flow-dependent emission–concentration relationships that vary in time and space depending on the atmospheric conditions. The modified EnKF is an offline application of the EnKF method that works by decoupling the analysis step from the ensemble simulation, which has benefits in the reuse of costly ensemble simulations and makes high-resolution long-term inversion affordable (Wu et al., 2020a). In this method, the ensemble simulation was performed firstly with the perturbed emissions, and then the observations were assimilated to constrain the emissions (Wu et al., 2020a). The state augmentation method is a commonly used parameter estimation method (Tandeo et al., 2020) in which the air pollutant emissions are taken as the state variable and are updated according to the error covariance between the emissions and the concentrations of related species.

2.3.1 State variable and ensemble generations

The state variable used in this study was chosen following our previous multi-species inversion study (Kong et al., 2023), which included the scaling factors for the emissions of fine-mode unspeciated aerosol (PMF), coarse-mode unspeciated aerosol (PMC), BC, OC, NO_x, SO_2, CO, and NMVOC, as well as the chemical concentrations of $PM_{2.5}$, $PM_{10-2.5}$ (PM_{10} minus $PM_{2.5}$), NO_2, SO_2, CO, and daily maximum 8-h O_3 (MDA8h O_3), which are formulated as follows:

$$x = [c,\ \beta]^T, \tag{1}$$

$$c = [PM_{2.5}, PM_{10-2.5},\ NO_2,\ SO_2, CO,\ MDA8h\ O_3], \tag{2}$$

$$\beta = [\beta_{PMF},\ \beta_{PMC},\ \beta_{BC},\ \beta_{OC}, \beta_{NO_x}, \beta_{SO_2}, \beta_{CO}, \beta_{NMVOC}], \tag{3}$$

where x denotes the vector of the state variable, c denotes the vector of the chemical concentrations of different species, and β denotes the vector of the scaling factors for the emissions of different species. Note that although the chemical concentration variables are included in the state variable, they are not optimized simultaneously with the emission in the analysis step and are only used to estimate the covariance between the emission and concentrations. Detailed descriptions of the state variables are available in Table 1.

The ensemble of the scaling factors for different species was generated independently using the same method of Kong et al. (2021), which has a medium size of 50 and considers the uncertainties of major air pollutant emissions in China, including SO_2, NO_x, CO, NMVOCs, ammonia, PM_{10}, $PM_{2.5}$, BC, and OC. The uncertainties of these species were considered to be 12%, 31%, 70%, 68%, 53%, 132%, 130%, 208% and 258%, respectively according to the estimates of Li et al. (2017b) and Streets et al. (2003). Note that in this study we did not perturb the emissions of different sectors to reduce the degrees of freedom in the ill-posed inverse estimation problem. Instead, we only perturbed the total emissions of different species. Therefore, only the total emissions of different species were constrained in this study. The ensemble of the chemical concentrations was then generated through an ensemble simulation based on NAQPMS and the perturbed emissions calculated by multiplying the *a priori* emissions by the ensemble of the scaling factors. This treatment implicitly assumes that the uncertainty in the chemical concentration is mainly caused by the emission uncertainty. This makes sense on a monthly or yearly basis, considering that substantial changes in emissions are expected to have taken place during the clean air action plans, which are subject to large

252 uncertainty. However, the lack of consideration of other error sources, such as those of the meteorological simulation and the

253 model itself, may lead to underestimation of the background error covariance and emission adjustment, which is a potential

254 limitation of this study. In addition, the dust and sea salt emissions were not perturbed and constrained in this study, and thus

255 the errors in the simulated fine and coarse dust emissions would influence the inversion of $PM_{2.5}$ and PM_{10} emissions. As a

256 result, the top-down estimated $PM_{2.5}$ and PM_{10} emissions will contain errors in the simulated dust and sea salt emissions.

257 Particularly, we did not consider the emissions of coarse dust during the inversion process since there is large uncertainty in

258 the simulated coarse dust emissions by current dust emission schemes (Zeng et al., 2020; Kang et al., 2011). The large errors

259 in the simulated coarse dust concentration could significantly influence the inversion results of PM_{10} emissions. For example,

260 the simulated coarse dust concentration could sometimes be several orders of magnitude higher than the observed PM_{10}

261 concentration, leading to too low values of the inverse PM_{10} emissions (approximately 0) over the regions that were not the

262 typical dust source regions but were influenced by the transportation of coarse dust. Therefore, we only used simulated PM_{10}

263 concentrations from other sources in the inversion of PM_{10} emissions to avoid the influences of the too large errors in simulated.

264 This is also similar to assume that the coarse dust emission is equal to zero during the assimilation. However, in this way, the

265 top-down estimated PM_{10} emissions in this study would comprise all coarse dust emissions which should be noted by potential

266 users. A detailed description of the ensemble generation is available in Kong et al. (2021).

2.3.2 Inversion algorithm

268 We used a deterministic form of EnKF (DEnKF) proposed by Sakov and Oke (2008) to update the scaling factors of the

269 emissions of different species, which is formulated as follows:

270 $$\overline{x^a} = \overline{x^b} + \mathbf{K}(y^o - \mathbf{H}\overline{x^b}), \tag{4}$$

271 $$\mathbf{X^a} = \mathbf{X^b} - \frac{1}{2}\mathbf{KHX^b} \tag{5}$$

272 $$\mathbf{K} = \lambda \mathbf{B_e^b}\mathbf{H^T}(\mathbf{H}\lambda \mathbf{B_e^b}\mathbf{H^T} + \mathbf{R})^{-1}, \tag{6}$$

273 $$\mathbf{B_e^b} = \frac{1}{N-1}\sum_{i=1}^{N} X_i^b(X_i^b)^{\mathrm{T}}, \tag{7}$$

274 $$\overline{x^b} = \frac{1}{N}\sum_{i=1}^{N} x_i^b \,; X_i^b = x_i^b - \overline{x^b}, \tag{8}$$

275 where $\overline{x}$ denotes the ensemble mean of the state variable; the superscript **b** and *a* respectively denote the *a priori* and *a*

276 *posteriori* estimate; $\mathbf{X^a}$ is the analysed anomalies that can be used to calculate the uncertainty of the a posteriori emissions. $\mathbf{K}$

277 is the Kalman gain matrix; $\mathbf{B_e^b}$ is the background error covariance matrix calculated by the background perturbation $\mathbf{X^b}$; y^o is

278 the vector of the observation and $\mathbf{R}$ is the observation error covariance matrix; $\mathbf{H}$ is the linear observation operator, which

279 maps the model space to the observation space; λ is the inflation factor used to compensate for the underestimation of the

280 background error caused by the limited ensemble size and unaccounted error sources, which is calculated using the method of

281 Wang and Bishop (2003),

282 $$\lambda = \frac{(\mathbf{R}^{-1/2}d)^{\mathrm{T}}\mathbf{R}^{-1/2}d - p}{trace\{\mathbf{R}^{-1/2}\mathbf{H}\mathbf{B_e^b}(\mathbf{R}^{-1/2}\mathbf{H})^{\mathrm{T}}\}} \tag{9}$$

283 $$d = y^o - \mathbf{H}\overline{x^b} \tag{10}$$

284 where d is the observation innovation and p is the number of observations. Table S2 summarized the calculated average value

285 (standard deviation) of the used inflation factor for different species. It shows that the inflation factor over the east China

286 (including NCP and SE region) was generally round 1.0, suggesting that the original ensemble can well represent the simulation

287 errors of the different air pollutants over these regions. The inflation factor is larger over the western China (including SW,

288 NW and Central regions), especially for PM_{10} (36.0–78.1) and SO_2 (7.8–176.1), suggesting that the original ensemble may

289 underestimate the simulation errors of the air pollutants. This is associated with the large biases in the simulated air pollutant

290 concentrations over there and reflect that the emission uncertainties assumed in our studies may be underestimated over these

291 regions. This also highlighted the importance of the use of inflation method during the inversion, otherwise it would lead to

292 filter divergency caused by the underestimations of the background error covariance.

293   In order to reduce the influence of the spurious correlations on the performance of data assimilation, the EnKF was

294 performed locally in this study in that the analysis was calculated grid by grid with the assumption that only measurements

295 located within a certain distance (cutoff radius) from a grid point would influence the analysis results of this grid. The use of

296 this local analysis method also allowed the inflation factor to be calculated locally and to vary in time and space, which can

297 help characterize the spatiotemporal variations of errors as we illustrated above. Similar to in Kong et al. (2021) and Kong et

298 al. (2023), the cutoff radius was chosen as 180 km for each species based on the wind speed and the lifespan of the species

299 (Feng et al., 2020). The same local scheme with a buffer area was also employed during the inversion to alleviate the

300 discontinuities in the updated state caused by the cut-off radius. A detailed description of the local analysis scheme is available

301 in Kong et al. (2021).

302   Table 1 summarizes the corresponding relationships between the emissions and chemical concentrations. Similar to Ma

303 et al. (2019) and Miyazaki et al. (2012), we did not consider the inter-species correlation during the assimilation to prevent the

304 spurious correlations between non- or weakly related variables. In most cases, observations of one particular species were only

305 allowed to adjust the emissions of the same species. The assimilation of $PM_{2.5}$ mass observation was more complicated as

306 there are multiple error sources in the simulated mass concentrations of $PM_{2.5}$, not only from primary emission, but also from

307 secondary production. In this study, the $PM_{2.5}$ mass observation was used to constrain the emissions of PMF, BC and OC but

308 not used to constrain the emissions of its precursors to avoid the spurious correlations and nonlinear chemistry effects, which

309 is similar to the scheme used in Ma et al. (2019). This is feasible since the emissions of primary $PM_{2.5}$ (i.e., PMF, BC and OC)

310 and the emissions of $PM_{2.5}$ precursors (e.g., SO_2, NO_2) were perturbed independently in our method, thus the contributions of

311 primary $PM_{2.5}$ emission and the secondary $PM_{2.5}$ productions to the $PM_{2.5}$ mass could be isolated through the use of ensemble

312 simulations. Meanwhile, the use of iteration inversion method (which will be introduced later) can further reduce the influence

313 of the errors in the precursors' emissions on the inversion of primary $PM_{2.5}$ emission, because the errors of its precursors'

314 emission would be constrained by their own observations during the iterations. However, the lack of assimilation of speciated

315 $PM_{2.5}$ observations may lead to uncertainties in the estimated emissions of PMF, BC and OC, which is a potential limitation

316 in current work. For example, if the a priori simulated $PM_{2.5}$ equals the observations, the emissions of PMF, BC and OC would

317 not be adjusted by using the current method. However, in such cases, there may still be errors in the proportions of the emissions

318 of different $PM_{2.5}$ components. To adjust the emissions of PMC, we used the observations of $PM_{10-2.5}$ to avoid the potential

319 cross-correlations between $PM_{2.5}$ and PM_{10} (Peng et al., 2018; Ma et al., 2019). For the NO_x emissions, although the O_3

320 concentration are chemically related to the NO_x emissions, we did not use the O_3 concentrations to constrain the NO_x emission

321 in this study since there is nonlinear relationship between the O_3 concentration and NO_x emission which would lead to wrong

322 adjustment of NO_x emissions (Tang et al., 2016).

323   The inversion of NMVOC emission is more difficult than other species due to the lack of long-term nationwide NMVOC

324 observations and the strong chemical activity. Previous studies usually assimilated the satellite observations of formaldehyde

325 and glyoxal to constrain the NMVOC emissions, such as Cao et al. (2018) and Stavrakou et al. (2015). However, these

326 inversion studies are hindered by the NO_x-VOC-O_3 chemistry and the inherent uncertainty in the satellite observations of

327 formaldehyde and glyoxal. Considering the strong chemical relationship between the O_3 and NMVOC, some pioneer studies

328 have also explored the method of assimilating ground-level O_3 concentrations to constrain the NMVOC emissions (Ma et al.,

329 2019; Xing et al., 2020), and demonstrated the effectiveness of this approach. For example, Ma et al. (2019) found that the

330 assimilation of O_3 concentration could adjust the NMVOC emissions in the direction resembling the bottom-up inventories,

331 and the forecast skill of O_3 concentrations were also improved, indicating that the constrained NMVOC emissions are improved

332 relative to their a priori. Inspired by these studies, we have made an attempt to constrain the NMVOC emissions based on the

333 MDA8h O_3. The use of MDA8h O_3 rather than the daily mean O_3 concentration is to avoid the effects of the nighttime O_3

334 chemistry. For example, the simulation errors in the titration effects of NO_x may influence the simulated O_3 concentrations

335 during nighttime and affect the inversion results of NMVOC. An important issue that should be noted when using the MDA8h

336 O_3 to constrain the NMVOC emission is the nonlinear interactions among NO_x, NMVOC and O_3. On the one hand, the O_3

337 concentrations are dependent not only on the NMVOC emissions but also on the NO_x emissions. The errors in the a priori

338 emissions of NO_x would also contribute to the simulation errors of O_3, and deteriorate the inversion of NMVOC. The iteration

339 inversion scheme could help deal with this issue as the errors in the NO_x emissions will be constrained by the NO_2 observations

340 in the next iteration, which can reduce the influences of errors in the NO_x emission on the inversion of NMVOC emission

341 based on MDA8h O_3 concentrations. This is in fact similar to the approach used by Xing et al. (2020) who firstly constrained

342 the NO_x emissions based on observations of NO_2, and then constrained the NMVOC emissions based on O_3 concentrations.

343 Also, in Feng et al. (2024), the NO_2 observations were simultaneously assimilated to constrain the NO_x emissions to account

344 for the influences of errors in NO_x emissions on the NMVOC emissions, suggesting that the iteratively nonlinear joint inversion

345 of NO_x and NMVOCs is an effective way to address the intricate relationship among VOC-NO_x-O_3 (Feng et al., 2024).

346 Similarly, the errors in the CO emissions which may be significant according to our following analysis are also constrained in

347 a similar way to reduce the potential influences on the inversion of NMVOC emission. On the other hand, the emission

348 adjustments of NMVOC may exhibit bidirectionality dependent on the VOC-limited or NO_x-limited regimes. According to

349 Fig. 3, the NMVOC emissions were adjusted in alignment with the direction of the O_3 errors, suggesting a VOC-limited regime

350 over urban areas in China, given that the O_3 observation sites are predominantly situated in the urban areas. This agrees with

351 Ren et al. (2022) who diagnosed the NO_x-VOC-O_3 sensitivity based on the satellite retrievals and found that the VOC-limited

352 regimes are mainly located in the urban areas in China. This suggests that the relationship between the O_3 concentrations and

353 VOC emissions could be reasonably reflected by our inversion system, providing the feasibility in utilizing the O_3 observations

354 to constrain the VOC emissions. Note that due to the lack observations of the VOC components, we only optimize the gross

355 emissions of the VOC during the assimilation.

356 As we illustrated before, there exists nonlinear effects in the atmospheric chemistry which could influence the inversion

357 results of different species. In addition, since we did not consider the temporal variations in the *a priori* emissions, it was

358 expected that there would be significant biases in the *a priori* emissions for the years after 2013, as substantial changes in

359 emissions were expected owing to the implementation of strict emission control measures. Such bias in the *a priori* emissions

360 does not conform to the unbiased hypothesis of the EnKF, which could lead to incomplete adjustments of the *a priori* emissions

361 and degrade the performance of the data assimilation (Dee and Da Silva, 1998). To address these issues, an iteration inversion

362 scheme was employed in this study, which has been used previously in Kong et al. (2023). The main idea of the iteration

363 inversion scheme is to preserve the background perturbation $\mathbf{X^b}$ but to update the ensemble mean of the state variable $\overline{x^b}$ based

364 on the model simulations driven by the inversion results of the kth iteration. Therefore, a new single model simulation is

365 required to be conducted by using the a posteriori emission from the previous iteration as the input to update the ensemble

366 mean of the original ensemble. This enables the observational information and the adjusted emissions to be promptly

367 incorporated into the model, thereby providing feedback for the adjustments of emission in the next iteration. However, we

368 did not reassemble the ensemble simulation for each iteration due to the expensive computational cost of the ensemble

369 simulation. Therefore, in each iteration calculation, the ensemble perturbation that were used to calculate the background error

370 covariance matrix remains the same with only the ensemble mean being updated based on the inversion results of the previous

371 iteration. The state variable used in the $(k + 1)$th inversions is then formulated as follows:

372 $$x_i^{b,k+1} = \left[c^k + c_i^e - \overline{c^e}, \beta^k + \beta_i^e - \overline{\beta^e} \right]^T, \tag{11}$$

373 where c^k represents the model simulations driven by the inversed emissions of the kth iteration, c_i^e represents the ith member

374 of ensemble simulations with an ensemble mean of $\overline{c^e}$, β^k represents the updated scaling factors at the kth iteration, and

375 β_i^e represents the ith member of the ensemble of scaling factors with a mean value of $\overline{\beta^e}$. In each iteration, all emissions are

376 updated simultaneously and two rounds of iteration were conducted in this study based on our previous inversion study to

377 maintain a balance between the inversion performance and the computational cost of the long-term inversions (Kong et al.,
378 2023).

2.3.3 Setup of inversion estimation

380   Based on this inversion scheme, we constrained the daily emissions of PMF, PMC, BC, OC, NO_x, SO_2, CO, and NMVOCs,
381 from 2013 to 2020, based on the daily averaged observations of $PM_{2.5}$, $PM_{10-2.5}$, NO_2, CO, and MDA8h O_3. However, due the
382 lack of enough speciated $PM_{2.5}$ observation, the model performance driven by the inverse emission for the BC, OC and primary
383 unspeciated $PM_{2.5}$ have not been thoroughly evaluated. It is thus currently unclear for the quality of the inverse emissions of
384 BC, OC and primary unspeciated $PM_{2.5}$. Also, the lack of speciated $PM_{2.5}$ observations could lead to uncertainties in the
385 estimated emissions of PMF, BC, and OC as we mentioned before. Considering this, similar to in Kong et al. (2023), although
386 we made attempt to estimate the emissions of BC, OC and primary unspeciated $PM_{2.5}$, we have reservations about their
387 inversion results and only provide the emissions of $PM_{2.5}$ (PMC+BC+OC) and PM10 ($PM_{2.5}$ + PMC) in current stage. In future,
388 we will collect more speciated $PM_{2.5}$ observations to comprehensively quantify the accuracy of their inversion results, after
389 which the emissions of these species would be released. Meanwhile, the speciated $PM_{2.5}$ observations could be assimilated
390 under the current inversion framework. This could provide us with further constrains on the emissions of BC, OC and primary
391 $PM_{2.5}$. Meanwhile, as mentioned in subsection 2.3.1, the meteorological and model uncertainty were not considered in the
392 ensemble simulation. Thus, the errors in the meteorological simulation would cause fluctuations in the daily emissions that
393 contaminate the inversion results and are difficult to isolate from the inherent variations of emissions (Tang et al., 2013).
394 Considering this, the daily emissions were averaged to monthly values to reduce the influences of random model errors after
395 the assimilation.

3 Performance of the chemical data assimilation system

3.1 Analysis of OmF and emission increment

398   The observation-minus-forecast (OmF) and emission increment (*a posteriori* emission minus *a priori* emission) were
399 firstly analyzed to demonstrate the performance of the data assimilation. As shown in Fig. 3, the *a priori* simulation generally
400 underestimated the $PM_{2.5}$ concentrations over the NCP, SE and SW regions (positive OmF values) during 2013–2014, but
401 overestimated the $PM_{2.5}$ concentrations from 2016, reflecting the effects of the emission control measures during these years.
402 In the NE, NW and central China (hereafter, "Central") regions, obvious underestimation of the $PM_{2.5}$ concentration was found
403 (positive OmF values) throughout almost the entire assimilation period. Similarly, the OmF values of PM_{10} were positive
404 throughout the whole assimilation period over all regions of China. In contrast, the OmF values for SO_2 were negative for most
405 regions, and the negative OmF values over the NCP region became larger as the years progressed, which reflects the effects
406 of the emission control measures. The OmF for NO_2 reveals a seasonal variation over the NCP and SE regions, with negative
407 values during summer and positive values during winter, while there were obvious positive OmF values over the NE, SW, NW
408 and Central regions. In terms of CO, large positive OmF values were found over all regions of China, and there were decreasing
409 trends in the OmF values of CO over different regions of China associated with the emission control policies during these
410 years. The OmF values for O_3 were positive over most regions of China, except the NW region. These results provide us with
411 valuable information on the potential deficiencies in the *a priori* emissions. However, since our inversion method did not
412 differentiate between anthropogenic and natural emissions, the biases in the model simulation may also be attributable to the
413 errors in natural emissions such as dust, especially over the major dust-source areas of China (e.g., the NW and Central regions).
414 In addition, the effects of emission control were not considered in the *a priori* emissions, which is another important contributor
415 to the errors in the model simulation for the later years. Thus, the emission increments calculated by the assimilation should
416 reflect the combined effects of errors in the anthropogenic and natural emissions, as well as the emission control.

10

The calculated emission increments were consistent with the OmF values for all species, which indicates that the data assimilation method can probably constrain the emissions based on the observations. According to Fig. 3, the emission increments were positive for $PM_{2.5}$ over the NE, NW and Central regions, for NO_2 over the NE, SW, NW and Central regions, and for PM_{10}, CO and NMVOC over almost all regions throughout the assimilation period. In contrast, the emission increments were negative for the SO_2 emissions for most cases. Consistent with the OmF values, the emission increments were positive for $PM_{2.5}$ over the NCP, SE and SW regions during 2013–2014, but became negative from 2016 owing to the implementation of strict emission control measures. The emission increments for NO_x also showed significant seasonal variation over the NCP and SE regions, being positive during winter and negative during summer. The *a posteriori* biases for the model simulations of different species were also plotted to assess the performance of the data assimilation. It can be clearly seen that the biases were substantially reduced for all species, and the calculated root-mean-square error (RMSE) reduced by 23.2–52.8% for $PM_{2.5}$, 19.9–37.8% for PM_{10}, 36.4–77.3% for SO_2, 18.3–25.2% for NO_2, 29.9–40.5% for CO, and 4.4–26.1% for O_3 over the different regions of China, suggesting a good performance of the data assimilation system.

3.2 Evaluation of the inversion results

Table 2 shows the calculated evaluation statistics for the inversion at different temporal scales. It can be clearly seen that the model simulation with the *a posteriori* emission inventory reproduced well the magnitude and temporal variations of the different air pollutants in China, with calculated correlation coefficients of approximately 0.77, 0.72, 0.64, 0.67, 0.69 and 0.71, and normalized mean biases of approximately 4.5%, −4.6%, −9.0%, −3.9%, −8.8% and 9.5%, for the hourly concentrations of $PM_{2.5}$, PM_{10}, SO_2, NO_2, CO and O_3, respectively. Moreover, the *a posteriori* model simulation achieved comparable accuracy with the air quality reanalysis data we developed in Kong et al. (2021) in terms of the RMSE, which was 32.4 $\mu g \cdot m^{-3}$, 53.1 $\mu g \cdot m^{-3}$, 24.9 $\mu g \cdot m^{-3}$, 19.9 $\mu g \cdot m^{-3}$, 0.56 $mg \cdot m^{-3}$ and 34.9 $\mu g \cdot m^{-3}$, respectively, for these species at the hourly scale. At the daily, monthly and yearly scales, the constrained model simulation performed better, with RMSEs of about 9.1–20.0 $\mu g \cdot m^{-3}$ ($PM_{2.5}$), 18.5–31.6 $\mu g \cdot m^{-3}$ (PM_{10}), 11.5–16.0 $\mu g \cdot m^{-3}$ (SO_2), 8.1–12.8 $\mu g \cdot m^{-3}$ (NO_2), 0.28–0.39 $mg \cdot m^{-3}$ (CO), and 14.2–26.1 $\mu g \cdot m^{-3}$ (O_3), which were respectively reduced by 56.7–67.3%, 49.2–52.1%, 68.8–72.8%, 36.3–39.8%, 47.0–58.0%, and 22.9–30.5% compared to the RMSEs of the *a priori* simulations. We also compared the model performance driven by the inverse inventory with that driven by more recent bottom-up inventories (MEIC and HTAPv3) by taking the simulation results of year 2020 as an example to give us a more objective understanding of the accuracy of the inverse emission inventory. It shows that the inverse emission generally achieves better performance in simulating the air pollutant concentrations in China than the MEIC and HTAPv3 (Table S3). It is also encouraging to find that the model performance driven by CAQIEI and MEIC-HTAPv3 is similar for $PM_{2.5}$, PM_{10}, and SO_2 over the NCP, NE, SE and SW regions, both significantly improved from the a priori emission inventory. This suggest that both the top-down and recent bottom-up emission inventories have good performance in capturing the emission changes of these species over these regions and they yield consistent estimations. Detailed information on the configurations of the model simulation results driven by MEIC-HTAPv3 and the comparisons results are available in Text S3. All these validation results confirm the good performance of the data assimilation method and suggest that the inversed emissions inventory has the capability to reasonably represent the magnitude and long-term trends of the air pollutant emissions in China during 2013–2020.

4 Results

Based on the top-down estimation, the gridded emissions for $PM_{2.5}$, PM_{10}, SO_2, CO, NO_x and NMVOCs over China from 2013 to 2020 were developed into what we have called the Inversed Emissions Inventory for Chinese Air Quality (CAQIEI). In the following sections, we first analyze the magnitude and seasonality of the air pollutant emissions in China by taking 2015 as a reference year when the number of observation sites became stable. After that, the changes in emissions of different air

pollutants from 2015 to 2020 are analyzed and compared between the two clean air action plans in China. Note that due to the impacts of the changes in observation coverage, it is difficult to estimate the overall emission reduction rates during the 2013–2017 action plan by using our inversion results. The emission change rates during 2015–2017 were then sampled in this study to assess the mitigation effects during the 2013–2017 action plan and to be compared with the emission change rates during 2018–2020. Finally, CAQIEI is compared to the previous bottom-up and top-down emission inventories to validate our top-down estimation and identify the potential uncertainties in the current understanding of China's air pollutant emissions.

4.1 Top-down estimated Chinese air pollutant emissions in 2015

The top-down estimated emissions of different species in 2015 are as follows: 25.2 Tg of NO_x, 17.8 Tg of SO_2, 465.4 Tg of CO, 15.0 Tg of $PM_{2.5}$, 40.1 Tg of PM_{10}, and 46.0 Tg of NMVOCs. Note that these values not only contain anthropogenic emissions but also natural (e.g., dust and biogenic NMVOC) emissions. Thus, the top-down estimated emissions of PM and NMVOCs were higher than those estimated by previous studies, as we mention in following sections. Emission maps of all species in 2015 are shown in Fig. 4, and the calculated emissions of different species over different regions are presented in Table 3. According to Fig. 4, higher air pollutant emissions are widely distributed in the megacity clusters (e.g., NCP, Yangtze River Delta and Pearl River Delta) and the developed cities in China, reflecting the influences of human activities. NCP was the region with the largest emission intensity of air pollutants in China, contributing 5.1 Tg of NO_x, 3.5 Tg of SO_2, 82.2 Tg of CO, 2.7 Tg of $PM_{2.5}$, 8.7 Tg of PM_{10} and 9.0 Tg of NMVOCs to the total emissions in China. The inversion results also demonstrate the contribution of natural sources to the air pollutant emissions, such as the soil NO_x emissions and the biogenic NMVOC emission distributed in the Tibet Plateau region. In general, the majority of air pollutant emissions were located in eastern China (including the NCP, NE and SE regions), where the economy is relatively well developed, which in total accounted for 66.0% of NO_x, 60.9% of SO_2, 57.5% of CO, 60.4% of $PM_{2.5}$, 60.5% of PM_{10}, and 67.8% of NMVOC emissions in China. However, although the GDP of western China (including the SW, NW and Central regions) is less than one third that of eastern China, the top-down estimation indicates that the air pollutant emissions in western China could have accounted for about 32.2–42.5% of the total emissions, which reflects the low emission control levels over these regions.

Figure 5 shows the monthly variations of air pollutant emissions in China for year 2015. The monthly profile of NO_x emissions was relatively flat among the six species. SO_2 and CO showed higher emissions during wintertime because of the enhanced residential emissions associated with higher coal consumption for heating during that time of year. Meanwhile, the emission factor for CO from vehicles in winter was also higher than in other seasons, due to additional emissions from the cold-start process (Kurokawa et al., 2013; Li et al., 2017b). $PM_{2.5}$ and PM_{10} had higher emissions during winter and spring, which, on the one hand was due to the enhanced emissions from the residential and industrial sectors during wintertime (Li et al., 2017b), whilst on the other hand was due to the enhanced dust emissions during the spring season (Fan et al., 2021). Emissions of NMVOCs exhibited strong monthly variations, with higher emissions mainly in summer because of the enhanced NMVOC emissions from biogenic sources.

4.2 Top-down estimated emission changes of different air pollutants

4.2.1 Emission changes of particular matter

Figure 6 shows the top-down estimated emission changes of $PM_{2.5}$ and PM_{10} over China during two clean air action periods. Both $PM_{2.5}$ and PM_{10} emissions decreased substantially, by 44.3% and 21.2% respectively, from 2013 to 2020. On the contrary, the top-down estimates showed increases of $PM_{2.5}$ and PM_{10} emissions in 2014 and 2015, but this would be a spurious trend caused by the changes of observation sites as we discussed in Text S2. Therefore, the emissions in 2013 and 2014 were discarded to prevent the spurious trends. According to Fig. 6, the $PM_{2.5}$ emissions decreased by 14.5% from 2015

496 (15.0 Tg) to 2017 (12.8 Tg), and the reduction in emissions was roughly uniform throughout the period, which was about 8%
497 compared to previous years. The PM_{10} emissions showed a smaller reduction rate (−7.2%) than that of $PM_{2.5}$, decreasing from
498 40.1 Tg in 2015 to 37.2 Tg in 2017. Compared with the emission reduction rate during 2015–2017, both $PM_{2.5}$ and PM_{10}
499 showed larger emission reduction rates during 2018–2020, estimated to be 27.2% and 25.5%, respectively. The emission
500 reductions in each year were also larger, especially for PM_{10}. For example, $PM_{2.5}$ and PM_{10} emissions reduced by about 19.3%
501 and 14.0% in 2019 compared to 2018. This may have been due to that in addition to the strict controls imposed on the industrial
502 and power sectors during the 2013–2017 action period, the residential emissions have been strengthened during the 2018–
503 2020 action period. In particular, "coal-to-electricity" and "coal-to-gas" strategies were vigorously implemented in northern
504 China during the 2018–2020 action to reduce coal consumption and related air pollutant emissions (Liu et al., 2016; Wang et
505 al., 2020a). Thus, our inversion results confirm the effectiveness of the controls on residential emissions in terms of reducing
506 the emissions of $PM_{2.5}$ and PM_{10}. In addition, the control of non-point sources, such as blowing-dust emissions, was also
507 strengthened during the 2018–2020 action period, which is consistent with the faster reduction of PM_{10} emissions during 2018–
508 2020. The annual trends of $PM_{2.5}$ and PM_{10} emissions were also calculated in China using the Mann–Kendall trend test and
509 the Theil–Sen trend estimation method, the results of which are summarized in Table 4. The calculation of emission trends can
510 help extend the existing emission datasets forward in time to produce up-to-date products. The top-down estimated trends of
511 $PM_{2.5}$ and PM_{10} emissions were −1.4 and −2.6 Tg/year during 2015–2020, attributable to the strict emission control measures
512 imposed during the two clean air action plans. As mentioned, the decreasing trends were larger during 2018–2020 (−1.5 and
513 −4.6 Tg/year) than during 2015–2017 (−1.1 and −1.5 Tg/year).

514 　　　On the regional scale (Fig. S3), it can be clearly seen that the $PM_{2.5}$ emissions decreased consistently over all regions, by
515 59.8% in NCP, 49.6% in SE, 39.5% in NE, 35.8% in SW, 33.2% in NW, and 41.0% in Central, from 2015 to 2020. The NCP
516 region showed the largest reduction in emissions among the six regions, with its emission reduction rate being almost larger
517 than 10% in each year. This is consistent with the strictest emission control policies having been imposed over the NCP region.
518 The SE region showed a similar emission reductions to the NCP region, with its emission reduction rate being larger than 10%
519 in most years. Obvious increases of $PM_{2.5}$ emissions could be found over the NW region from 2013 to 2015 owing to the
520 increase in the number of observation sites in those years. After 2015, $PM_{2.5}$ emissions generally decreased over the NW region,
521 while there was a slight rebound in $PM_{2.5}$ emissions in 2016 and 2018, possibly due to the influences of the errors in fine dust
522 emission. The Central region showed different characteristics of emission changes to the other regions insofar as it showed
523 little change in $PM_{2.5}$ emissions during 2015–2018 but large reductions in 2019. This may be consistent with the control of
524 emissions over the Fenwei Plain area (the part of the Central region where the emission intensity is largest) being weak during
525 the 2013–2017 action plan but strengthened during the 2018–2020 action plan. In terms of the $PM_{2.5}$ emission trends over the
526 different regions, the calculated $PM_{2.5}$ emission trends were about −0.32 Tg/year in NCP, −0.32 Tg/year in SE, −0.24 Tg/year
527 in NE, −0.21 Tg/year in SW, −0.09 Tg/year in NW, and −0.15 Tg/year in Central, from 2015 to 2020.

528 　　　The changes of PM_{10} emissions were generally similar to those of $PM_{2.5}$, i.e., with decreases in all regions from 2015 to
529 2020 (Fig. S4). The top-down estimated PM_{10} emission reductions from 2015 to 2020 were about 3.5 Tg (40.0%) in NCP, 2.6
530 Tg (35.5%) in SE, 3.0 Tg (36.6%) in NE, 2.0 Tg (35.9%) in SW, 1.0 Tg (25.3%) in NW, and 1.3 Tg (21.6%) in Central; and
531 the calculated trends were about −0.64 Tg/yr, −0.52 Tg/yr, −0.51 Tg/yr, −0.40 Tg/yr, −0.20 Tg/yr, and −0.27 Tg/yr,
532 respectively. However, due to the influences of the changes in the number of observation sites, the PM_{10} emissions over the
533 NE, SW and NW regions increased substantially from 2013 to 2015, while they decreased in almost all years after 2015.
534 Different from the other regions, the Central region showed increases in PM_{10} emissions from 2015 to 2018, by about 0.92 Tg
535 (14.9%), but substantial decreases in 2019 and 2020. The result also shows that most PM_{10} emission reductions were achieved
536 during the 2018–2020 action plan. According to CAQIEI, the PM_{10} emissions decreased by 0.64–2.3 Tg (17.4–31.8%) from
537 2018 to 2020, which accounted for 48.4–169.0% of the total reduction in emissions from 2015 to 2020. This again emphasizes
538 the effectiveness of the control of blowing-dust emissions during the 2018–2020 action plan.

4.2.2 Emission changes of gaseous air pollutants

4.2.2.1 SO₂ and CO

Figure 7 shows the emission changes of different gaseous air pollutants in China from 2013 to 2020. Similar to the PM emissions, SO_2 and CO emissions decreased continuously during the two action plan periods, with top-down estimated emission reductions of about 9.6 Tg (54.1%) and 166.3 Tg (35.7%) for SO_2 and CO from 2015 to 2020, respectively. Meanwhile, both SO_2 and CO showed a significant decreasing trend from 2015 to 2020, with estimated trends of approximately −2.1 Tg/yr and −36.0 Tg/yr, respectively (Table 5). The reductions in SO_2 and CO emissions are closely consistent with the strict emission control measures imposed during the action plan periods, such as the phasing out of outdated industrial capacity and high-emitting factories, the strengthening of emission standards for industry and the power sector, the elimination of small coal-fired industrial boilers, and the replacement of coal with cleaner energies, which reflects the effectiveness of the emission control measures during the two action plan periods. Reductions of SO_2 emission were generally steady during the two action plan periods, which were approximately 4.2 Tg (23.8%) from 2015 to 2017 and 2.5 Tg (23.5%) from 2018 to 2020. However, CO showed a different emission reduction rate during the two action plan periods, with its emission reductions (67.1 Tg, 18.3%) during 2018–2020 being larger than those (45.6 Tg, 9.8%) during 2015–2017. This contrast may reflect the different emission control policies during the two clean air action periods, as well as the different emission distributions among the sectors between SO_2 and CO. According to the estimates of Zheng et al. (2018), the share of emissions from the industrial and power sector for SO_2 (77%) is nearly double that for CO (39%). Thus, the smaller reduction of CO emissions than that of SO_2 during 2015–2017 provides evidence that the 2013–2017 action plan mainly focused on controlling the emissions from the industrial and power sectors. During the 2018–2020 action plan, strict control measures targeted on the residential and transportation sectors were also implemented, which together account for 61% of CO emissions but only 23% of SO_2 emissions. As a result, CO showed a larger emission reduction rate during 2018–2020, while the emission reduction rate for SO_2 was similar to that during 2015–2017. The calculated trends of SO_2 and CO emissions during the two action plans are presented in Table 4, which are −2.1 Tg/yr and −1.3 Tg/yr for SO_2, and −22.8 Tg/yr and −33.5 Tg/yr for CO, respectively.

The reduction of SO_2 and CO emissions was also evident on the regional scale (Fig. S5 and S6). According to the top-down estimation, the reduction of SO_2 emissions ranged from 0.44 to 2.42 Tg (41.7–69.9%) from 2015 to 2020, with the NCP region exhibiting the largest reductions. The calculated decreasing trend of SO_2 emissions was also significant over all regions, ranging from −0.08 Tg/yr over the NW region to −0.57 Tg/yr over the NCP region (Table 5). With regards to the emission reduction rate during the different action plans, the results suggest that the emission reduction rate of SO_2 was higher during 2015 – 2017 (by 20.8–39.8%) than that during 2018–2020 (16.6–29.0%) over the NCP, SE, NE and SW regions. This may have been because, after the strict emission controls imposed upon industry and power plants during the 2013–2017 action plan, the room for further reductions in SO_2 emissions become smaller during the 2018–2020 action plan over these regions. Although residential and vehicle emissions were controlled more strictly during the 2018–2020 action plan, in total they account for ~20% of anthropogenic SO_2 emissions in China (Zheng et al., 2018). Thus, the enhanced reductions in SO_2 emissions from the residential and transportation sectors may not have been able to fully compensate for the weakened reductions from the industrial and power sectors, leading to a smaller SO_2 emission reduction rate over these regions. In contrast, the SO_2 emission reduction rate during 2018–2020 (31.1–34.8%) was higher than that during 2015–2017 (14.1–20.4%) over the NW and Central regions. This may have been due to the fact that the emission controls over the NW and Central regions were relatively weak during the 2013–2017 action plan (as also evidenced by the emission reduction rates of other species) owing to its less-developed economy. During the 2018–2020 action plan, the emission controls over these two regions were strengthened, which led to their higher emission reduction rates. Accordingly, the enhanced SO_2 emission reduction rates over the NW and Central regions compensated for the weakened reduction rates over the other regions, leading to a steady SO_2 emission reduction rate on the national scale.

14

581   The reductions of CO emissions from 2015 to 2020 were approximately 14.9–42.3 Tg (21.6–51.4%) over the different

582   regions of China, with significant decreasing trends ranging from −3.0 to −8.7 Tg/yr (Fig. S6 and Table 5). Consistent with

583   the comparisons of national CO emission reduction rates between the two action plans, the emission reduction rates during

584   2015–2017 (4.4–24.6%) were estimated to be smaller than those during 2018–2020 (12.2–24.6%) over all the different regions

585   except the Central region, where the CO emission reduction rate was similar during the two action plans (Fig. S6).

4.2.2.2 NO_x and NMVOCs

587   The top-down estimated NO_x and NMVOC emissions showed different changes to the other four species, by increasing

588   during 2015–2017 but declining during 2018–2020. Specifically, NO_x emissions increased slightly by 5.9% from 2015 (25.2

589   Tg) to 2017 (26.6 Tg), with a non-significant increasing trend of 0.74 Tg/yr. Then, NO_x emissions began to decrease in 2018,

590   with a top-down estimated emission reduction and calculated trend of approximately 3.1 Tg (12.7%) and −1.6 Tg/yr,

591   respectively, from 2018 to 2020. NMVOCs showed stronger emission increases than did NO_x, with top-down estimated

592   emission increases of approximately 12.7 Tg (27.6%) and a calculated emission trend of about 6.3 Tg/yr from 2015 to 2017.

593   Similar to NO_x, NMVOC emissions began to decrease after 2018, with a top-down estimated reduction of approximately 2.6

594   Tg (−4.4%) from 2018 to 2020, and a calculated trend of about −1.3 Tg/yr.

595   The increases of NO_x and NMVOC emissions during 2015–2017 suggest that the 2013–2017 action plan may not have

596   achieved desirable mitigation effects on these two species. For NO_x emissions, the upward trend may have been associated

597   with the following factors. On the one hand, vehicle exhaust is one of the most important sources of NO_x in China, accounting

598   for 31% of all NO_x emissions nationally (Zheng et al., 2018). From 2013 to 2017, the number of vehicles in China continued

599   to increase and reached 310 million in 2017, approximately 33.5% higher than in 2013 (MEE, 2017), which led to increases

600   of NO_x emissions from vehicles in China. On the other hand, although the 2013–2017 action plan was effective in reducing

601   the NO_x emissions from coal-fired power plants by promoting denitrification facilities and an ultra-low emission standard, the

602   mitigation impacts on industrial NO_x emissions may have been relatively small. For example, Wang et al. (2019a) compiled a

603   unit-based emissions inventory for China's iron and steel industry from 2010 to 2015, based on detailed survey results of

604   approximately 4900 production facilities in mainland China. They found that there were almost no NO_x control measures in

605   China's iron and steel industry during 2010–2015, resulting in a 12.4% increase in China's NO_x emissions from the iron and

606   steel industry in 2015 compared to 2010. In addition, although the penetration rate of denitrification facilities in China's cement

607   industry reached 92% in 2015, the actual operating rate of denitrification facilities in the cement industry was not desirable,

608   due to the lack of online emission monitoring systems. According to the research results of the Ministry of Ecology and

609   Environment, 800, 1300, and 1400 cement production kilns were equipped with selective non-catalytic denitrification facilities

610   from 2013 to 2015, but the actual operating rates were only 51%, 54% and 73%, respectively (Liu et al., 2021). In addition,

611   the new precalciner kilns used in the cement industry have a higher NO_x emission factor, such that the shift from traditional

612   vertical kilns to precalciner kilns has to some extent increased the cement industry's emissions of NO_x (Liu et al., 2021). Thus,

613   there is evidence that the mitigation effects of the industrial control measures on NO_x emissions may not be as significant as

614   expected. Overall, the increased number of vehicles may have offset the emission mitigation effects brought about by the

615   control of power plants, and the mitigation effects of controlling industrial NO_x emissions were also undesirable. Consequently,

616   NO_x emissions in China may not have decreased, and even increased slightly, during the 2013–2017 action plan. Figure S7

617   further shows the changes in NO_x emissions over different regions of China, revealing that NO_x emissions over the NCP, SE,

618   NE and SW regions were roughly unchanged (by less than 5%) from 2015 to 2017, while they increased over NW (18.6%)

619   and Central (17.5%). This is consistent with previous results and indicates that NO_x emissions may have increased over the

620   NW and Central regions, possibly due to their increased human activities and weak emission controls.

621   In terms of NMVOC emissions, since the inversion results did not differentiate between anthropogenic and biogenic

622   sources, the changes in NMVOC emissions may have been related to both anthropogenic and biogenic emissions. With respect

to anthropogenic emissions, previous bottom-up studies have suggested that China's NMVOC emissions did not decline during the 2013–2017 action plan, due to the lack of effective control measures on the chemical industry and solvent use (Zheng et al., 2018; Li et al., 2019c). According to the estimates of Li et al. (2019c), China's NMVOC emissions from solvent use increased by 11.1% in 2017 compared to those in 2015. Meanwhile, the increase in the number of vehicles in China may also have led to an increase in NMVOC emissions from transportation. Thus, the increases of NMVOC emission during 2015–2017 estimated by our inversion inventory may be related to the increases in anthropogenic NMVOC emissions from the chemical industry, solvent use, and vehicles. For the trends of biogenic NMVOC emissions, the CAMS global emission inventory shows that there were only little changes in the biogenic NMVOC emissions in China from 2013 to 2018 (Sect. 4.3.3), suggesting little contributions of the biogenic sources to the increased NMVOC emission in China. Figure S8 further shows the changes in NMVOC emissions over different regions of China, which suggests consistent increases in NMVOC emissions from 2015 to 2017 over different regions. According to the top-down estimations, NMVOC emissions increased by 30.5%, 25.2%, 18.5%, 10.9%, 50.5% and 63.1% over the NCP, SE, NE, SW, NW and Central regions, respectively. Again, the NW and Central regions exhibited the largest emission increases among the six regions, which is consistent with their elevated levels of human activity and weak emission controls.

The decrease in NO_x and NMVOC emissions after 2018 suggests that the emission control strategy of the Chinese government had reached a point of optimization. The 2018–2020 action plan not only strengthened the controls over the industrial and power sectors, but also the transportation sector, especially for diesel vehicles with high NO_x emissions. For example, the Chinese government released the "Action Plan for the Control of Diesel Trucks", and vigorously promoted an adjustment of the transportation structure of China by gradually improving the availability of rail transport. As a result, there was a downward trend in NO_x emissions in China. The top-down estimated reductions of NO_x emissions were approximately 0.81 Tg (17.2%) over NCP, 0.98 Tg (14.0%) over SE, 0.37 Tg (9.4%) over NE, 0.51 Tg (12.2%) over SW, 0.13 Tg (11.0%) over NW, and 0.32 Tg (9.2%) over Central (Fig. S7). The decrease in NMVOC emissions after 2018 may on the one hand have been related to the strengthening of vehicle controls during the 2018–2020 action plan, whilst on the other hand it may have been related to the promotion of clean heating plans in the northern region, which reduced the emissions of NMVOCs from residential sources. However, the decreases in NMVOC emissions were smaller than those in NO_x, which were estimated to be 0.84 Tg (6.9%) over NCP, 0.47 Tg (2.8%) over SE, 0.98 Tg (10.1%) over NE, and 0.53 Tg (14.1%) over NW (Fig. S6). Different from other regions, the NMVOC emissions over the SW and Central regions remained almost unchanged during the 2018–2020 action plan (Fig. S8).

4.2.3 Changes in the distribution pattern of emissions in China

Due to the different emission control intensities over the different regions of China, the emission distribution patterns of the different species may also have been altered, which could have influenced the distributions of air pollution in China. Based on CAQIEI, we further investigated the emission distribution patterns, as well as their changes, during the two action plans. Maps of the emission changes of different species during 2015–2017 and 2018–2020 are presented in Fig. 8. The shares of emissions in 2015, 2017 and 2020 by each subregion of China are also presented (Fig. 9). It can be seen that the emission changes during the 2015–2017 were more heterogenous than those during 2018–2020. The air pollutant emissions after the 2018–2020 action plan showed consistent reductions over most regions of China, while there were obvious emission increases detected from 2015 to 2017. This is consistent with the different emission control effects during the two clean air action plans as mentioned in previous sections. Due to its strictest emission control policies, the NCP region showed consistent emission reductions of SO_2, NO_x, CO, $PM_{2.5}$ and PM_{10} during the two clean air action plans. Accordingly, the shares of emissions in the NCP region continued to decrease during the two action plan periods (Fig. 9). For example, the share of SO_2 emissions in the NCP region decreased from 19.4% to 15.4% during the period of 2015–2017, and from 15.4% to 12.7% during the 2018–2020 action plan. In contrast, NMVOC emissions increased obviously over the NCP region from 2015 to 2017, and decreased during

665 2018–2020. However, its share did not change significantly, being roughly 20% throughout both periods. As for other regions,
666 increases of SO_2, NO_x, $PM_{2.5}$, PM_{10} and NMVOC emissions during 2015–2017 could be found over the Central region. More
667 specifically, the emission increases were mainly located in the Fenwei Plain area of the Central region, which was due to the
668 fact that this area was not included as a key region of emission controls during the 2013–2017 action plan. However, the
669 Fenwei Plain area was added as a key emission control region during the 2018–2020 action plan, which is consistent with the
670 emission reductions for these species over the Central region (Fig. 8). As a result, the shares of SO_2 and $PM_{2.5}$ emissions in the
671 Central region increased during 2015–2017 but decreased during 2018–2020 (Fig. 9). However, the shares of NO_x, PM_{10} and
672 NMVOC emissions continued to increase over the Central region during the two clean air action plans, which suggests larger
673 roles of air pollutant emissions in that region. In contrast, the share of CO emissions in the Central region continued to decrease
674 in the two action plans, from 17.7% in 2015 to 13.4% in 2020.

675 In terms of the shares of emissions in eastern and western China, the top-down estimation suggests an increased share of
676 NO_x, $PM_{2.5}$, PM_{10} and NMVOC emissions in western China after the two clean air action plans (Fig. 9), which indicates slower
677 emission reductions for these species in western China. However, the share of CO emissions in western China was reduced
678 after the two clean air action plans. Although the share of SO_2 emissions in western China increased during 2015–2017, it
679 turned to a decrease during 2018–2020.

4.3 Comparisons with different emission inventories

681 In this section, the CAQIEI is compared with the previous long-term bottom-up and top-down emission inventories in
682 China to validate our inversion results and provide the clues for the potential uncertainty in the current air pollutant emission
683 inventories. The bottom-up emission inventories used in the comparison include MEIC (Zheng et al., 2018), ABaCAS (Li et
684 al., 2023), HTAPv3 (Crippa et al., 2023), EDGARv6 (Jalkanen et al., 2012) and CEDS (Mcduffie et al., 2020), while the top-
685 down emission inventory is obtained from the updated Tropospheric Chemistry Reanalysis (TCR-2) (Miyazaki et al., 2020b).
686 However, it is difficult to directly compare our inversion results with these emission inventories considering that the inversion
687 emission includes both anthropogenic and natural emissions. To better compare our inversion results with previous inventories,
688 the natural emission sources, including soil NO_x emissions and biogenic emissions obtained from the CAMS global emission
689 inventory   (https://ads.atmosphere.copernicus.eu/cdsapp#!/dataset/cams-global-emission-inventories?tab=overview;   last
690 accessed 26 July 2023) and the biomass burning emissions obtained from the Global Fire Assimilation System (GFAS) (Kaiser
691 et al., 2012) are taken as a reference to account for the influences of natural sources. The CAMS and GFAS emission inventory
692 are used because they are state-of-art natural emission inventories and can provide us with independent long-term estimations
693 of natural emissions. Since the latest year of most emission inventories is 2018, the comparisons were conducted between 2015
694 and 2018. Note that due to the complexity in the estimations of natural sources, significant uncertainty exists in the estimated
695 natural emissions. As a result, the comparison results would be sensitive to the used natural emission inventories, especially
696 for the species with large amount of natural emission, such as the NMVOC and particulate matter. Therefore, it should be
697 aware of that the comparison conducted here and the derived implications are on the basis of the natural emissions estimated
698 by CAMS and GFAS. In addition, the natural dust emissions are not considered in the comparisons, which would influence
699 the comparisons of the PM emissions.

4.3.1 Magnitude

4.3.1.1 NO_x

702 Figure 10 shows the average emissions of different air pollutants in China during 2015–2018 obtained from CAQIEI and
703 the previous emission inventories plus the natural sources we considered. Comparisons of the emission estimations on the
704 regional scale and gridded scale are also presented (Fig. 11 and Fig. S9). The results show that the CAQIEI has slightly higher

705 NO$_x$ emissions in China than the other inventories. Considering that CAQIEI includes both anthropogenic and natural sources,

706 this discrepancy could be explained by the natural NO$_x$ sources. According to the estimations of CAMS and GFAS, the soil

707 and biomass-burning NO$_x$ emissions are approximately 1.9 and 0.08 Tg/yr, which explains well the higher NO$_x$ emissions

708 given by CAQIEI. After consideration of the natural sources, MEIC, HTAPv3 and EDGARv6 agree well with our inversion

709 results on the national scale, with their differences within 1.0–7.4%. The NO$_x$ emission estimated by ABaCAS, CEDS and

710 TCR-2 are slightly lower than CAQIEI and other emission inventories. However, the differences between CAQIEI and these

711 inventories were found to range from 15.9% to 21.3%, which is within the previous estimated uncertainties of NO$_x$ emissions

712 in China (Kurokawa and Ohara, 2020; Li et al., 2017b; Li et al., 2023). These results suggest that the total NO$_x$ emissions in

713 CAQIEI are generally consistent with the current estimations of the anthropogenic and natural NO$_x$ emissions in China. On

714 the regional scale, the top-down estimated NO$_x$ emissions show good agreement with the previous emission inventories over

715 the NCP and SE regions, with their differences ranging from 1.0%–26.8%, suggesting good consistency in the estimations of

716 NO$_x$ emissions over these two regions. This makes sense because NCP and SE are the two most developed regions in China,

717 and where surveys and research on emissions are most sufficient. The differences are larger over the other regions. In the NE

718 region, CAQIEI has higher NO$_x$ emissions than the other inventories by 5–70%, suggesting higher anthropogenic or biomass-

719 burning emissions over there. The estimations made by MEIC, CEDS and TRC-2 are closer to our estimates, with their

720 differences being approximately 5.4–23.3%, while the differences are larger for ABaCAS, HTAPv3 and EDGARv6 (36.7–

721 70.0%). Over the SW and Central regions, there are large diversity in the previous emission inventories with estimations by

722 HTAPv3 and EDGARv6 almost double those of MEIC, ABaCAS, CEDS and TCR-2. The CAQIEI suggests a midst estimation

723 which is within the range of previous emission inventories. In the NW region, CAQIEI is consistently higher than other

724 inventories, by 22.7–64.2%, which suggests a potential missing source of the NO$_x$ emissions over this region.

725 **4.3.1.2 SO$_2$**

726   For SO$_2$ emissions, since natural sources contribute little (only about 0.02 Tg/yr) to them in China, the discrepancies

727 between CAQIEI and previous emission inventories are mainly attributable to the differences in anthropogenic emissions. As

728 shown in Fig. 10, CAQIEI agrees well with HTAPv3 and CEDS on the national scale, with their differences being

729 approximately ±2%, but is higher than MEIC, ABaCAS and TCR-2 by 17.4–32.9%. In contrast, EDGARv6 may have a

730 positive bias in its estimated SO$_2$ emissions, which are roughly double those of CAQIEI and other inventories. On the regional

731 scale, our results agree well with MEIC, ABaCAS, HTAPv3, CEDS and TCR-2 over the NCP region, with their differences

732 ranging from 1.0 to 18.1%. In the SE region, CAQIEI suggest lower SO$_2$ emissions than previous emission inventories, except

733 TCR-2. The differences are relatively smaller for the MEIC and ABaCAS inventories by around −15%, but larger for HTAPv3,

734 EDGARv6 and CEDS (ranging from −47.3% to −113.2%). In contrast, CAQIEI suggests higher SO$_2$ emissions than all

735 previous emission inventories over the NE region by about 14.8–132.0%, indicating possible missing sources over there.

736 Similarly, the CAQIEI and HTAPv3 suggests higher SO$_2$ emissions than the MEIC, ABaCAS, CEDS and TCR-2 by 27.0–

737 75.6% in the NW region, and by 44.3–77.7% in the Central region.

738 **4.3.1.3 CO**

739   For CO emissions, CAQIEI is substantially higher than the previous emission inventories, with the estimated CO

740 emissions of CAQIEI being about three times higher than the bottom-up inventories and more than double those of the top-

741 down estimates made by TCR-2. According to GFAS, the average rate of CO biomass-burning emissions in China from 2015

742 to 2018 was about 3.4 Tg/yr. Yin et al. (2019), based on MODIS fire radiative energy data, also estimated China's CO biomass-

743 burning emissions to be about 5.0 (2.3–7.8) Tg/yr. The biogenic CO emissions obtained from the CAMS global emission

744 inventory were approximately 2.3 Tg/yr. According to these estimates, natural CO emissions in China have a magnitude of

745 about 10^1, which is rather small compared with anthropogenic sources, and cannot explain the large discrepancies between

746   CAQIEI and other inventories. Thus, the CAQIEI suggest much higher anthropogenic CO emissions in China than the existing

747   emission inventories. In fact, the potential underestimation of CO anthropogenic emissions has been investigated in previous

748   studies and is regarded as the main reason for the negative bias in global or hemispheric CO simulations (Stein et al., 2014;

749   Gaubert et al., 2020). Regionally, Kong et al. (2020) compared a suite of 13 modeling results from six different CTMs—

750   namely, NAQPMS, CMAQ, WRF-Chem, NU-WRF, NHM-Chem and GEOS-Chem—with observations over the NCP and

751   Pearl River Delta regions under the framework of the Model Inter-Comparison Study for Asia III (MICS-Asia III), and found

752   consistent negative biases in the CO simulations of all models, pointing toward potential underestimations of CO emissions in

753   China. Previous inversion studies have also reported higher a posteriori CO emissions than their *a priori* emission inventories

754   (Bergamaschi et al., 2000; Miyazaki et al., 2012; Petron et al., 2002; Petron et al., 2004; Tang et al., 2013; Gaubert et al., 2020).

755   For example, the constrained CO emissions reported by Gaubert et al. (2020) are 80% higher than the CEDS over the northern

756   China. Our inversion results are consistent with these inversion studies, suggesting higher anthropogenic CO emissions in

757   China. However, direct evidence in support of such high CO emissions in China reported by our study is still limited currently.

758   Thus, we compiled more inversion results within the period of 2013–2020 from previous studies to further validate our

759   inversion results, which are summarized in Table 6. It can be clearly seen that there are large differences in the estimated CO

760   emissions between the inversion results based on surface observations and those based on satellite data. Our inversion results

761   are consistent with the results of Feng et al. (2020), with China's CO emissions in December 2017 estimated at approximately

762   1500.0 kt/day and 1388.1 kt/day, respectively. In addition, Feng et al. (2020) used the CMAQ model to constrain CO emissions,

763   which is different from the model we used. This may indicate that the model uncertainty would not significantly influence the

764   inversion results of CO emissions. However, the top-down estimated CO emissions based on satellite data (163.6–553.4 kt/day)

765   are much lower than those based on surface observations, although they are all higher than their *a priori* emissions. The lower

766   CO emission estimations based on satellite data assimilation may be attributable to the lower sensitivities of satellite data to

767   surface concentrations, suggesting that the assimilation of satellite data alone may not be adequate to correct the negative

768   biases in the *a priori* emissions. This deficiency has also been revealed by Miyazaki et al. (2020b), who found undercorrected

769   surface CO emissions in the extratropic of the Northern Hemisphere in TCR-2. However, the assimilation of surface

770   observations can be influenced by the uncertainties in the modeled vertical mixing, which could lead to the uncertainties in the

771   inversed CO emissions based on surface observations. Therefore, the inversed CO emissions in CAQIEI could be partly

772   supported by previous inversion studies based on surface observations, but more evidence is still needed to justify the

773   magnitude of the inversed CO emissions. Besides anthropogenic sources, the chemical production of CO via oxidation of

774   methane (CH_4) and NMVOCs, as well as the CO sinks via the hydroxyl radical (OH) reaction, also influence the simulation

775   of CO (Stein et al., 2014; Gaubert et al., 2020; Müller et al., 2018). Due to the important role of OH in the chemical production

776   and sinks of CO, the inversion of CO emissions is sensitive to the modeled OH abundance and the emissions of CH_4 and

777   NMVOCs. According to the estimation of Müller et al. (2018), the magnitude of inversed CO emissions in China could differ

778   by more than 40% when different levels of OH concentrations are used in the model. Thus, the much higher estimations of

779   CO emissions in our inversion results may also be partly explained by the underestimation of CO chemical production or the

780   overestimation of the CO sink.

781   **4.3.1.4 PM$_{2.5}$**

782   In terms of PM$_{2.5}$, the CAQIEI suggests higher emissions than ABaCAS, HTAPv3 and EDGARv6 by about 20%, and by

783   47.7% than MEIC on the national scale. Larger discrepancies mainly occur in the NE and NW regions, where CAQIEI is about

784   27.2–114.9% and 83.2–143.2% higher than the previous inventories. The differences in the estimated PM$_{2.5}$ emissions may be

785   related to the uncertainties in the biomass-burning or anthropogenic sources in the NE region (Wu et al., 2020b), while in the

786   NW region, the errors in the fine-dust emissions may also contribute to the differences in the estimated PM$_{2.5}$ emissions there.

787   The differences in the estimated PM$_{2.5}$ emissions are relatively smaller in the NCP and SE regions, ranging from −18.9% to

788 20.4%, suggesting better agreement in the estimated PM$_{2.5}$ emissions over these two regions. In the SW region, CAQIEI is

789 closer to HTAPv3 and EDGARv6, with their differences being about 6.3% and −9.5% respectively, and is higher than MEIC

790 and ABaCAS by 54.2% and 28.6%, suggesting higher uncertainty in the estimated PM$_{2.5}$ emissions over there.

4.3.1.5 PM$_{10}$

792 For PM$_{10}$ emissions, it is difficult to directly compare CAQIEI with previous emission inventories since CAQIEI not only

793 contains anthropogenic and biomass-burning emissions, but also coarse-dust emissions. As a result, the estimated emissions

794 of PM$_{10}$ by CAQIEI are substantially higher than those by previous inventories, especially over the NW, Central and NE

795 regions (Fig. 11), which are the typical natural windblown dust-source regions in China (Zeng et al., 2020). Besides the

796 naturally windblown dust of arid desert regions (Prospero et al., 2002), large amounts of coarse-dust emissions also stem from

797 anthropogenic sources, including anthropogenic fugitive, combustion and industrial dust from urban sources (AFCID) (Philip

798 et al., 2017), and anthropogenic windblown dust from human-disturbed soils due to changes in land-use practices, deforestation

799 and agriculture (Tegen et al., 1996). Therefore, although the other regions are not typical natural windblown dust-source

800 regions in China, there are still high levels of coarse dust emissions from anthropogenic sources there (also called "urban

801 dust"), which may be the main reason for the large deviation in the estimated PM$_{10}$ emissions between CAQIEI and previous

802 inventories. On the one hand, although AFCID is included in MEIC, ABaCAS, HTAPv3 and EDGARv6, it is difficult for

803 current bottom-up emission inventories to completely represent fugitive sources (Philip et al., 2017). On the other hand, the

804 anthropogenic windblown dust emissions have not been included in current bottom-up emission inventories, which is an

805 important source of coarse dust in urban areas according to the estimations of Li et al. (2016) and the another important

806 contributor to the differences between CAQIEI and previous emission inventories.

4.3.1.6 NMVOCs

808 For NMVOC emissions, since CAQIEI includes both anthropogenic and natural sources, its estimated NMVOC emissions

809 are much higher than those estimated by previous emission inventories. After consideration of natural sources, the CAQIEI

810 suggests close estimations of the NMVOC emissions with the MEIC, HTAPv3 and CEDS inventories on the national scale,

811 with their differences being about 1.5–12.5%. The estimated NMVOC emission by ABaCAS and EDGARv6 are slightly lower

812 than CAQIEI by 17.8% and 24.6%, respectively. On the regional scale, the CAQIEI suggests higher NMVOC emissions over

813 the northern China (NCP, NE and NW), with the top-down estimated NMVOC emissions about 30.4–81.4%, 27.3–72.1%,

814 79.3–116.8%, and 8.7–57.5% higher than those of the previous emission inventories. In contrast, the CAQIEI suggests lower

815 NMVOC emissions over the SE region, with the estimated NMVOC emissions of CAQIEI being about 21.2–27.6% lower

816 than those of MEIC, ABaCAS, HTAPv3 and CEDS. These results are consistent with the previous inversion results based on

817 the satellite observations, which suggest higher NMVOC emissions over the NCP region and lower NMVOC emissions over

818 the south China (Souri et al., 2020). Over the SW region, CAQIEI shows good agreement with MEIC, ABaCAS and CEDS,

819 with CAQIEI being slightly lower than these inventories by 1.0–8.9%, but is lower than HTAPv3 and EDGARv6 by about

820 38.6% and 29.1%, respectively. Again, it should be noted that the comparisons of NMVOC emission are conducted on the

821 basis of natural emissions estimated by CAMS and GFAS, and could be more sensitive to the used natural sources than other

822 species considering the larger contributions of the natural source to the NMVOC emissions.

4.3.2 Seasonality

824 Figure 12 presents the monthly profiles of different air pollutants obtained from different emission inventories. Note that

825 the natural sources have been added to the previous inventories to facilitate the comparisons. The results show that different

826 emission inventories give similar monthly profiles of NO$_x$ and CO emissions, with higher emissions during wintertime and

827 lower emissions during summertime, which suggests relatively lower uncertainty in the estimated monthly profiles for these

828 two species. For SO$_2$ emissions, CAQIEI yields stronger monthly variation than the other inventories, with a higher proportion

829 from January to March and lower proportion during summertime. Due to the influences of dust emissions, the top-down

830 estimated PM$_{2.5}$ and PM$_{10}$ emissions show higher proportions than the other emission inventories during the spring season,

831 especially for PM$_{10}$. However, the proportion of emissions during autumn and winter are lower than in the other inventories.

832 The monthly profiles of NMVOC emissions are generally consistent, with higher emissions during summer due to the enhanced

833 biogenic emissions. However, the profile of CAQIEI is flatter than the previous inventories, and suggests a higher proportion

834 during springtime. In addition, the timings of peak values of NMVOC emissions are also different between CAQIEI and the

835 previous inventories, with CAQIEI showing peak values during May–July but the other inventories suggesting peaks during

836 June–August.

4.3.3 Emission changes during 2015–2018

838   The top-down estimated emission changes of different air pollutants during 2015–2018 were also compared with previous

839 emission inventories. Figure 13 shows the time series of the total emissions of different species from 2013 to 2020 obtained

840 from the CAQIEI and other emission inventories. Comparisons of the emission changes over the regional scales are also

841 presented in Fig. S10–S15. Before the comparison, we firstly analyze the trends of natural sources in China to investigate their

842 influences on the emission changes of different species based on the CAMS emission inventory and GFAS. Note that we only

843 consider the soil, biogenic and biomass-burning emissions for the natural sources; the trends of dust emissions in China are

844 not analyzed, which may lead to uncertainty when comparing the emission changes of PM$_{2.5}$ and PM$_{10}$. As shown in Fig. S16,

845 the natural sources of NO$_x$ and NMVOC emissions changed little during 2013–2018. The other species had small decreasing

846 trends from 2013 to 2018. However, considering the small contributions of natural sources to their emissions, these small

847 trends would not significantly influence their emission trends. For the dust emissions, previous studies have indicated a

848 declining trend in dust activity in China from 2001 to 2020 (Wu et al., 2022; Wang et al., 2021), due to weakened surface wind

849 and increased vegetation cover and soil moisture. These results suggest that the emission trends in the CAQIEI would be

850 mainly driven by the anthropogenic sources for the gaseous air pollutants based on the estimations of CAMS and GFAS, while

851 its estimated emission trends of PM$_{2.5}$ and PM$_{10}$ would be influenced by the declining trends in dust emissions in China, which

852 should be noted when comparing the emission changes of PM$_{2.5}$ and PM$_{10}$.

853   As shown in Fig. 14, all the emission inventories agree that the NO$_x$, SO$_2$, CO, PM$_{2.5}$ and PM$_{10}$ emissions in China were

854 reduced from 2015 to 2018, except for the increases of CO emissions estimated by TCR-2, which confirms the effectiveness

855 of the emission control policies implemented during the clean air action plans. Meanwhile, most emission inventories agree

856 that SO$_2$ is the species with the largest emission reduction rate, followed by PM$_{2.5}$, indicating better emission mitigation effects

857 of these two species (Fig. 14). However, the CAQIEI suggested lower emission reduction rates than the other emission

858 inventories for most species, especially for NO$_x$, PM$_{10}$ and NMVOCs (Fig. 14). The estimated emission reduction rate of NO$_x$

859 obtained from CAQIEI is about −2.7%, which is lower than the values of MEIC (−9.7%), ABaCAS (−23.0%), HTAPv3

860 (−13.0%) and CEDS (−9.0%). As we discussed in Sect. 4.2.2.2, the small reductions of NO$_x$ emission in CAQIEI would be

861 related to the increased vehicle emissions and the undesirable mitigation effects of the industry control. In fact, these factors

862 have been considered in some bottom-up emission inventories, such as MEIC. The differences between our inversion results

863 and previous inventories thus reflect uncertainty in the quantifications of the effects of these factors on the NO$_x$ emissions due

864 to the lack of sufficient statistics on mobile vehicle or other sectors. Our inversion results suggest larger adverse effects of

865 these two factors on the reductions of NO$_x$ emissions in China. According to Fig. S17, the differences between CAQIEI and

866 these inventories mainly occur in the SE, SW, NW and Central regions, with the emission reduction rate estimated by CAQIEI

867 being substantially lower than those estimated by previous inventories. In particular, CAQIEI suggests increases of NO$_x$

868 emissions over the Central region, which is opposite to the previous emission inventories. Better agreement is achieved over

869 the NCP and NE regions, with the emission reduction rate estimated by CAQIEI being closer to those of MEIC, HTAPv3 and

CEDS. The NO_x emission reduction rates estimated by EDGARv6 (−3.3%) and TCR-2 (−1.7%) are closer to our results on the national scale, but they estimated lower NO_x emission reduction rate than our estimate over the NCP and NE regions.

Similarly, the emission reduction rate of PM_{10} obtained from CAQIEI (−10.8%) is lower than those estimated by MEIC (−27.9%), ABaCAS (−33.0%) and HTAPv3 (−27.8%) on the national scale (Fig. 14). A lower PM_{10} emission reduction rate of CAQIEI than these inventories also exist in the different regions of China, except SW (Fig. S17). In particular, different from previous emission inventories, CAQIEI suggests that PM_{10} emissions may have actually increased over the Central region. Considering that dust emissions may have decreased from 2015 to 2018 owing to weakened dust events (Wang et al., 2021), the increase in PM_{10} emissions over the Central region may reflect the increases in anthropogenic sources. Meanwhile, we also found that CAQIEI estimated the emission reduction rate of PM_{10} to be smaller than that of $PM_{2.5}$. This is different from previous emission inventories, which show similar emission reduction rates for $PM_{2.5}$ and PM_{10}. Considering that PM_{10} emissions include $PM_{2.5}$ and PMC emissions, the lower emission reduction rate of PM_{10} than $PM_{2.5}$ in CAQIEI suggests that PMC emissions may have decreased slower than $PM_{2.5}$ emissions from 2015 to 2018.

In terms of NMVOCs, most previous inventories, including MEIC, EDGARv6 and CEDS, suggest a weak decrease in China, with the estimated rates of change in emissions ranging from −0.8% to −4.6%. The emission reduction rate estimated by ABaCAS is larger, reaching up to −14.2%. In contrast, the CAQIEI suggests an opposite emission change to these inventories, with estimated NMVOC emissions increasing by 26.6% from 2015 to 2018. HATPv3 also suggests an increase in NMVOC emissions, but with a much lower rate of increase (2.7%). Similar results could also be found on the regional scale (Fig. S17), especially over the NCP, NE and Central regions, where NMVOC emissions could have increased by 38.0%, 38.3% and 60.0%, respectively, according to the estimates of CAQIEI. As we discussed in Sect. 4.2.2.2, the increases of NMVOC emission estimated in CAQIEI may be related to the increased anthropogenic NMVOC emissions from the chemical industry, solvent use, and vehicles. Therefore, similar to the NO_x emissions, the differences between CAQIEI and previous inventories reflects the uncertainty in the quantifications of the impacts of these factors, and suggest larger adverse effects of these factors on the emission reductions of NMVOC emission than the previous inventories.

The differences in the estimated emission reduction rates between CAQIEI and previous inventories are relatively smaller for SO_2 and $PM_{2.5}$ emissions. The emission reduction rate of SO_2 estimated by CAQIEI is close to that estimated by MEIC and CEDS, ranging from −34.7% to −44.3%. ABaCAS and HTAPv3 estimate a larger emission reduction rate of about −58.5% and −53.7%, respectively. EDGARv6 and TCR-2 may underestimate the reduction rate of SO_2, with estimates of only about −7.0% and −9.1%, respectively. This may be because EDGARv6 underestimates the FGD (flue-gas desulfurization devices) penetration or SO_2 removal efficiencies of FGD in China. On the regional scale (Fig. S17), the top-down estimated SO_2 emission reduction rate agrees reasonably with that of MEIC over the NCP, NE and SE regions, but these inventories estimate different SO_2 emission reduction rates over the SW, NW, and Central regions. The reduction rates estimated by MEIC over the SW and Central regions is higher than those given by CAQIEI, but lower over the NW region. The other emission inventories also give different emission reduction rates, suggesting large uncertainty in the estimated SO_2 emission reduction rates over these three regions. In terms of $PM_{2.5}$, CAQIEI's estimated emission reduction rate agrees well with those of MEIC and HTAPv3 on the national scale, which is about 24–27% from 2015 to 2018. The emission reduction rate of $PM_{2.5}$ estimated by EDGARv6 are lower than our estimates and other inventories, which were about 9%. On the regional scale, our results show good consistency with MEIC and HTAPv3 over the NCP, NE, SE and SW regions, but they have large differences over the NW and SW regions.

Different from the other species, the CO emission reduction rate estimated by CAQIEI (−21.3%) is higher than in most of the previous inventories, including MEIC (−13.0%), ABaCAS (−11.6%), EDGARv6 (−4.7%), and CEDS (−11.7%), suggesting larger mitigation effects on CO emissions than other inventories. HTAPv3 agrees with our results, with an estimated emission reduction rate of about −22.0%. On the regional scale (Fig. S17), our result is consistent with MEIC over the NCP and SE regions, with estimated emission reduction rates for CO of around 24% and 15%, respectively, while in other regions

913 the emission reduction rate estimated by CAQIEI is higher than that estimated by MEIC. The TCR-2 shows opposite changes

914 in CO emissions compared with the other inventories insofar as it suggests increases of CO emissions over different regions

915 of China. Since the emissions in TCR-2 are constrained by satellite observations, the differences between our results and those

916 of TCR-2 highlight that the observations used to constrain the emissions may have a large influence on the estimated emission

917 changes. In this case, the estimated changes of CO emissions by CAQIEI are more consistent with those estimated by other

918 bottom-up inventories. Considering this, the TCR-2 may have uncertainties in its estimated changes of CO emissions in China

919 from 2015 to 2017, which could be related the suboptimal performance of the data assimilation caused by the underestimated

920 background errors of CO or too short assimilation window for the CO emission estimates (Miyazaki et al., 2020).

4.4 Uncertainty estimation of CAQIEI

922   Finally, the uncertainty of the inversed emission inventory product is estimated in this section to facilitate users'

923 understanding of the data's accuracy. Within the framework of EnKF, the analysis perturbation $\mathbf{X^a}$ estimated by using Eq. (3)

924 could provide the information regarding the uncertainty of the inversed emission inventory. The Coefficient of variation

925 (hereinafter, CV), defined as the standard deviation divided by the average, with a larger value denoting higher uncertainty, is

926 calculated based on the analysis perturbation to measure the uncertainty of the inverse emission inventory. Based on this

927 method, the uncertainty (CV) of the a posteriori emission was estimated as follows: 92.3% ($PM_{2.5}$), 88.8% (PM_{10}), 26.7%

928 (SO_2), 46.8% (CO), 31.8% (NO_x) and 65.5% (NMVOC). However, it should be noted that such uncertainty was only calculated

929 under the framework of the EnKF constructed in this study, which is dependent on the assigned value of the a priori emission

930 uncertainty, observation errors and the number of assimilated observations. In addition, we only considered the a priori

931 emission uncertainty and the observation errors during the inversion. The influences of the other error sources, such as

932 uncertainty in the chemistry transport model, meteorology simulations and the inversion method were not considered.

933 Therefore, the current estimated uncertainty should be considered as a lower bound for the real uncertainty. More systematic

934 analysis that thoroughly consider the uncertainty sources regarding the emission inversion should be conducted in future to

935 give a more accurate estimation of the uncertainty in our products.

5 Discussion and conclusion

937   A long-term, top-down emissions inventory of major air pollutants in China was developed and validated in this study by

938 assimilating surface observations from CNEMC using the modified EnKF method and NAQPMS. It includes gridded emission

939 maps of NO_x, SO_2, CO, primary $PM_{2.5}$, primary PM_{10}, and NMVOCs in China from 2013 to 2020, on a monthly basis, with a

940 horizontal resolution of 15 km × 15 km. This new top-down emissions inventory, named CAQIEI, provides new insights into

941 the air pollutant emissions and their changes in China during the country's two clean air action periods. The estimated total

942 emissions for the year 2015 in China are 25.2 Tg of NO_x, 17.8 Tg of SO_2, 465.4 Tg of CO, 15.0 Tg of $PM_{2.5}$, 40.1 Tg of PM_{10}

943 and 46.0 Tg of NMVOCs. Comparisons of CAQIEI with previous inventories, including MEIC, ABaCAS, HTAPv3,

944 EDGARv6, CEDS and TCR-2, on the basis of the natural emissions obtained from CAMS and GFAS showed reasonable

945 agreement for the estimation of NO_x, SO_2 and NMVOC emissions in China. The $PM_{2.5}$ emissions obtained from CAQIEI (13.2

946 Tg) are slightly higher than in the previous emission inventories (8.3–11.1 Tg), while the CO emissions estimated by CAQIEI

947 (426.8 Tg) are substantially higher than in previous inventories (120.7–237.7 Tg). However, the reasons for such a large gap

948 are still not clear, but might be attributable to both the underestimation of CO sources (e.g., anthropogenic, biomass-burning

949 and chemical-production sources) (Bergamaschi et al., 2000; Miyazaki et al., 2012; Petron et al., 2002; Petron et al., 2004;

950 Tang et al., 2013; Gaubert et al., 2020), and/or the overestimation of CO sinks in the model (Müller et al., 2018). In addition,

951 comparisons with previous inversion studies suggest there are larger differences in the top-down estimated CO emissions based

952 on surface and satellite observations. Our inversion results are consistent with previous inversions based on surface

observations, but are much higher than those based on satellite observations, suggesting large uncertainty in inversion-estimated CO emissions in China. Therefore, more research is needed to better understand the reasons behind the negative biases in CO simulation, and to explain the differences between our results and those of previous inventories. Similar to situation with CO emissions, the PM_{10} emissions estimated by CAQIEI (37.7 Tg) are also substantially higher than in previous inventories (11.1–15.9 Tg). However, this will be mainly associated with the emissions of coarse dust, which were not included in previous inventories. The estimation of dust emissions in China is subject to high levels of uncertainty, with the estimated dust fluxes based on different dust emission schemes differing by several orders of magnitude (Zeng et al., 2020). Therefore, our inversion results could provide a reference for the magnitude of coarse-dust emissions in China, which could then help to reduce the large uncertainty in estimations of dust emissions in China.

Several potential important deficiencies in current emission estimations were also indicated by CAQIEI on the regional scale. For example, the CAQIEI suggests substantially higher air pollutant emissions than the previous emission inventories over the NW and Central regions. Thus, the air pollutant issues may be more severe than we expected over these two regions. Meanwhile, our inversion results suggest higher NMVOC emissions over the northern China but suggest lower NMVOC emissions in southern China, which is consistent with the previous inversion studies based on the satellite. China is now facing increasingly severe O_3 pollution and has an urgent need for a coordinated control of O_3 and $PM_{2.5}$. Our results may provide valuable information on the NMVOC emissions in China, which is important for a proper understanding of O_3 pollution and the development of effective control strategies nationally. Higher emissions were also found in the NE region based on our inversion results. The NE region is a typical area for open-area biomass burning, with significant emissions from straw combustion (Wu et al., 2020b). The higher emissions estimated by our inversion result may indicate higher biomass-burning emissions over there. This is consistent with recent estimations of biomass-burning emissions by Xu et al. (2023) and Wu et al. (2020b), who showed higher biomass-burning emissions in China than previous estimations, including those of GFEDv4.1s (https://www.globalfiredata.org/data.html), FINNv1.5 (https://www.acom.ucar.edu/Data/fire/), and GFASv1.2 (https://www.ecmwf.int/en/forecasts/dataset/global-fire-assimilation-system).

Based on CAQIEI, we further quantified the emission changes of different air pollutants in China during the two clean air action plans. The results confirmed the effectiveness of these campaigns on the mitigation of air pollutant emissions in China, with estimated emission reductions of 15.1% for NO_x, 54.5% for SO_2, 35.7% for CO, 44.4% for $PM_{2.5}$, and 33.6% for PM_{10} from 2015 to 2020. In contrast, NMVOC emissions increased by 21.0% from 2015 to 2020. Comparisons of the estimated emission reduction rates during the two clean air action plans suggested that emission reductions were larger during the 2018–2020 than during 2015–2017. The estimated rates of change in emissions were 5.9% for NO_x, −23.8% for SO_2, −9.8% for CO, −14.5% for $PM_{2.5}$, −7.2% for PM_{10}, and 27.6% for NMVOCs during 2015–2017, which were smaller than the −12.1% for NO_x, −23.5% for SO_2, −18.3% for CO, −26.6% for $PM_{2.5}$, −25.5% for PM_{10}, and −4.5% for NMVOCs during 2018–2020. On the one hand, this is due to the fact that more sectors were controlled during the 2018–2020 action plan. Besides the industrial and power sectors, which were the main points of control in the 2013–2017 action plan, the residential sector, transportation sector, and non-point sources like blowing-dust emissions, were also strengthened in the 2018–2020 action plan. Consequently, the emission reduction rates of CO, $PM_{2.5}$ and PM_{10} during 2018–2020 were higher than those during the 2015–2017 when the 2013–2017 action plan was implemented. However, the reduction of SO_2 emissions was similar during the two action plan periods. This is because most SO_2 emissions stem from the industrial sector and power plants, which together contribute about 77% of all emissions (Zheng et al., 2018). Thus, the additional control of other sectors in the 2018–2020 action plan may not have significantly impacted the mitigation of SO_2 emissions. On the other hand, strict emission controls were implemented or strengthened in more areas of China during the 2018–2020 action plans. For example, the inversion results indicated that there were obvious increases of SO_2, NO_x, $PM_{2.5}$, PM_{10} and NMVOC emissions during 2015–2017 over the Central region, especially in the Fenwei Plain area, where the emission controls were relatively weak during the 2013–2017 action plan. However, all species showed obvious emission reductions almost the whole China during the 2018–2020 action plan.

996   The estimated rates of change in emissions during 2015–2018 were also compared with those estimated by previous
997   emission inventories. Although both CAQIEI and previous inventories showed declines of air pollutant emissions in China,
998   the emission reduction rates estimated by CAQIEI were generally smaller than those estimated by previous inventories,
999   especially for NO_x, PM_{10} and NMVOCs, suggesting a smaller mitigation effects of the air pollution control measures than the
1000   previous emission inventories suggested. In particular, China's NMVOC emissions were shown to have increased by 26.6%
1001   from 2015 to 2018, especially over NCP (38.0%), NE (38.3%) and Central (60.0%). CO was found to be an exception insofar
1002   as the emission reduction rate estimated by CAQIEI was larger than that of most previous emission inventories, except in the
1003   NCP region. The estimated emission reduction rates of SO_2 and $PM_{2.5}$ were relatively closer to those of previous inventories,
1004   suggesting better consistency in the estimated emission reduction for these two species.

1005   Overall, the inversion inventory developed in this study could provide us with value information on the complex variations
1006   of air pollutant emissions in China during its two recent clean air action periods, which could help improve our understanding
1007   of air pollutant emissions and related changes in air quality in China. For example, the increases of O_3 and nitrate
1008   concentrations may be associated with the undesirable emission reduction effects of the 2013–2017 action plans. The estimated
1009   lower NO_x emission reduction rate by CAQIEI may also help explain the weak responses of nitrogen deposition fluxes to the
1010   clean air action plans. Meanwhile, this top-down emissions inventory can be used to supply the input data for CTMs or server
1011   as a comparable reference for future inversion studies based on other methods or observation data, which is expected to
1012   improve the performance of model simulations and air quality forecasts, and facilitate the development of inversion method.

6 Limitations

1014   However, due to the complexity of the emission estimation, it is inevitable that there are some limitations in our inversion
1015   results. Here We summarise some issues that might affect the quality of the CAQIEI which were known at the time of
1016   publication to assist the potential users in properly using this data products.

1017   (1) The changes in the number of observation sites would induce spurious emission trends during 2013–2014, especially
1018   over western China, although the influence of the number of observation sites is smaller over the NCP and SE regions because
1019   of their higher density of observation sites. Therefore, it is recommended that not to use the emissions in 2013 and 2014 when
1020   analyzing the emission trends in China. This limitation makes it difficult to estimate the overall emission control effects of
1021   2013 – 2017 action plan. Consequently, the emission change rate during the 2015–2017 were sampled in this study to represent
1022   the emission control effects of the 2013–2017 action plan, but it may not necessarily reflect the overall reduction rate of the
1023   action plan for the entire period. In addition, although the number of observation sites has become stable since 2015, the limited
1024   number of observation sites makes it difficult to fully constrain China's air pollutant emissions, especially for the natural
1025   sources considering that the majority of the observation sites are located in the urban areas. Therefore, the uncertainty in the
1026   estimated emissions over the remote areas are expected to be higher than those over the urban areas, especially for the species
1027   with large amount of natural emission, such as PM and NMVOC. For example, the coarse-dust emissions over western China
1028   are expected to be underestimated by CAQIEI because of the limited availability of observation sites. Therefore, adding
1029   observations there will help improve the accuracy of the inversion estimates. For example, simultaneous assimilation of the
1030   surface and satellite observation may help alleviate this problem and provide more constrains on the emissions without surface
1031   observations.

1032   (2) The natural and anthropogenic emissions are not differentiated in our inversion method, leading to higher emissions
1033   of PM_{10} and NMVOCs than in other emission inventories. This also hinders the comparisons of our inversion results with the
1034   previous inventories. Therefore, potential readers should be aware of that the current comparisons of our inversion results and
1035   previous inventories are on the basis of the natural emissions estimated by CAMS and GFAS, which does not necessarily
1036   indicate large uncertainties in anthropogenic sources within the bottom-up inventories. The impacts are expected to be smaller

1037 for the NO_x, SO_2 and CO due to the small contributions of natural sources to their emission, but would be larger for NMVOC

1038 and PM which has large amount of natural emission. Assimilation of isotope data, speciated $PM_{2.5}$ and NMVOC observations

1039 may help differentiate the natural and anthropogenic emissions, and address this problem in future.

1040   (3) The NMVOC emissions may have larger uncertainty than the other species. On the one hand, a significant amount of

1041 NMVOC emission would originate from suburban or rural regions. Therefore, although the O_3 observations at the urban sites

1042 could provide information on the NMVOC emissions over the suburban or rural areas according to covariance estimated by

1043 the ensemble simulation, the NMVOC emissions may not be fully constrained due to the lack of observation sites over the

1044 suburban or rural areas. On the other hand, due to the lack of long-term NMVOC observations, the NMVOC emissions were

1045 constrained by the O_3 concentrations in this study. Although the feasibility of this approach has been demonstrated by previous

1046 inversion studies, the nonlinear NO_x-VOC-O_3 interactions could inevitably introduces greater uncertainty into the inversion of

1047 NMVOC than other species. Therefore, more attention should be paid while using the inversion results of NMVOC, and more

1048 robust analysis of the effects of nonlinear NO_x-VOC-O_3 interactions and the number of observation sites should be performed

1049 in future to better illustrate the feasibility of assimilating O_3 to constrain the NMVOC emissions.

1050   (4) The errors in the meteorological simulation and the CTMs were not considered in the emission inversions, which

1051 would lead to uncertainty in our estimated emissions. For example, the errors in the simulated wind would influence the

1052 transportation of the air pollutant and lead to uncertainty in the emissions distributions. According to the evaluation results of

1053 meteorological simulations (Table S1), the simulated relative humidity is generally lower than the observations, which may

1054 weaken the formation of secondary aerosol. On the contrary, the simulated precipitation was higher than the observation for

1055 most regions which would lead to overestimations of the wet removal of air pollutants. As a result, there may be a positive

1056 tendency in the inversed emission inventory due to the errors in the simulated relative humidity and precipitation. Besides

1057 these parameters, the accuracy of the simulated boundary layer is also important for the performance of the emission inversions

1058 (Du et al., 2020), although it was not evaluated currently due to the lack of observation. If the WRF systematically

1059 underestimates the boundary layer, the vertical diffusions of the air pollutants would be suppressed, which would lead to

1060 overestimated surface air pollutant concentrations and a negative tendency in the inverse emission inventory. However, it is

1061 difficult to quantify the influences of the meteorological errors on the emission inversions, as the errors in the meteorological

1062 simulation and chemical transport model interact with each other. More comprehensive analysis should be conducted in the

1063 future to better understand the impacts of the meteorological and model errors on the inverse emission inventory. A multi-

1064 model inversion framework, for example that of Miyazaki et al. (2020a), may help alleviate the influences of model errors on

1065 emission inversions in future. Using other models (e.g., WRF-Chem, CMAQ) to validate our inversion inventory could also

1066 help us assess the impacts of model uncertainty on the emission inversions. Meanwhile, because of the many uses that require

1067 a rapid update of emissions, it may be time to organize an intercomparison study focused on the emission inversions.

1068   (5) Current inversion emission inventory is mainly assessed by the surface observations and previous emission

1069 inventories. more independent observations, such as the satellite observation data, should be used in future to further validate

1070 the inversion results of this study and its derived findings. For example, the independent measurements from field campaign

1071 or satellite retrievals (e.g., TropOMI CO data) can help validate the reliability of the much higher a posterior CO emissions in

1072 CAQIEI than the previous inventories in the future.

1073 **7 data availability**

1074   The CAQIEI inventory can be freely download at https://doi.org/10.57760/sciencedb.13151 (Kong et al., 2023), which

1075 includes monthly grid maps of the air pollutant emissions from 2013 to 2020. The contained species include NO_x, SO_2, CO,

1076 primary $PM_{2.5}$, primary PM_{10} and NMVOC. The horizontal resolution is 15km. There are totally 8 Network Common Data

1077 Form files (NetCDF), which were named by the date and contains the monthly emissions of different air pollutants in China

1078 in each year. The description of the content of each NetCDF file and some important notes when using this dataset are also
1079 available in README.txt on the website.
1080

1081 **Tables**

1082 **Table 1. Corresponding relationships between the chemical observations and adjusted emissions**

Species	Description	Observations used for inversions of this species
BC	Black carbon	$PM_{2.5}$
OC	Organic carbon	$PM_{2.5}$
PMF	Fine-mode unspeciated aerosol	$PM_{2.5}$
PMC	Coarse-mode unspeciated aerosol	$PM_{10} - PM_{2.5}$
NO_x	Nitrogen oxide	NO_2
SO_2	Sulfur dioxide	SO_2
CO	Carbon monoxide	CO
NMVOCs	Non-methane volatile organic compounds	MDA8h O_3

1083
1084
1085
1086
1087
1088
1089
1090
1091
1092
1093
1094
1095
1096
1097
1098
1099
1100
1101
1102
1103
1104
1105
1106
1107

Table 2. Evaluation statistics of the *a posteriori* (*a priori*) model simulation for different species[a]

	PM$_{2.5}$ (µg/m^3)				PM$_{10}$ (µg/m^3)			
	R	MBE	NMB (%)	RMSE	R	MBE	NMB (%)	RMSE
Hourly	0.77 (0.53)	2.1 (13.3)	4.5 (28.6)	32.4 (55.6)	0.72 (0.44)	−3.7 (−11.5)	−4.6 (−14.3)	53.1 (74.4)
Daily	0.89 (0.61)	2.1 (13.3)	4.4 (28.4)	20.0 (46.3)	0.88 (0.51)	−3.7 (−11.2)	−4.6 (−14.1)	31.6 (62.2)
Monthly	0.94 (0.68)	2.1 (13.3)	4.5 (28.3)	11.7 (32.5)	0.90 (0.56)	−3.6 (−11.3)	−4.5 (−14.1)	21.2 (44.1)
Yearly	0.94 (0.62)	2.2 (11.9)	4.4 (24.3)	9.1 (27.7)	0.89 (0.52)	−3.8 (−13.4)	−4.6 (−16.1)	18.5 (38.7)

	SO$_2$ (µg/m^3)				NO$_2$ (µg/m^3)			
	R	MBE	NMB (%)	RMSE	R	MBE	NMB (%)	RMSE
Hourly	0.64 (0.16)	−1.8 (19.0)	−9.1 (93.8)	24.9 (58.7)	0.67 (0.45)	−1.2 (−0.9)	−3.9 (−2.7)	19.9 (25.5)
Daily	0.80 (0.20)	−1.8 (19.0)	−9.2 (94.5)	16.0 (51.4)	0.80 (0.51)	−1.2 (−0.8)	−3.7 (−2.6)	12.8 (20.1)
Monthly	0.85 (0.20)	−1.9 (18.9)	−9.3 (93.1)	12.4 (45.8)	0.84 (0.57)	−1.2 (−0.8)	−3.8 (−2.6)	9.4 (15.6)
Yearly	0.83 (0.18)	−2.4 (17.0)	−10.8 (75.9)	11.6 (42.4)	0.82 (0.63)	−1.3 (−1.6)	−3.9 (−5.0)	8.1 (13.0)

	CO (mg/m^3)				O$_3$ (µg/m^3)			
	R	MBE	NMB (%)	RMSE	R	MBE	NMB (%)	RMSE
Hourly	0.69 (0.38)	−0.1 (−0.4)	−8.8 (−45.6)	0.6 (0.8)	0.71 (0.51)	5.6 (−8.4)	9.5 (−14.0)	34.9 (41.6)
Daily	0.81 (0.42)	−0.1 (−0.4)	−8.6 (−45.5)	0.4 (0.7)	0.71 (0.40)	5.7 (−8.4)	9.5 (−14.1)	26.1 (33.8)
Monthly	0.83 (0.42)	−0.1 (−0.4)	−8.7 (−45.7)	0.3 (0.7)	0.76 (0.47)	5.6 (−8.4)	9.4 (−14.1)	19.6 (26.0)
Yearly	0.82 (0.27)	−0.1 (−0.5)	−9.0 (−47.6)	0.3 (0.7)	0.53 (0.11)	5.1 (−7.8)	8.7 (−13.4)	14.2 (20.5)

[a] The time series of the air pollutant concentrations at each station were firstly catenated into a single vector. Then the values of each evaluation metric were calculated based on the catenated time series of the observed and simulated concentrations.

1112
1113
1114
1115
1116
1117
1118
1119
1120
1121
1122
1123
1124
1125
1126
1127
1128

1129 **Table 3. Inversion-estimated emissions (Tg/yr) of different species in China as well as the six regions for year 2015**

	China	NCP	SE	NE	SW	NW	Central
NO_x	25.2	5.1	7.1	4.5	4.2	1.2	3.2
SO_2	17.8	3.5	3.3	4.0	2.6	0.8	3.6
CO	465.4	82.2	106.7	78.7	82.8	32.6	82.3
$PM_{2.5}$	14.9	2.7	3.3	3.1	2.9	1.2	1.9
PM_{10}	40.1	8.7	7.5	8.2	5.5	4.1	6.2
NMVOC	46.0	9.0	13.7	8.5	7.8	2.7	4.2

1130
1131
1132
1133
1134
1135

1136 **Table 4. The calculated annual trends of $PM_{2.5}$ and PM_{10} emissions in China based on CAQIEI**

	$PM_{2.5}$ (Tg/year)			PM_{10} (Tg/year)		
	2015–2020	2015–2017	2018–2020	2015–2020	2015–2017	2018–2020
China	−1.4*	−1.1	−1.5	−2.6*	−1.4	−4.6
NCP	−0.32*	−0.30	−0.32	−0.64*	−0.88	−0.99
SE	−0.32*	−0.21	−0.44	−0.52*	−0.48	−0.84
NE	−0.24*	−0.25	−0.11	−0.52*	−0.22	−0.73
SW	−0.21*	−0.26	−0.20	−0.40*	−0.26	−0.56
NW	−0.09	−0.08	−0.12	−0.20*	−0.32	−0.32
Central	−0.15	0.01	−0.32	−0.27	−0.32	−1.14

1137 * Trend is significant at the 0.05 significance level
1138
1139
1140
1141
1142
1143
1144
1145
1146
1147
1148
1149
1150
1151
1152
1153
1154
1155

Table 5. The calculated annual trends of the four gaseous emissions in China based on CAQIEI

	SO_2 (Tg/year)			CO (Tg/year)		
	2015–2020	2015–2017	2018–2020	2015–2020	2015–2017	2018–2020
China	−2.1*	−2.1	−1.3	−36.0*	−22.8	−33.5
NCP	−0.57*	−0.69	−0.21	−8.4*	−4.30	−7.23
SE	−0.34*	−0.39	−0.20	−6.1*	−3.54	−8.37
NE	−0.44*	−0.44	−0.21	−6.2*	−1.74	−3.91
SW	−0.22*	−0.27	−0.17	−3.8*	−2.36	−4.54
NW	−0.08*	−0.08	−0.08	−3.0*	−0.73	−2.95
Central	−0.46*	−0.25	−0.40	−8.7*	−10.14	−6.55

	NO_x (Tg/year)			NMVOC (Tg/year)		
	2015–2020	2015–2017	2018–2020	2015–2020	2015–2017	2018–2020
China	−0.67	0.74	−1.6	1.9	6.3	−1.3
NCP	−0.32	0.05	−0.40	0.66	1.37	−0.42
SE	−0.22	0.18	−0.49	0.50	1.73	−0.24
NE	−0.17	0.03	−0.19	0.03	0.79	−0.49
SW	−0.06	0.10	−0.26	0.23*	0.43	0.03
NW	−0.03	0.11	−0.06	0.10	0.69	−0.27
Central	0.04	0.28	−0.16	0.55*	1.33	0.09

1157 * Trend is significant at the 0.05 significance level

1158

1159

1160

1161

1162

1163

1164

1165

1166

1167

1168

1169

1170

1171

1172

1173

1174

1175

1176

1177

1178

1179

1180

Table 6 The top-down estimated CO emissions in China from previous inventories

Reference	Region	Period	Method	Assimilated observation	*A priori* CO emission (kt/day)	*A posteriori* CO emission (kt/day)
Feng et al. (2020)	China Mainland	December 2013	EnKF with CMAQ model	Surface observation	586.4	1678.0
		December 2017			499.3	1388.1
	NCP	December 2013			143.9	394.3
		December 2017			120.5	340.7
Muller et al. (2018)	China	2013	4DVar with IMAGES model	IASI CO observation with different constraints on OH levels	454.8	367.1–553.4
Gaubert et al. (2020)	Central China	May 2016	DART/CAM-CHEM	MOPITT CO observation	193.6	220.3
	North China				93.5	163.6
Jiang et al. (2017)	East China	2013	4DVar with GEOS-Chem	MOPITT CO observation	564.5	439.5–484.4
		2014				430.4–481.1
		2015				397.5–439.7
Zheng et al. (2019)	China	2010–2017 average	Bayesian inversion	MOPITT CO, OMI HCHO, and GOSAT CH4 observation	-	444.4

1182
1183
1184
1185
1186
1187
1188
1189
1190
1191
1192
1193
1194
1195
1196
1197

Figures

1200
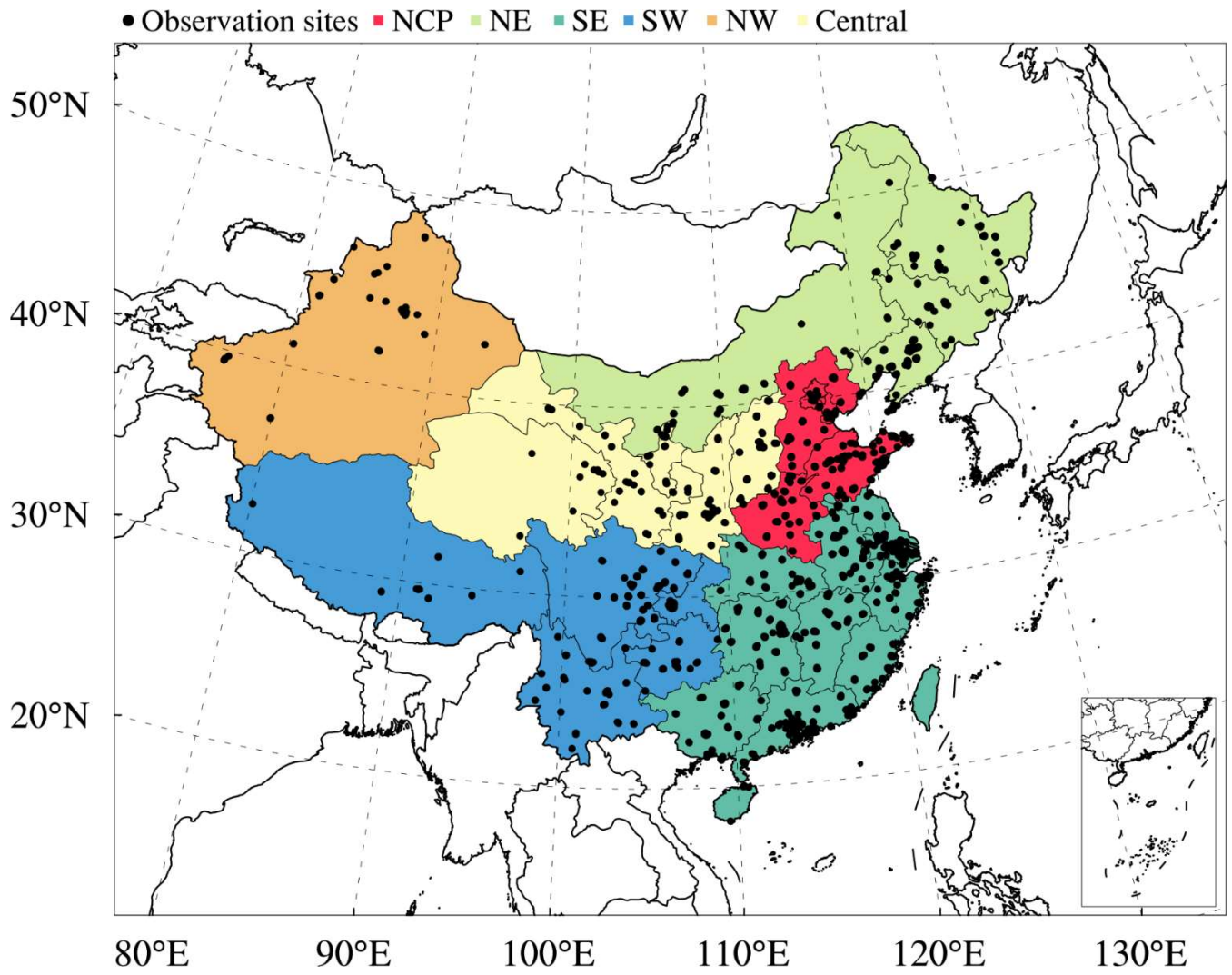
1201 **Figure 1: Modeling domain of the ensemble simulation overlaid with the distributions of observation sites from CNEMC. Different**
1202 **colors denote the different regions in mainland China—namely, the North China Plain (NCP), Northeast China (NE), Southwest**
1203 **China (SW), Southeast China (SE), Northwest China (NW) and Central China (Central).**

1204
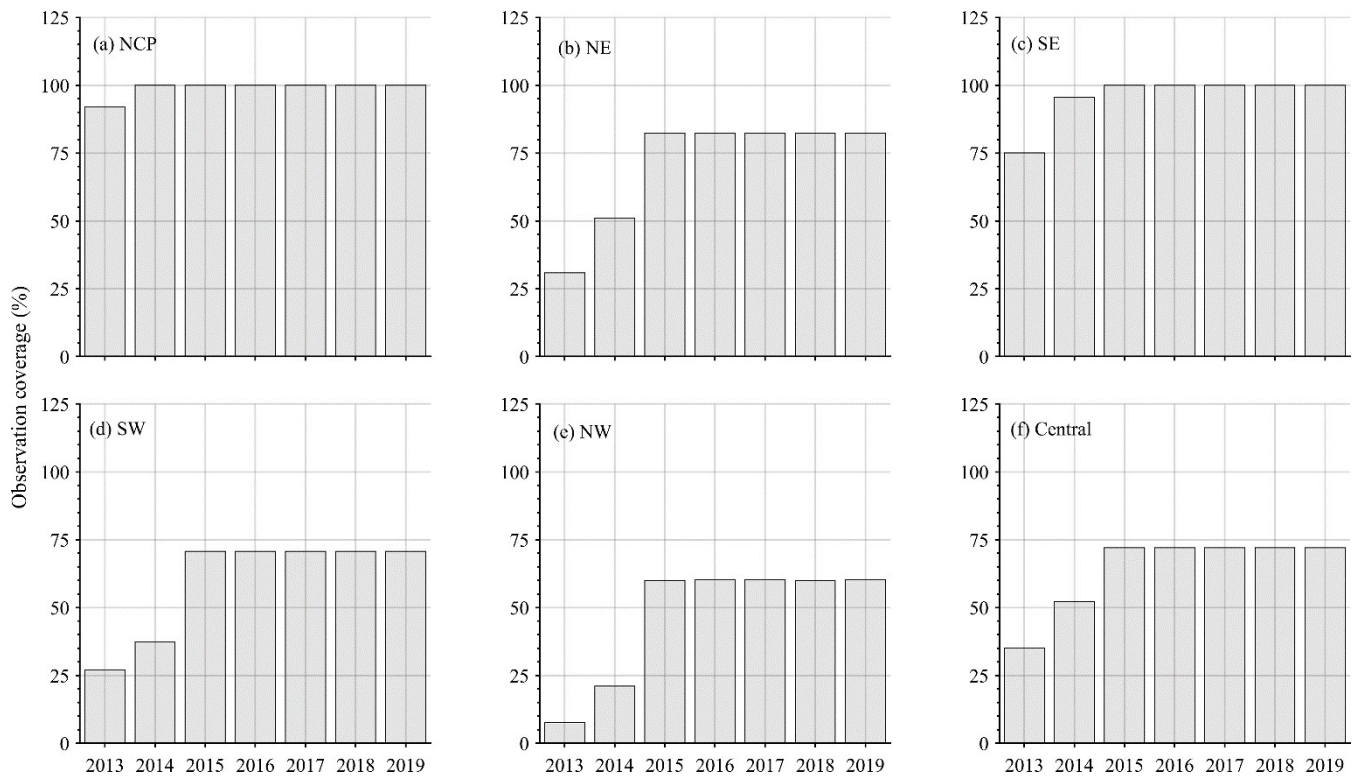
Figure 2: Time series of the observational coverage from 2013 to 2020 over different regions of China.
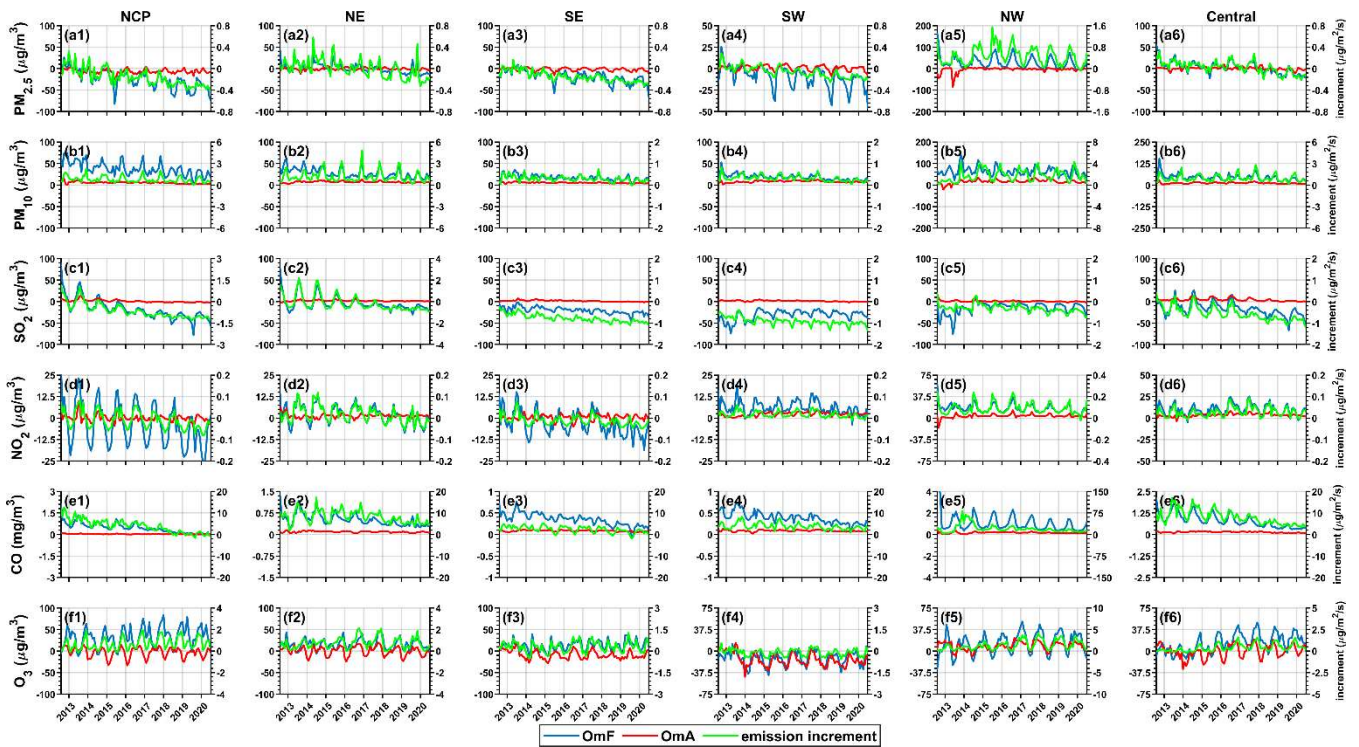
Figure 3: Time series of the *a priori* bias (blue lines), the *a posteriori* bias (red lines), and the emission increment (green lines) from 2013 to 2020 for different species over the six regions of China.

1216
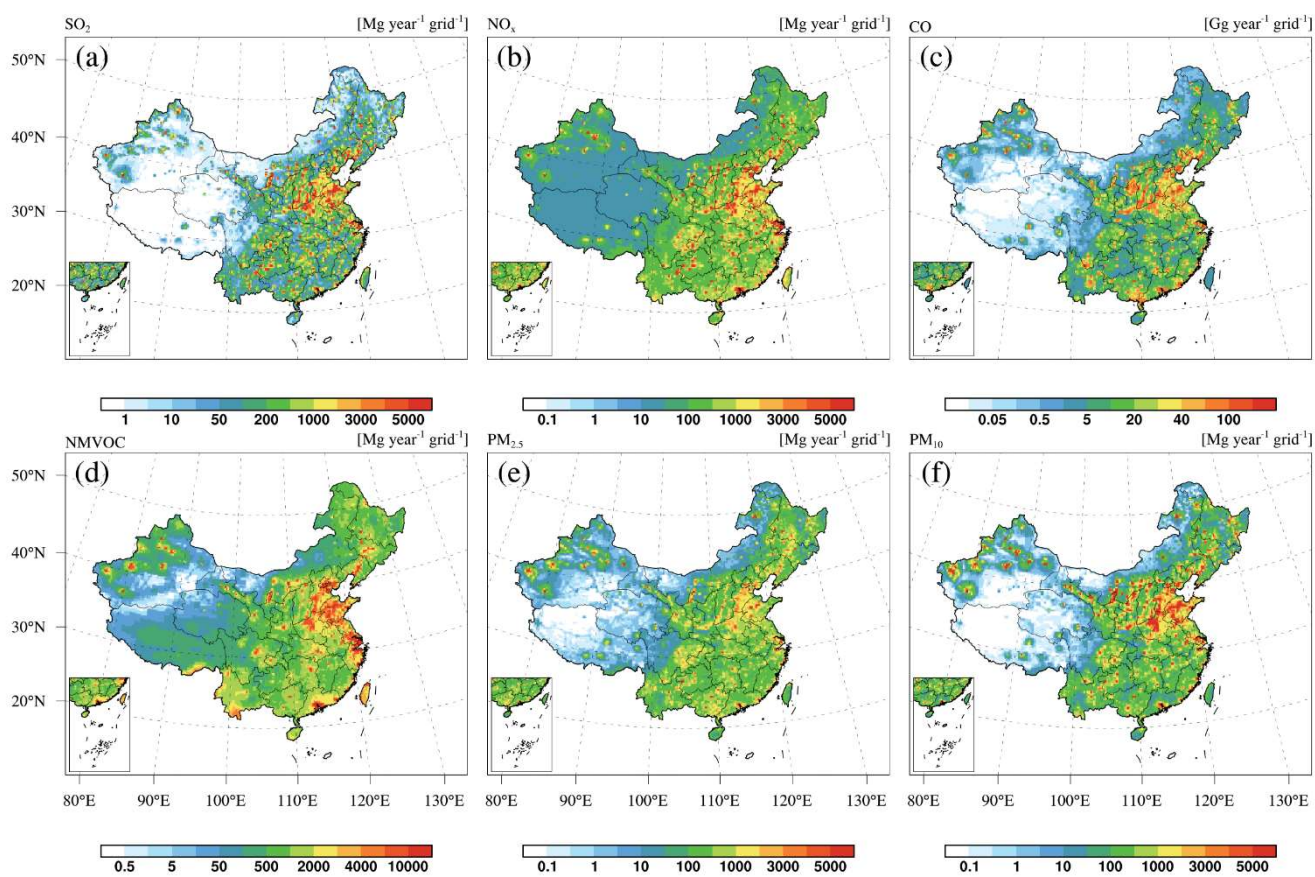
Figure 4: Spatial distributions of the emissions of (a) SO$_2$, (b) NO$_x$, (c) CO, (d) NMVOCs, (e) PM$_{2.5}$, and (f) PM$_{10}$ in 2015 obtained from CAQIEI.

1219

1220

1221
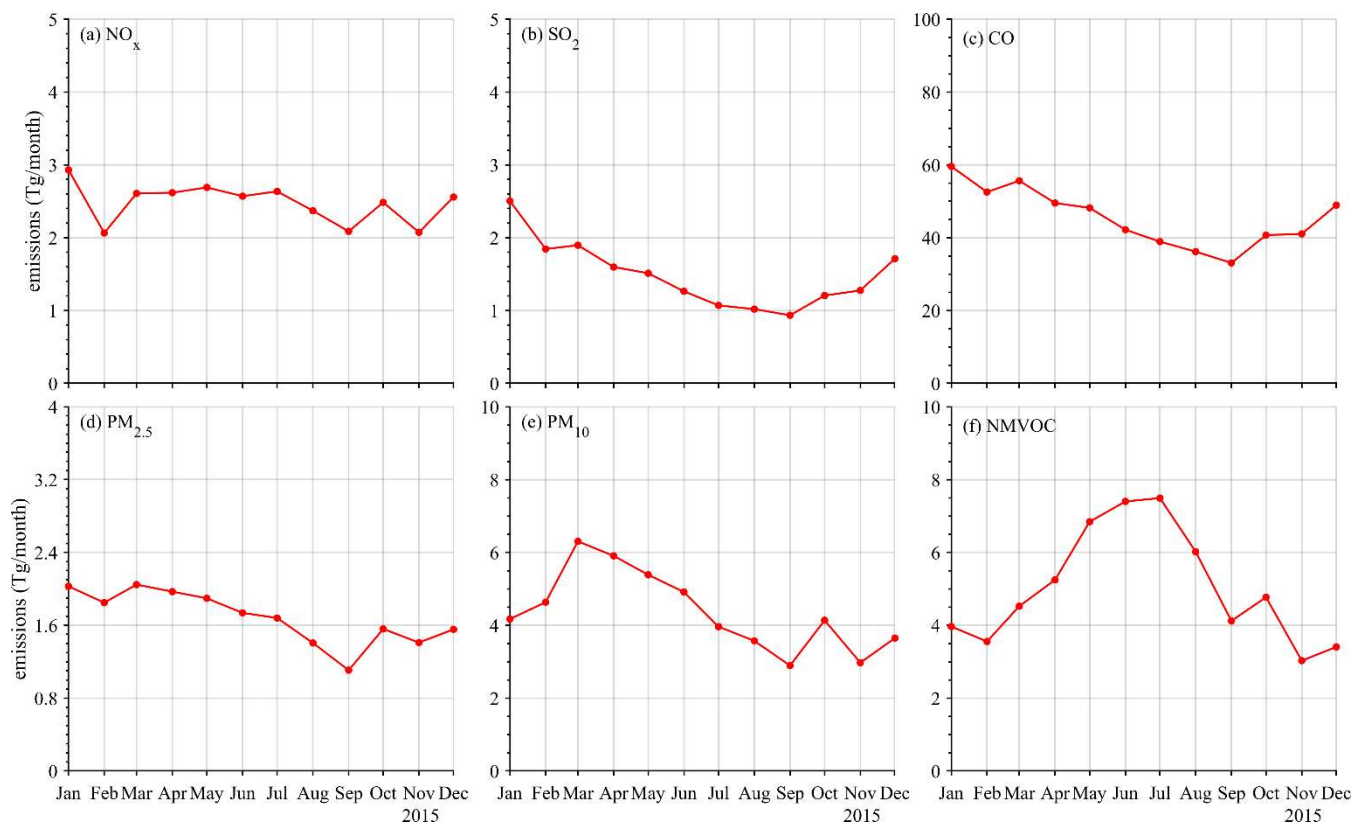
Figure 5: Monthly series of total emissions of (a) NO$_x$, (b) SO$_2$, (c) CO, (d) PM$_{2.5}$, (e) PM$_{10}$, and (f) NMVOCs in China for year 2015 obtained from CAQIEI.
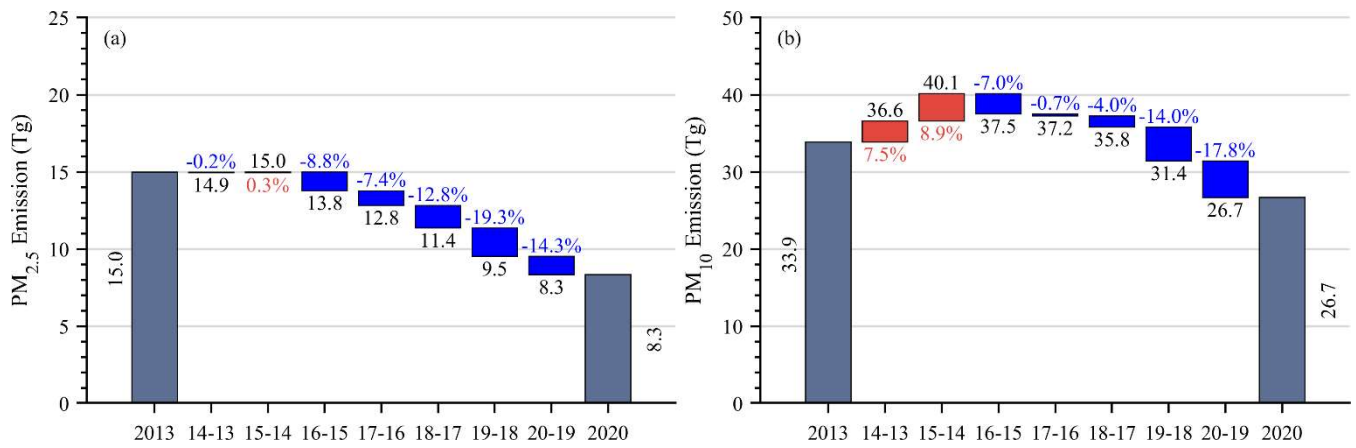
Figure 6: Emission changes in (a) PM$_{2.5}$ and (b) PM$_{10}$ obtained from CAQIEI from 2013 to 2020.
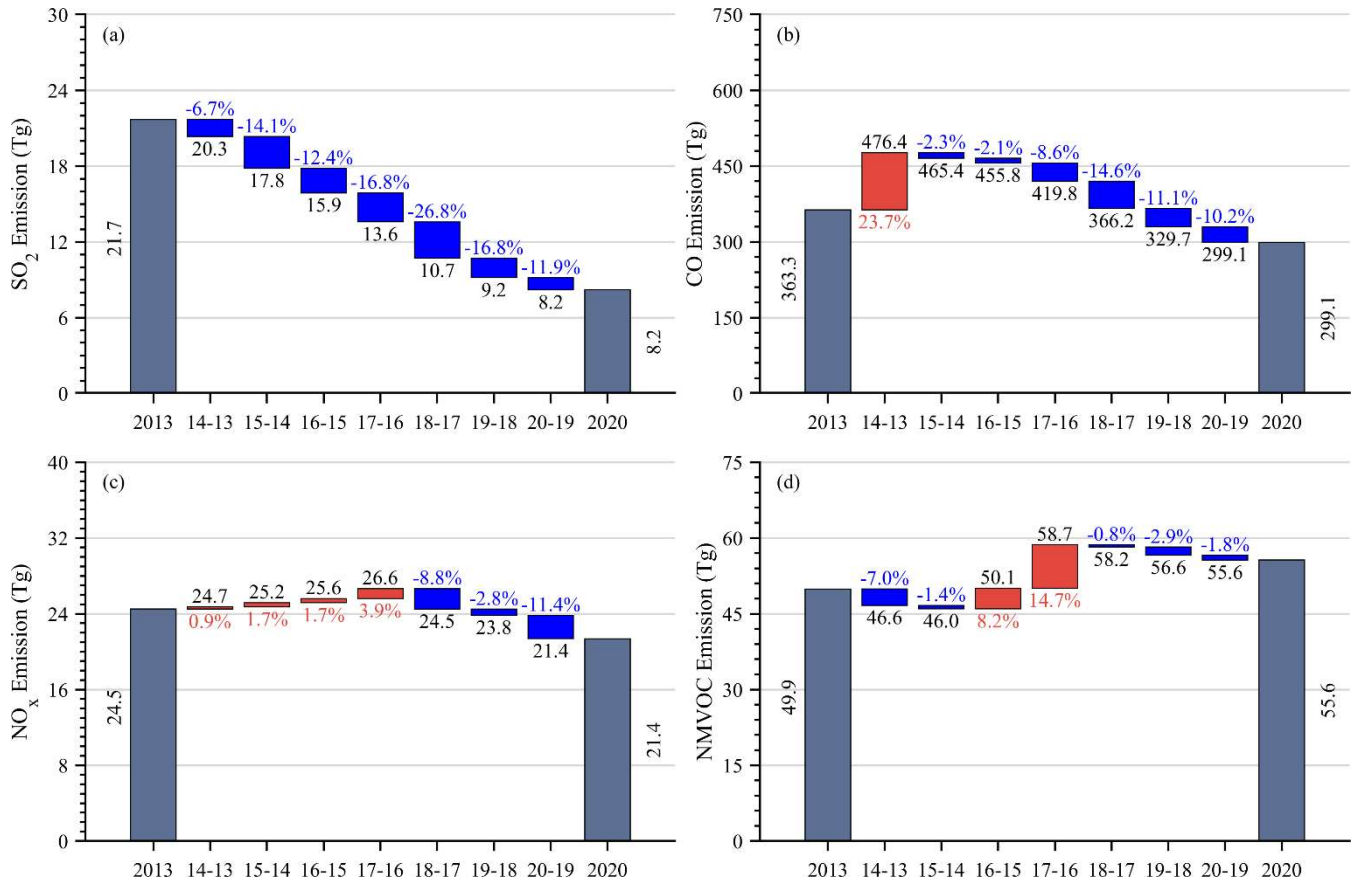
Figure 7: Emission changes in (a) SO$_2$, (b) CO, (c) NO$_x$, and (d) NMVOCs obtained from CAQIEI from 2013 to 2020.

36
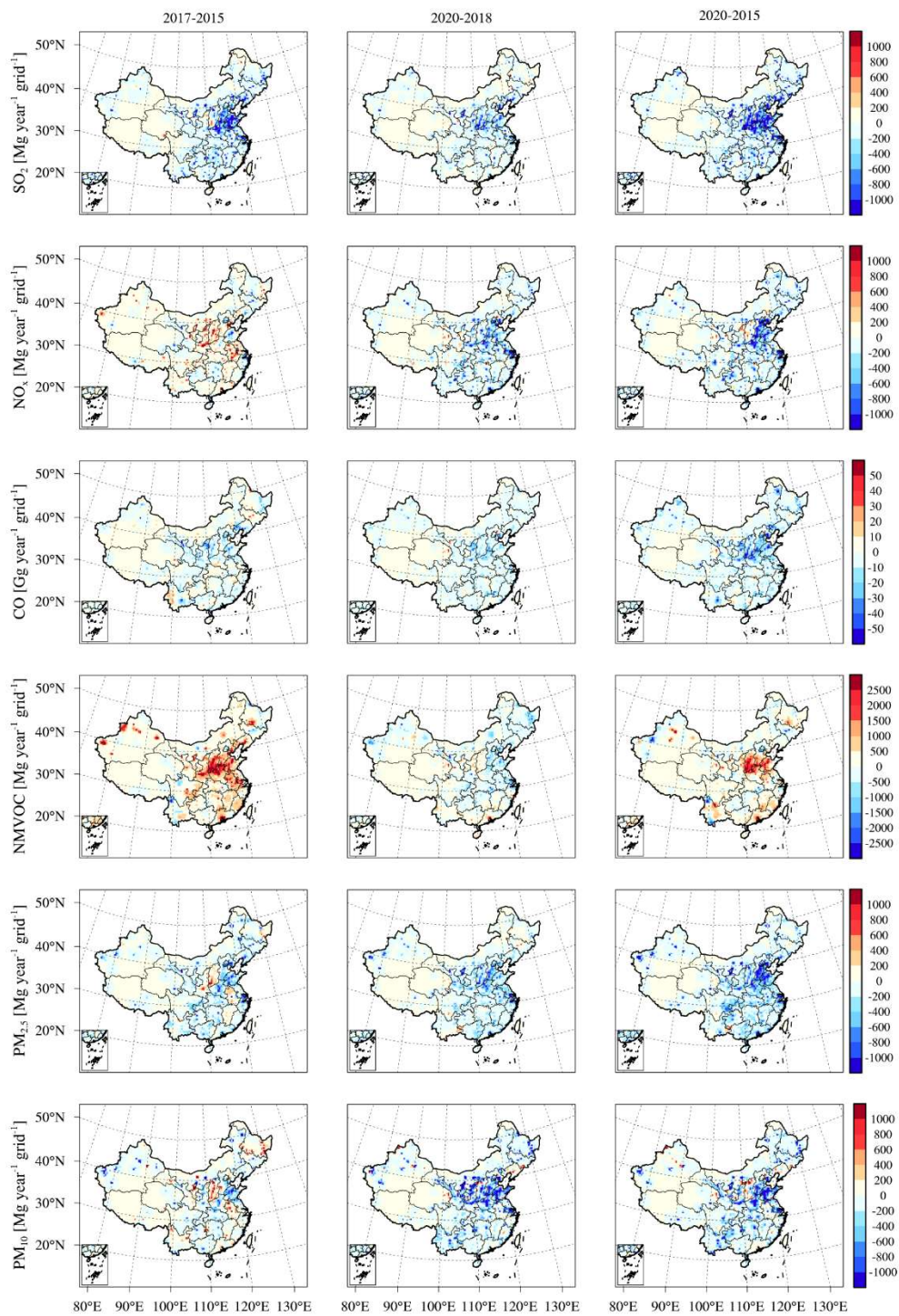
1245

Figure 8: Spatial distributions of the emission changes of different species during 2015–2017 (left panels), 2018–2020 (middle panels), and 2015–2020 (right panels) obtained from CAQIEI from 2013 to 2020.
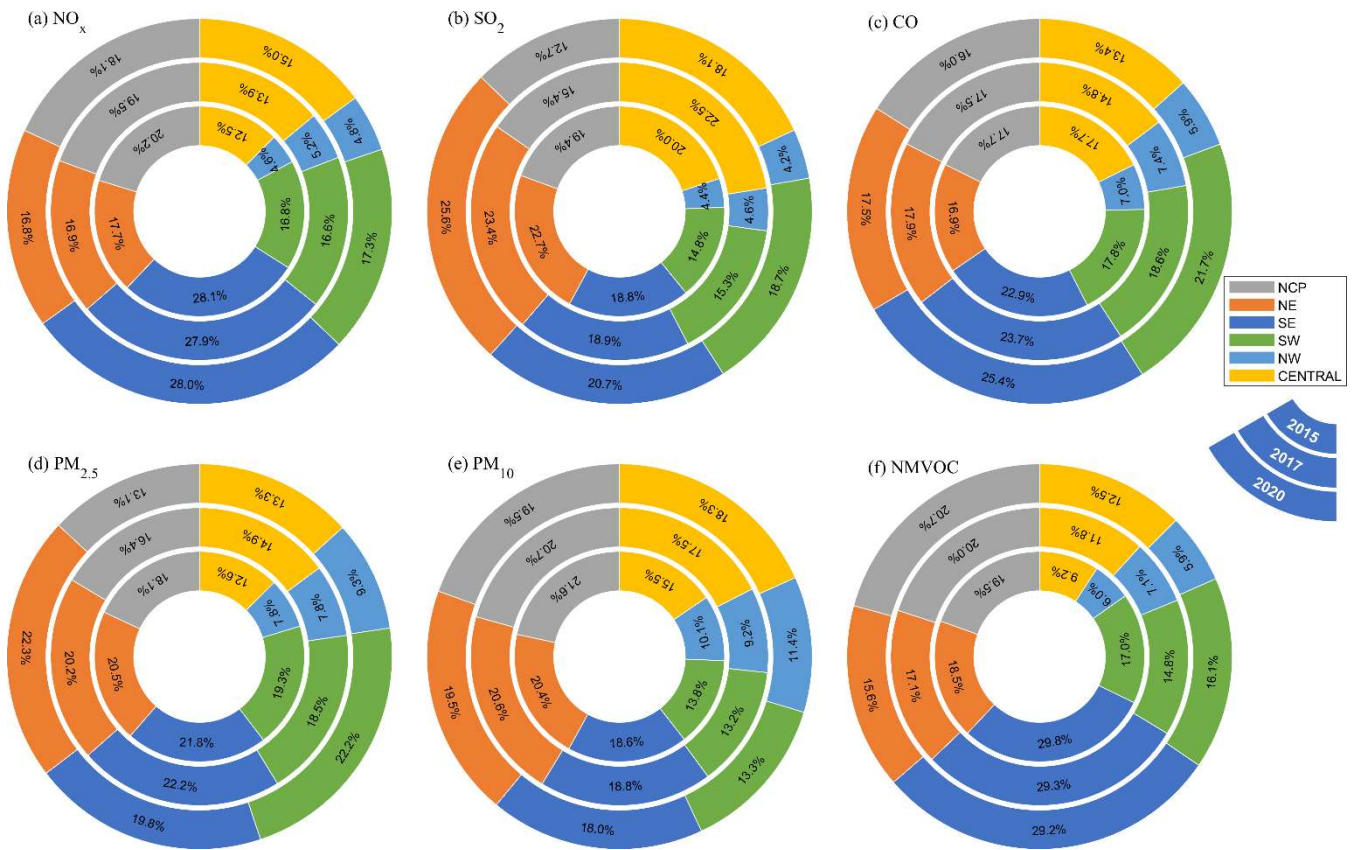
1248

1249 **Figure 9: Emission distributions of (a) NOₓ, (b) SO₂, (c) CO, (d) PM2.5, € PM₁₀, and (f) NMVOCs among different regions in China**
1250 **obtained from CAQIEI in 2015, 2017 and 2020.**

1251

1252
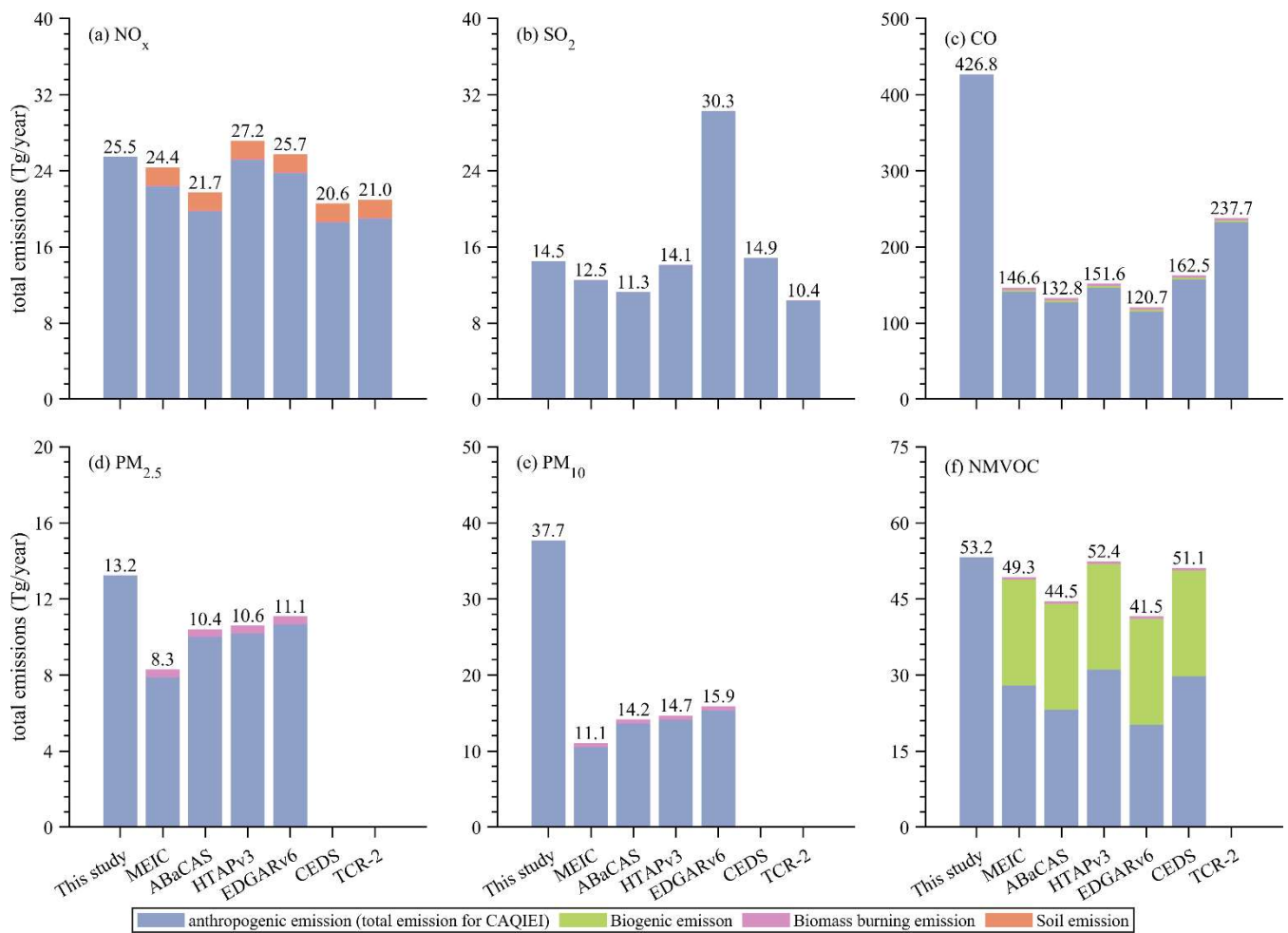
1253

Figure 10: Comparisons of the averaged emissions of (a) NO_x, (b) SO_2, (c) CO, (d) $PM_{2.5}$, (e) PM_{10}, and (f) NMVOCs over China from 2015 to 2018 between CAQIEI and previous inventories added with natural sources.

1254
1255

1256
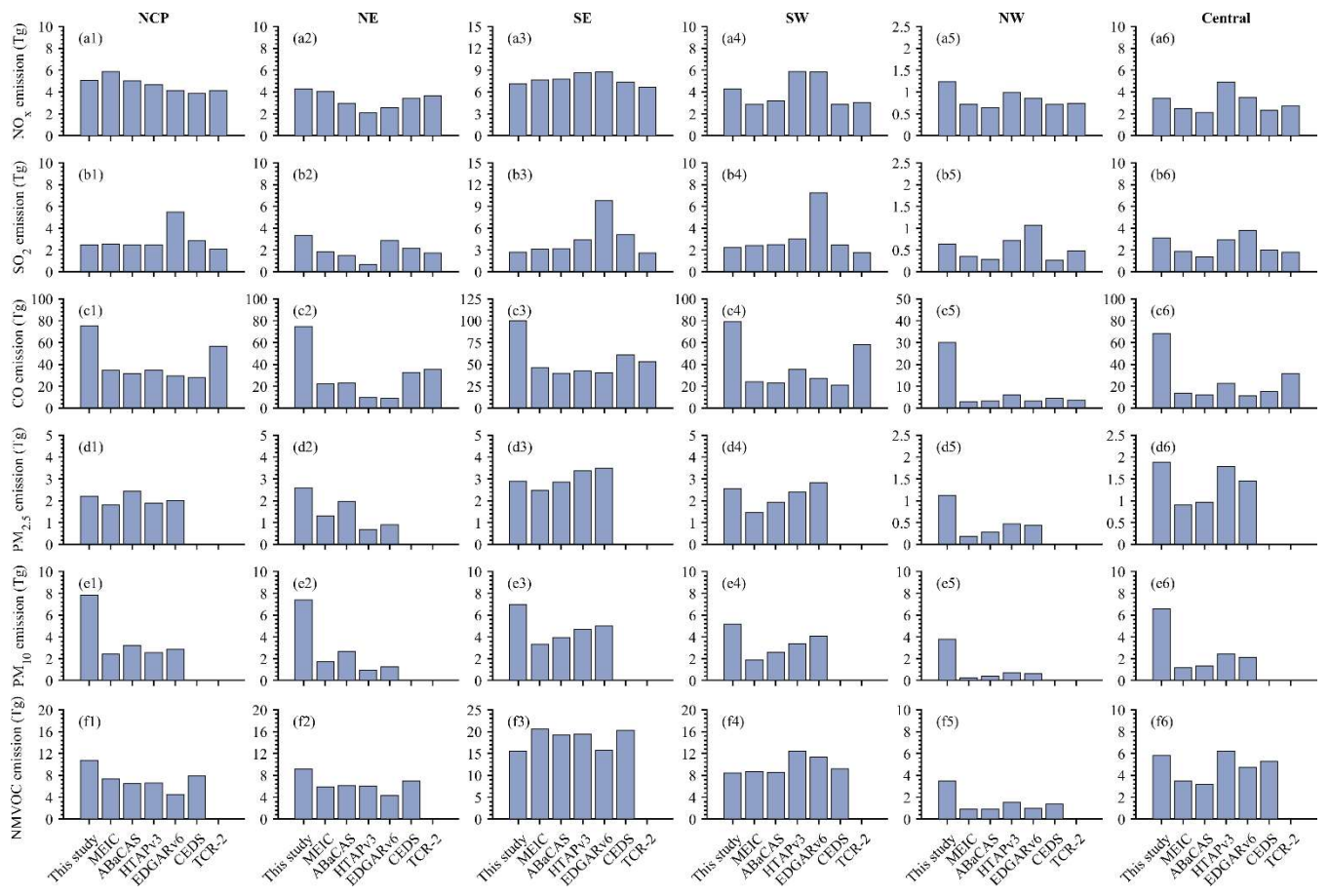
1257

Figure 11: Comparisons of the averaged emissions of (a) NO$_x$, (b) SO$_2$, (c) CO, (d) PM$_{2.5}$, (e) PM$_{10}$, and (f) NMVOCs over different regions in China from 2015 to 2018 between CAQIEI and previous inventories added with natural sources.

1258
1259

1260

1261

1262

1263

1264
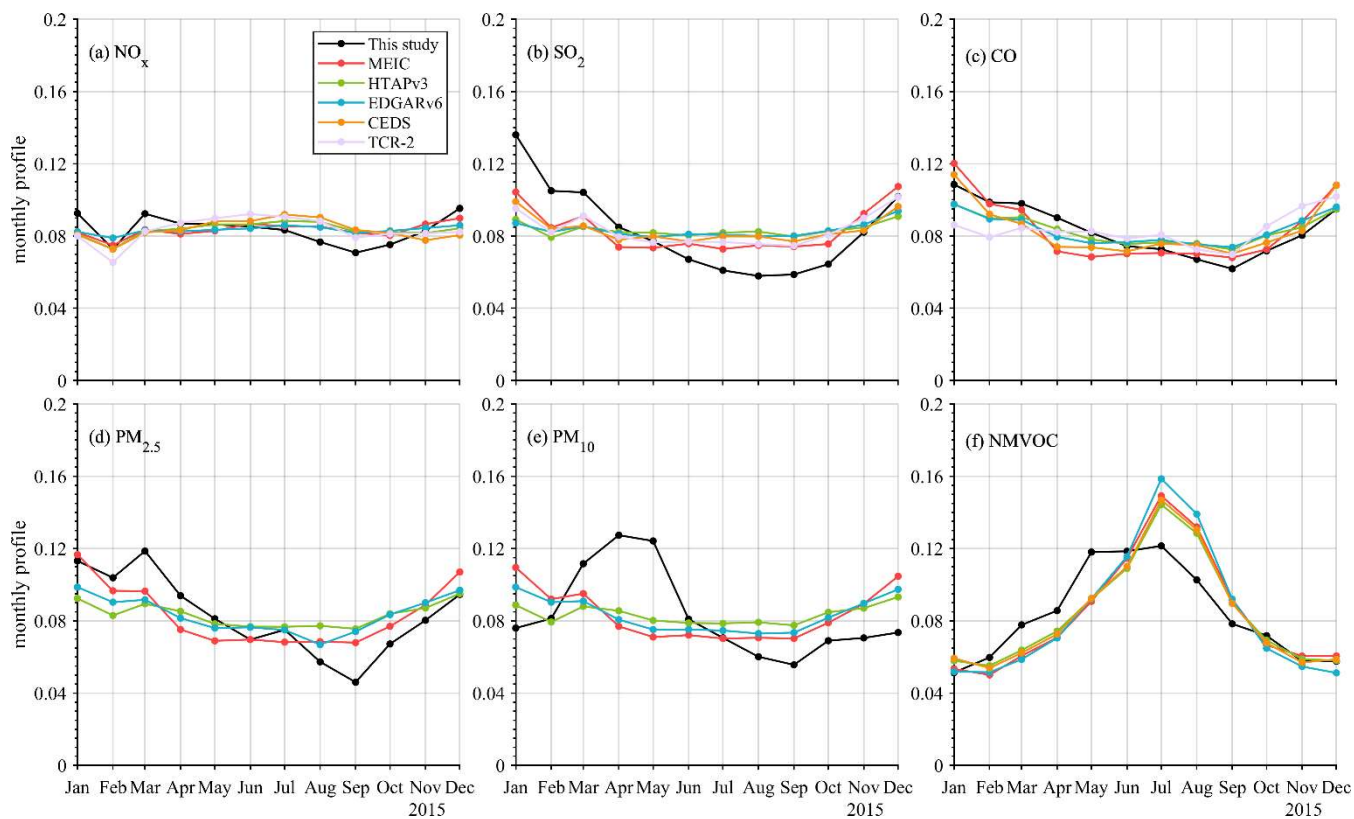
Figure 12: Comparisons of the monthly profiles of (a) NO$_x$, (b) SO$_2$, (c) CO, (d) PM$_{2.5}$, (e) PM$_{10}$, and (f) NMVOCs over China averaged from 2015 to 2018 between CAQIEI and previous inventories added with natural sources.
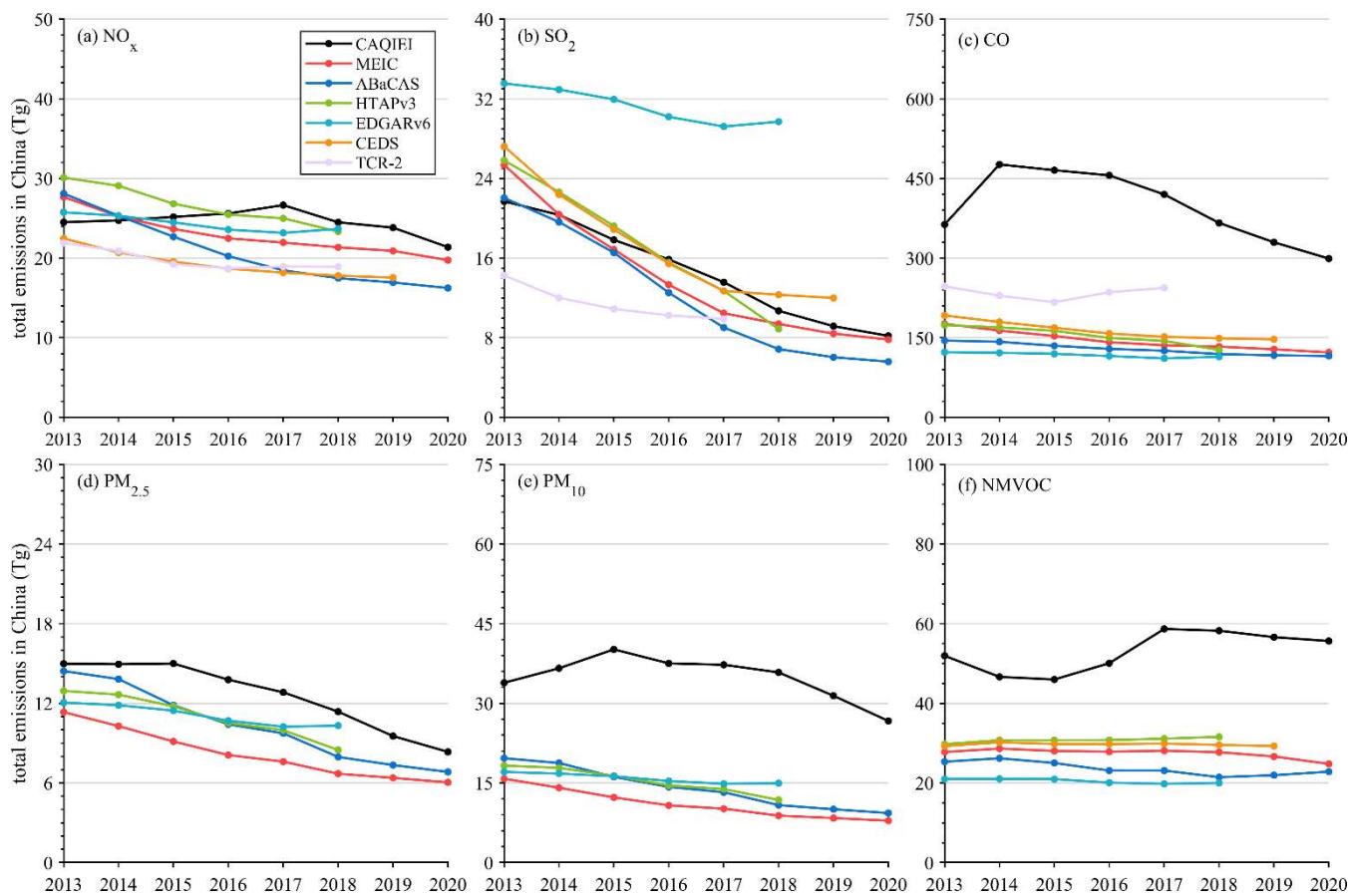
Figure 13: Time series of annual emissions of (a) NO_x, (b) SO_2, (c) CO, (d) $PM_{2.5}$, (e) PM_{10} and (f) NMVOC over China from 2013 to 2020 obtained from CAQIEI and previous inventories. Note that the natural sources were not included in the previous inventories in this figure.
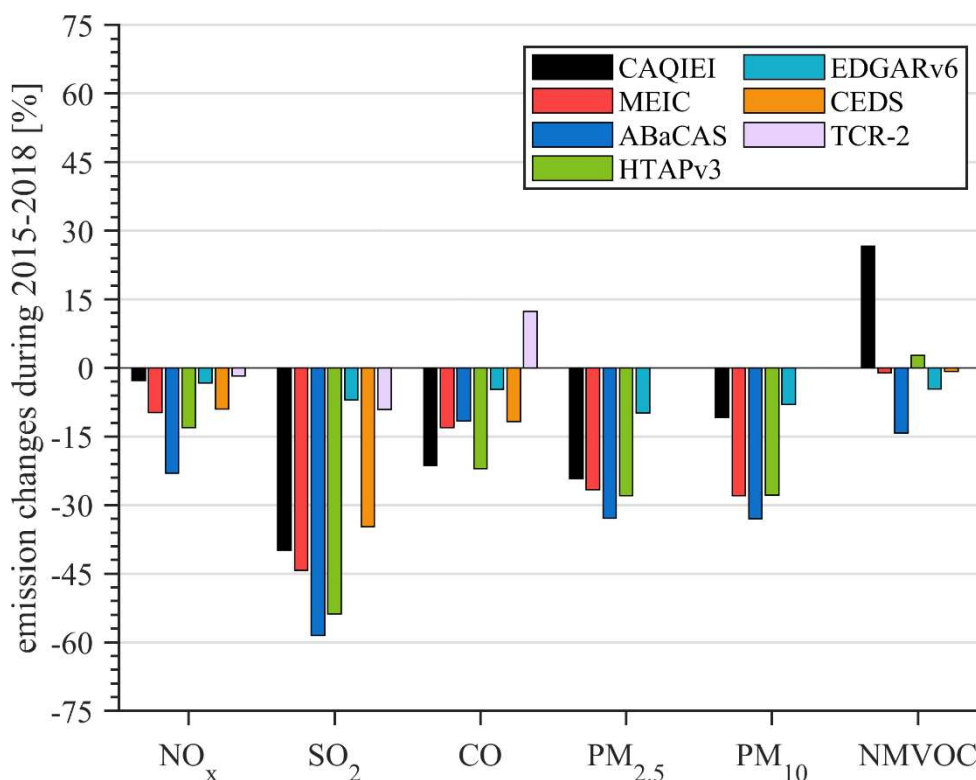
Figure 14: Comparisons of the calculated emission changes of NO$_x$, SO$_2$, CO, PM$_{2.5}$, PM$_{10}$, and NMVOCs over China from 2015 to 2018 between CAQIEI and previous inventories. Note that the natural sources were not included in the calculation of the emission changes in this figure.

Author contributions

X.T., Z.W., and J.Z. conceived and designed the project; L.K., H.W., X.T., and L.W. established the data assimilation system; Q.W. and L.K. performed the meteorology simulations; L.K., H.C., and J.L. conducted the ensemble simulation with the NAQPMS model; J.L., L.Z., W.W., B.L., Q.W., D.C. and Y.P. provided the air quality monitoring data; H.W. performed the quality control of the observation data; and L.K. performed the inversion estimation, generated the figures, and wrote the paper, with comments provided by G.R.C.

Competing interests

The authors declare no competing financial interest.

Acknowledgements

Financial support

References

Athanasopoulou, E., Tombrou, M., Pandis, S. N., and Russell, A. G.: The role of sea-salt emissions and heterogeneous chemistry in the air quality of polluted coastal areas, Atmos. Chem. Phys., 8, 5755-5769, https://doi.org/10.5194/acp-8-5755-2008, 2008.

Bergamaschi, P., Hein, R., Heimann, M., and Crutzen, P. J.: Inverse modeling of the global CO cycle 1. Inversion of CO mixing ratios, J. Geophys. Res.-Atmos., 105, 1909-1927, https://doi.org/10.1029/1999jd900818, 2000.

Bobbink, R., Hornung, M., and Roelofs, J. G. M.: The effects of air-borne nitrogen pollutants on species diversity in natural and semi-natural European vegetation, J. Ecol., 86, 717-738, https://doi.org/10.1046/j.1365-2745.1998.8650717.x, 1998.

Brasseur, G. P., Hauglustaine, D. A., Walters, S., Rasch, P. J., Müller, J.-F., Granier, C., and Tie, X. X.: MOZART, a global chemical transport model for ozone and related chemical tracers: 1. Model description, J. Geophys. Res.-Atmos., 103, 28265-28289, https://doi.org/10.1029/98JD02397, 1998.

Cao, H. S., Fu, T. M., Zhang, L., Henze, D. K., Miller, C. C., Lerot, C., Abad, G. G., De Smedt, I., Zhang, Q., van Roozendael, M., Hendrick, F., Chance, K., Li, J., Zheng, J. Y., and Zhao, Y. H.: Adjoint inversion of Chinese non-methane volatile organic compound emissions using space-based observations of formaldehyde and glyoxal, Atmos. Chem. Phys., 18, 15017-15046, https://10.5194/acp-18-15017-2018, 2018.

Cohen, A. J., Brauer, M., Burnett, R., Anderson, H. R., Frostad, J., Estep, K., Balakrishnan, K., Brunekreef, B., Dandona, L., Dandona, R., Feigin, V., Freedman, G., Hubbell, B., Jobling, A., Kan, H., Knibbs, L., Liu, Y., Martin, R., Morawska, L., Pope, C. A., Shin, H., Straif, K., Shaddick, G., Thomas, M., van Dingenen, R., van Donkelaar, A., Vos, T., Murray, C. J. L., and Forouzanfar, M. H.: Estimates and 25-year trends of the global burden of disease attributable to ambient air pollution: an analysis of data from the Global Burden of Diseases Study 2015, Lancet, 389, 1907-1918, https://doi.org/10.1016/s0140-6736(17)30505-6, 2017.

Crippa, M., Guizzardi, D., Butler, T., Keating, T., Wu, R., Kaminski, J., Kuenen, J., Kurokawa, J., Chatani, S., Morikawa, T., Pouliot, G., Racine, J., Moran, M. D., Klimont, Z., Manseau, P. M., Mashayekhi, R., Henderson, B. H., Smith, S. J., Suchyta, H., Muntean, M., Solazzo, E., Banja, M., Schaaf, E., Pagani, F., Woo, J. H., Kim, J., Monforti-Ferrario, F., Pisoni, E., Zhang, J., Niemi, D., Sassi, M., Ansari, T., and Foley, K.: The HTAP_v3 emission mosaic: merging regional and global monthly emissions (2000–2018) to support air quality modelling and policies, Earth Syst. Sci. Data, 15, 2667-2694, https://doi.org/10.5194/essd-15-2667-2023, 2023.

Dee, D. P. and Da Silva, A. M.: Data assimilation in the presence of forecast bias, Q. J. R. Meteorol. Soc., 124, 269-295, https://doi.org/10.1002/qj.49712454512, 1998.

Du, Q., Zhao, C., Zhang, M., Dong, X., Chen, Y., Liu, Z., Hu, Z., Zhang, Q., Li, Y., Yuan, R., and Miao, S.: Modeling diurnal variation of surface $PM_{2.5}$ concentrations over East China with WRF-Chem: impacts from boundary-layer mixing and anthropogenic emission, Atmos. Chem. Phys., 20, 2839-2863, https://doi.org/10.5194/acp-20-2839-2020, 2020.

Elbern, H., Strunk, A., Schmidt, H., and Talagrand, O.: Emission rate and chemical state estimation by 4-dimensional variational inversion, Atmos. Chem. Phys., 7, 3749-3769, https://doi.org/10.5194/acp-7-3749-2007, 2007.

Elguindi, N., Granier, C., Stavrakou, T., Darras, S., Bauwens, M., Cao, H., Chen, C., van der Gon, H., Dubovik, O., Fu, T. M., Henze, D. K., Jiang, Z., Keita, S., Kuenen, J. J. P., Kurokawa, J., Liousse, C., Miyazaki, K., Muller, J. F., Qu, Z., Solmon, F., and Zheng, B.: Intercomparison of Magnitudes and Trends in Anthropogenic Surface Emissions From Bottom-Up Inventories, Top-Down Estimates, and Emission Scenarios, Earth Future, 8, 20, https://doi.org/10.1029/2020ef001520, 2020.

Evensen, G.: Sequential data assimilation with a nonlinear quasi-geostrophic model using Monte Carlo methods to forecast error statistics, J. Geophys. Res.-Oceans, 99, 10143-10162, https://doi.org/10.1029/94JC00572, 1994.

Fan, H., Zhao, C., Yang, Y., and Yang, X.: Spatio-Temporal Variations of the PM2.5/PM10 Ratios and Its Application to Air Pollution Type Classification in China, Front. Environ. Sci., 9, https://doi.org/10.3389/fenvs.2021.692440, 2021.

Feng, S., Jiang, F., Qian, T., Wang, N., Jia, M., Zheng, S., Chen, J., Ying, F., and Ju, W.: Constraint of non-methane volatile organic compound emissions with TROPOMI HCHO observations and its impact on summertime surface ozone simulation over China, EGUsphere, 2024, 1-34, https://10.5194/egusphere-2023-2654, 2024.

Feng, S., Jiang, F., Wu, Z., Wang, H., Ju, W., and Wang, H.: CO Emissions Inferred From Surface CO Observations Over China in December 2013 and 2017, J. Geophys. Res.-Atmos., 125, e2019JD031808, https://doi.org/10.1029/2019JD031808, 2020.

Fu, X., Wang, T., Gao, J., Wang, P., Liu, Y. M., Wang, S. X., Zhao, B., and Xue, L. K.: Persistent Heavy Winter Nitrate Pollution Driven by Increased Photochemical Oxidants in Northern China, Environ. Sci. Technol., 54, 3881-3889, https://doi.org/10.1021/acs.est.9b07248, 2020.

Gaubert, B., Emmons, L. K., Raeder, K., Tilmes, S., Miyazaki, K., Arellano Jr, A. F., Elguindi, N., Granier, C., Tang, W., Barré, J., Worden, H. M., Buchholz, R. R., Edwards, D. P., Franke, P., Anderson, J. L., Saunois, M., Schroeder, J., Woo, J. H., Simpson, I. J., Blake, D. R., Meinardi, S., Wennberg, P. O., Crounse, J., Teng, A., Kim, M., Dickerson, R. R., He, H., Ren, X., Pusede, S. E., and Diskin, G. S.: Correcting model biases of CO in East Asia: impact on oxidant distributions during KORUS-AQ, Atmos. Chem. Phys., 20, 14617-14647, https://doi.org/10.5194/acp-20-14617-2020, 2020.

Goldberg, D. L., Saide, P. E., Lamsal, L. N., de Foy, B., Lu, Z. F., Woo, J. H., Kim, Y., Kim, J., Gao, M., Carmichael, G., and Streets, D. G.: A top-down assessment using OMI NO2 suggests an underestimate in the NOx emissions inventory in Seoul, South Korea, during KORUS-AQ, Atmos. Chem. Phys., 19, 1801-1818, https://10.5194/acp-19-1801-2019, 2019.

Granier, C., Lamarque, J., Mieville, A., Muller, J., Olivier, J., Orlando, J., Peters, J., Petron, G., Tyndall, G., and Wallens, S.: POET, a database of surface emissions of ozone precursors, available at: http://www.aero.jussieu.fr/projet/ACCENT/POET.php (last access: 09 October 2023), 2005.

Hauglustaine, D. A., Brasseur, G. P., Walters, S., Rasch, P. J., Muller, J. F., Emmons, L. K., and Carroll, C. A.: MOZART, a global chemical transport model for ozone and related chemical tracers 2. Model results and evaluation, J. Geophys. Res.-Atmos., 103, 28291-28335, https://doi.org/10.1029/98jd02398, 1998.

Henze, D. K., Seinfeld, J. H., and Shindell, D. T.: Inverse modeling and mapping US air quality influences of inorganic PM2.5 precursor emissions using the adjoint of GEOS-Chem, Atmos. Chem. Phys., 9, 5877-5903, https://doi.org/10.5194/acp-9-5877-2009, 2009.

Hernández, D. L., Vallano, D. M., Zavaleta, E. S., Tzankova, Z., Pasari, J. R., Weiss, S., Selmants, P. C., and Morozumi, C.: Nitrogen Pollution Is Linked to US Listed Species Declines, BioScience, 66, 213-222, https://doi.org/10.1093/biosci/biw003, 2016.

Jalkanen, J. P., Johansson, L., Kukkonen, J., Brink, A., Kalli, J., and Stipa, T.: Extension of an assessment model of ship traffic exhaust emissions for particulate matter and carbon monoxide, Atmos. Chem. Phys., 12, 2641-2659, https://doi.org/10.5194/acp-12-2641-2012, 2012.

Janssens-Maenhout, G., Crippa, M., Guizzardi, D., Dentener, F., Muntean, M., Pouliot, G., Keating, T., Zhang, Q., Kurokawa, J., Wankmuller, R., van der Gon, H. D., Kuenen, J. J. P., Klimont, Z., Frost, G., Darras, S., Koffi, B., and Li, M.: HTAP_v2.2: a mosaic of regional and global emission grid maps for 2008 and 2010 to study hemispheric transport of air pollution, Atmos. Chem. Phys., 15, 11411-11432, https://doi.org/10.5194/acp-15-11411-2015, 2015.

Jiang, Z., Worden, J. R., Worden, H., Deeter, M., Jones, D. B. A., Arellano, A. F., and Henze, D. K.: A 15-year record of CO emissions constrained by MOPITT CO observations, Atmos. Chem. Phys., 17, 4565-4583, https://doi.org/10.5194/acp-17-4565-2017, 2017.

Kaiser, J. W., Heil, A., Andreae, M. O., Benedetti, A., Chubarova, N., Jones, L., Morcrette, J. J., Razinger, M., Schultz, M. G., Suttie, M., and van der Werf, G. R.: Biomass burning emissions estimated with a global fire assimilation system based on observed fire radiative power, Biogeosciences, 9, 527-554, https://doi.org/10.5194/bg-9-527-2012, 2012.

Kan, H., Chen, R., and Tong, S.: Ambient air pollution, climate change, and population health in China, Environ. Int., 42, 10-19, https://doi.org/10.1016/j.envint.2011.03.003, 2012.

Kang, J.-Y., Yoon, S.-C., Shao, Y., and Kim, S.-W.: Comparison of vertical dust flux by implementing three dust emission schemes in WRF/Chem, J. Geophys. Res.-Atmos., 116, https://doi.org/10.1029/2010JD014649, 2011

Kong, L., Tang, X., Wang, Z. F., Zhu, J., Li, J. J., Wu, H. J., Wu, Q. Z., Chen, H. S., Zhu, L. L., Wang, W., Liu, B., Wang, Q., Chen D. H., Pan Y. P., Li, J., Wu, L., and Carmichael, G. R.: Inversed Emission Inventory for Chinese Air Quality (CAQIEI) version 1.0, Science Data Bank [dataset], https://doi.org/10.57760/sciencedb.13151, 2023.

Kong, L., Tang, X., Zhu, J., Wang, Z., Pan, Y., Wu, H., Wu, L., Wu, Q., He, Y., Tian, S., Xie, Y., Liu, Z., Sui, W., Han, L., and Carmichael, G.: Improved Inversion of Monthly Ammonia Emissions in China Based on the Chinese Ammonia Monitoring Network and Ensemble Kalman Filter, Environ. Sci. Technol., 53, 12529-12538, https://doi.org/10.1021/acs.est.9b02701, 2019.

Kong, L., Tang, X., Zhu, J., Wang, Z., Sun, Y., Fu, P., Gao, M., Wu, H., Lu, M., Wu, Q., Huang, S., Sui, W., Li, J., Pan, X., Wu, L., Akimoto, H., and Carmichael, G. R.: Unbalanced emission reductions of different species and sectors in China during COVID-19 lockdown derived by multi-species surface observation assimilation, Atmos. Chem. Phys., 23, 6217-6240, https://doi.org/10.5194/acp-23-6217-2023, 2023.

Kong, L., Tang, X., Zhu, J., Wang, Z., Li, J., Wu, H., Wu, Q., Chen, H., Zhu, L., Wang, W., Liu, B., Wang, Q., Chen, D., Pan, Y., Song, T., Li, F., Zheng, H., Jia, G., Lu, M., Wu, L., and Carmichael, G. R.: A 6-year-long (2013–2018) high-resolution air quality reanalysis dataset in China based on the assimilation of surface observations from CNEMC, Earth Syst. Sci. Data, 13, 529-570, https://doi.org/10.5194/essd-13-529-2021, 2021.

Kong, L., Tang, X., Zhu, J., Wang, Z., Fu, J. S., Wang, X., Itahashi, S., Yamaji, K., Nagashima, T., Lee, H. J., Kim, C. H., Lin, C. Y., Chen, L., Zhang, M., Tao, Z., Li, J., Kajino, M., Liao, H., Wang, Z., Sudo, K., Wang, Y., Pan, Y., Tang, G., Li, M., Wu, Q., Ge, B., and Carmichael, G. R.: Evaluation and uncertainty investigation of the NO2, CO and NH3 modeling over China under the framework of MICS-Asia III, Atmos. Chem. Phys., 20, 181-202, https://doi.org/10.5194/acp-20-181-2020, 2020.

Koohkan, M. R., Bocquet, M., Roustan, Y., Kim, Y., and Seigneur, C.: Estimation of volatile organic compound emissions for Europe using data assimilation, Atmos. Chem. Phys., 13, 5887-5905, https://doi.org/10.5194/acp-13-5887-2013, 2013.

Koukouli, M. E., Theys, N., Ding, J. Y., Zyrichidou, I., Mijling, B., Balis, D., and Johannes, V. R.: Updated SO2 emission estimates over China using OMI/Aura observations, Atmos. Meas. Tech., 11, 1817-1832, 10.5194/amt-11-1817-2018, 2018.

Krotkov, N. A., McLinden, C. A., Li, C., Lamsal, L. N., Celarier, E. A., Marchenko, S. V., Swartz, W. H., Bucsela, E. J., Joiner, J., Duncan, B. N., Boersma, K. F., Veefkind, J. P., Levelt, P. F., Fioletov, V. E., Dickerson, R. R., He, H., Lu, Z. F., and Streets, D. G.: Aura OMI observations of regional SO2 and NO2 pollution changes from 2005 to 2015, Atmos. Chem. Phys., 16, 4605-4629, https://doi.org/10.5194/acp-16-4605-2016, 2016.

Krupa, S. V.: Effects of atmospheric ammonia (NH3) on terrestrial vegetation: a review, Environ. Pollut., 124, 179-221, https://doi.org/10.1016/s0269-7491(02)00434-7, 2003.

Kurokawa, J. and Ohara, T.: Long-term historical trends in air pollutant emissions in Asia: Regional Emission inventory in ASia (REAS) version 3, Atmos. Chem. Phys., 20, 12761-12793, https://doi.org/10.5194/acp-20-12761-2020, 2020.

Kurokawa, J., Ohara, T., Morikawa, T., Hanayama, S., Janssens-Maenhout, G., Fukui, T., Kawashima, K., and Akimoto, H.: Emissions of air pollutants and greenhouse gases over Asian regions during 2000-2008: Regional Emission inventory in ASia (REAS) version 2, Atmos. Chem. Phys., 13, 11019-11058, https://doi.org/10.5194/acp-13-11019-2013, 2013.

Lei, L., Zhou, W., Chen, C., He, Y., Li, Z. J., Sun, J. X., Tang, X., Fu, P. Q., Wang, Z. F., and Sun, Y. L.: Long-term characterization of aerosol chemistry in cold season from 2013 to 2020 in Beijing, China, Environ. Pollut., 268, 9, 10.1016/j.envpol.2020.115952, 2021.

Li, C., McLinden, C., Fioletov, V., Krotkov, N., Carn, S., Joiner, J., Streets, D., He, H., Ren, X., Li, Z., and Dickerson, R. R.: India Is Overtaking China as the World's Largest Emitter of Anthropogenic Sulfur Dioxide, Sci Rep, 7, 14304, https://doi.org/10.1038/s41598-017-14639-8, 2017a.

Li, H., Cheng, J., Zhang, Q., Zheng, B., Zhang, Y., Zheng, G., and He, K.: Rapid transition in winter aerosol composition in Beijing from 2014 to 2017: response to clean air actions, Atmos. Chem. Phys., 19, 11485-11499, https://doi.org/10.5194/acp-19-11485-2019, 2019a.

Li, J., Wang, Z., Zhuang, G., Luo, G., Sun, Y., and Wang, Q.: Mixing of Asian mineral dust with anthropogenic pollutants over East Asia: a model case study of a super-duststorm in March 2010, Atmos. Chem. Phys., 12, 7591-7607, 2012.

Li, K., Jacob, D. J., Liao, H., Shen, L., Zhang, Q., and Bates, K. H.: Anthropogenic drivers of 2013-2017 trends in summer surface ozone in China, Proc. Natl. Acad. Sci. U.S.A., 116, 422-427, https://doi.org/10.1073/pnas.1812168116, 2019b.

Li, L. Y., Yang, W. Z., Xie, S. D., and Wu, Y.: Estimations and uncertainty of biogenic volatile organic compound emission inventory in China for 2008-2018, Sci. Total Environ., 733, 10, https://doi.org/10.1016/j.scitotenv.2020.139301, 2020a.

Li, M., Zhang, Q., Zheng, B., Tong, D., Lei, Y., Liu, F., Hong, C. P., Kang, S. C., Yan, L., Zhang, Y. X., Bo, Y., Su, H., Cheng, Y. F., and He, K. B.: Persistent growth of anthropogenic non-methane volatile organic compound (NMVOC) emissions in China during 1990-2017: drivers, speciation and ozone formation potential, Atmos. Chem. Phys., 19, 8897-8913, https://doi.org/10.5194/acp-19-8897-2019, 2019c.

Li, M., Zhang, Q., Kurokawa, J. I., Woo, J. H., He, K., Lu, Z., Ohara, T., Song, Y., Streets, D. G., Carmichael, G. R., Cheng, Y., Hong, C., Huo, H., Jiang, X., Kang, S., Liu, F., Su, H., and Zheng, B.: MIX: a mosaic Asian anthropogenic emission inventory under the international collaboration framework of the MICS-Asia and HTAP, Atmos. Chem. Phys., 17, 935-963, https://doi.org/10.5194/acp-17-935-2017, 2017b.

Li, N., Long, X., Tie, X. X., Cao, J. J., Huang, R. J., Zhang, R., Feng, T., Liu, S. X., and Li, G. H.: Urban dust in the Guanzhong basin of China, part II: A case study of urban dust pollution using the WRF-Dust model, Sci. Total Environ., 541, 1614-1624, https://doi.org/10.1016/j.scitotenv.2015.10.028, 2016.

Li, R., Cui, L. L., Li, J. L., Zhao, A., Fu, H. B., Wu, Y., Zhang, L. W., Kong, L. D., and Chen, J. M.: Spatial and temporal variation of particulate matter and gaseous pollutants in China during 2014-2016, Atmos. Environ., 161, 235-246, https://doi.org/10.1016/j.atmosenv.2017.05.008, 2017c.

Li, S., Wang, S., Wu, Q., Zhang, Y., Ouyang, D., Zheng, H., Han, L., Qiu, X., Wen, Y., Liu, M., Jiang, Y., Yin, D., Liu, K., Zhao, B., Zhang, S., Wu, Y., and Hao, J.: Emission trends of air pollutants and CO2 in China from 2005 to 2021, Earth Syst. Sci. Data, 15, 2279-2294, https://doi.org/10.5194/essd-15-2279-2023, 2023.

Li, W., Shao, L., Wang, W., Li, H., Wang, X., Li, Y., Li, W., Jones, T., and Zhang, D.: Air quality improvement in response to intensified control strategies in Beijing during 2013-2019, Sci. Total Environ., 744, https://doi.org/10.1016/j.scitotenv.2020.140776, 2020b.

Liu, J., Tong, D., Zheng, Y. X., Cheng, J., Qin, X. Y., Shi, Q. R., Yan, L., Lei, Y., and Zhang, Q.: Carbon and air pollutant emissions from China's cement industry 1990-2015: trends, evolution of technologies, and drivers, Atmos. Chem. Phys., 21, 1627-1647, https://doi.org/10.5194/acp-21-1627-2021, 2021.

Liu, J., Mauzerall, D. L., Chen, Q., Zhang, Q., Song, Y., Peng, W., Klimont, Z., Qiu, X. H., Zhang, S. Q., Hu, M., Lin, W. L., Smith, K. R., and Zhu, T.: Air pollutant emissions from Chinese households: A major and underappreciated ambient pollution source, Proc. Natl. Acad. Sci. U.S.A., 113, 7756-7761, https://doi.org/10.1073/pnas.1604537113, 2016.

Lu, X., Zhang, L., Wang, X. L., Gao, M., Li, K., Zhang, Y. Z., Yue, X., and Zhang, Y. H.: Rapid Increases in Warm-Season Surface Ozone and Resulting Health Impact in China Since 2013, Environ. Sci. Technol. Lett., 7, 240-247, https://doi.org/10.1021/acs.estlett.0c00171, 2020.

Lu, X., Hong, J. Y., Zhang, L., Cooper, O. R., Schultz, M. G., Xu, X. B., Wang, T., Gao, M., Zhao, Y. H., and Zhang, Y. H.: Severe Surface Ozone Pollution in China: A Global Perspective, Environ. Sci. Technol. Lett., 5, 487-494, https://doi.org/10.1021/acs.estlett.8b00366, 2018.

Ma, C. Q., Wang, T. J., Mizzi, A. P., Anderson, J. L., Zhuang, B. L., Xie, M., and Wu, R. S.: Multiconstituent Data Assimilation With WRF-Chem/DART: Potential for Adjusting Anthropogenic Emissions and Improving Air Quality Forecasts Over Eastern China, J. Geophys. Res.-Atmos., 124, 7393-7412, https://doi.org/10.1029/2019jd030421, 2019.

Martin, S. T., Hung, H. M., Park, R. J., Jacob, D. J., Spurr, R. J. D., Chance, K. V., and Chin, M.: Effects of the physical state of tropospheric ammonium-sulfate-nitrate particles on global aerosol direct radiative forcing, Atmos. Chem. Phys., 4, 183-214, https://doi.org/10.5194/acp-4-183-2004, 2004.

McDuffie, E. E., Smith, S. J., O'Rourke, P., Tibrewal, K., Venkataraman, C., Marais, E. A., Zheng, B., Crippa, M., Brauer, M., and Martin, R. V.: A global anthropogenic emission inventory of atmospheric pollutants from sector- and fuel-specific sources (1970-2017): an application of the Community Emissions Data System (CEDS), Earth Syst. Sci. Data, 12, 3413-3442, https://doi.org/10.5194/essd-12-3413-2020, 2020.

Miyazaki, K. and Eskes, H.: Constraints on surface NOx emissions by assimilating satellite observations of multiple species, Geophys. Res. Lett., 40, 4745-4750, https://doi.org/10.1002/grl.50894, 2013.

Miyazaki, K., Bowman, K. W., Yumimoto, K., Walker, T., and Sudo, K.: Evaluation of a multi-model, multi-constituent assimilation framework for tropospheric chemical reanalysis, Atmos. Chem. Phys., 20, 931-967, https://doi.org/10.5194/acp-20-931-2020, 2020a.

Miyazaki, K., Eskes, H. J., Sudo, K., Takigawa, M., van Weele, M., and Boersma, K. F.: Simultaneous assimilation of satellite NO2, O-3, CO, and HNO3 data for the analysis of tropospheric chemical composition and emissions, Atmos. Chem. Phys., 12, 9545-9579, https://doi.org/10.5194/acp-12-9545-2012, 2012.

Miyazaki, K., Bowman, K., Sekiya, T., Eskes, H., Boersma, F., Worden, H., Livesey, N., Payne, V. H., Sudo, K., Kanaya, Y., Takigawa, M., and Ogochi, K.: Updated tropospheric chemistry reanalysis and emission estimates, TCR-2, for 2005–2018, Earth Syst. Sci. Data, 12, 2223-2259, https://doi.org/10.5194/essd-12-2223-2020, 2020b.

Müller, J.-F., Stavrakou, T., Bauwens, M., George, M., Hurtmans, D., Coheur, P.-F., Clerbaux, C., and Sweeney, C.: Top-Down CO Emissions Based On IASI Observations and Hemispheric Constraints on OH Levels, Geophys. Res. Lett., 45, 1621-1629, https://doi.org/10.1002/2017GL076697, 2018.

Muller, J. F., Stavrakou, T., Bauwens, M., George, M., Hurtmans, D., Coheur, P. F., Clerbaux, C., and Sweeney, C.: Top-Down CO Emissions Based On IASI Observations and Hemispheric Constraints on OH Levels, Geophys. Res. Lett., 45, 1621-1629, https://doi.org/10.1002/2017gl076697, 2018.

Paulot, F., Jacob, D. J., Pinder, R. W., Bash, J. O., Travis, K., and Henze, D. K.: Ammonia emissions in the United States, European Union, and China derived by high-resolution inversion of ammonium wet deposition data: Interpretation with a new agricultural emissions inventory (MASAGE_NH3), J. Geophys. Res.-Atmos., 119, 4343-4364, https://doi.org/10.1002/2013jd021130, 2014.

Peng, Z., Lei, L., Tan, Z. M., Zhang, M., Ding, A., and Kou, X.: Dynamics-based estimates of decline trend with fine temporal variations in China's PM2.5 emissions, EGUsphere, 2023, 1-34, https://doi.org/10.5194/egusphere-2023-755, 2023.

Peng, Z., Lei, L. L., Liu, Z. Q., Su, J. N., Ding, A. J., Ban, J. M., Chen, D., Kou, X. X., and Chu, K. K.: The impact of multi-species surface chemical observation assimilation on air quality forecasts in China, Atmos. Chem. Phys., 18, 18, https://doi.org/10.5194/acp-18-17387-2018, 2018.

Petron, G., Granier, C., Khattatov, B., Lamarque, J. F., Yudin, V., Muller, J. F., and Gille, J.: Inverse modeling of carbon monoxide surface emissions using Climate Monitoring and Diagnostics Laboratory network observations, J. Geophys. Res.-Atmos., 107, 23, https://doi.org/10.1029/2001jd001305, 2002.

Petron, G., Granier, C., Khattatov, B., Yudin, V., Lamarque, J. F., Emmons, L., Gille, J., and Edwards, D. P.: Monthly CO surface sources inventory based on the 2000-2001 MOPITT satellite data, Geophys. Res. Lett., 31, 5, https://doi.org/10.1029/2004gl020560, 2004.

Philip, S., Martin, R. V., Snider, G., Weagle, C. L., van Donkelaar, A., Brauer, M., Henze, D. K., Klimont, Z., Venkataraman, C., Guttikunda, S. K., and Zhang, Q.: Anthropogenic fugitive, combustion and industrial dust is a significant, underrepresented fine particulate matter source in global atmospheric models, Environ. Res. Lett., 12, 7, https://doi.org/10.1088/1748-9326/aa65a4, 2017.

Price, C., Penner, J., and Prather, M.: NOx from lightning .1. Global distribution based on lightning physics, J. Geophys. Res.-Atmos., 102, 5929-5941, https://doi.org/10.1029/96jd03504, 1997.

Prospero, J. M., Ginoux, P., Torres, O., Nicholson, S. E., and Gill, T. E.: Environmental characterization of global sources of atmospheric soil dust identified with the Nimbus 7 Total Ozone Mapping Spectrometer (TOMS) absorbing aerosol product, Rev. Geophys., 40, 31, https://doi.org/10.1029/2000rg000095, 2002.

Qu, Z., Henze, D. K., Capps, S. L., Wang, Y., Xu, X. G., Wang, J., and Keller, M.: Monthly top-down NO$_x$ emissions for China (2005-2012): A hybrid inversion method and trend analysis, J. Geophys. Res.-Atmos., 122, 4600-4625, https://doi.org/10.1002/2016jd025852, 2017.

Qu, Z., Henze, D. K., Li, C., Theys, N., Wang, Y., Wang, J., Wang, W., Han, J., Shim, C., Dickerson, R. R., and Ren, X. R.: SO2 Emission Estimates Using OMI SO2 Retrievals for 2005-2017, J. Geophys. Res.-Atmos., 124, 8336-8359, https://doi.org/10.1029/2019jd030243, 2019.

Randerson, J. T., Van Der Werf, G. R., Giglio, L., Collatz, G. J., and Kasibhatla, P. S.: Global Fire Emissions Database, Version 4.1 (GFEDv4), ORNL DAAC, Oak Ridge, Tennessee, USA, https://doi.org/10.3334/ORNLDAAC/1293, 2017.

Ren, J., Guo, F., and Xie, S.: Diagnosing ozone–NOx–VOC sensitivity and revealing causes of ozone increases in China based on 2013–2021 satellite retrievals, Atmos. Chem. Phys., 22, 15035-15047, https://10.5194/acp-22-15035-2022, 2022.

Sakov, P. and Oke, P. R.: A deterministic formulation of the ensemble Kalman filter: an alternative to ensemble square root filters, Tellus Ser. A-Dyn. Meteorol. Oceanol., 60, 361-371, https://doi.org/10.1111/j.1600-0870.2007.00299.x, 2008.

Sindelarova, K., Granier, C., Bouarar, I., Guenther, A., Tilmes, S., Stavrakou, T., Muller, J. F., Kuhn, U., Stefani, P., and Knorr, W.: Global data set of biogenic VOC emissions calculated by the MEGAN model over the last 30 years, Atmos. Chem. Phys., 14, 9317-9341, https://doi.org/10.5194/acp-14-9317-2014, 2014.

Song, C., Wu, L., Xie, Y., He, J., Chen, X., Wang, T., Lin, Y., Jin, T., Wang, A., Liu, Y., Dai, Q., Liu, B., Wang, Y.-n., and Mao, H.: Air pollution in China: Status and spatiotemporal variations, Environ. Pollut., 227, 334-347, https://doi.org/10.1016/j.envpol.2017.04.075, 2017.

Souri, A. H., Nowlan, C. R., Abad, G. G., Zhu, L., Blake, D. R., Fried, A., Weinheimer, A. J., Wisthaler, A., Woo, J. H., Zhang, Q., Miller, C. E. C., Liu, X., and Chance, K.: An inversion of NOx and non-methane volatile organic compound (NMVOC) emissions using satellite observations during the KORUS-AQ campaign and implications for surface ozone over East Asia, Atmos. Chem. Phys., 20, 9837-9854, https://10.5194/acp-20-9837-2020, 2020.

Stavrakou, T., Muller, J. F., Bauwens, M., De Smedt, I., Van Roozendael, M., De Maziere, M., Vigouroux, C., Hendrick, F., George, M., Clerbaux, C., Coheur, P. F., and Guenther, A.: How consistent are top-down hydrocarbon emissions based on formaldehyde observations from GOME-2 and OMI?, Atmos. Chem. Phys., 15, 11861-11884, https://10.5194/acp-15-11861-2015, 2015.

Stein, O., Schultz, M. G., Bouarar, I., Clark, H., Huijnen, V., Gaudel, A., George, M., and Clerbaux, C.: On the wintertime low bias of Northern Hemisphere carbon monoxide found in global model simulations, Atmos. Chem. Phys., 14, 9295-9316, https://doi.org/10.5194/acp-14-9295-2014, 2014.

Streets, D. G., Bond, T. C., Carmichael, G. R., Fernandes, S. D., Fu, Q., He, D., Klimont, Z., Nelson, S. M., Tsai, N. Y., Wang, M. Q., Woo, J. H., and Yarber, K. F.: An inventory of gaseous and primary aerosol emissions in Asia in the year 2000, J. Geophys. Res.-Atmos., 108, n/a-n/a, https://doi.org/10.1029/2002JD003093, 2003.

1544 Tandeo, P., Ailliot, P., Bocquet, M., Carrassi, A., Miyoshi, T., Pulido, M., and Zhen, Y. C.: A Review of Innovation-Based Methods to
1545   Jointly Estimate Model and Observation Error Covariance Matrices in Ensemble Data Assimilation, Mon. Weather Rev., 148, 3973-
1546   3994, https://doi.org/10.1175/mwr-d-19-0240.1, 2020.

1547 Tang, M., Liu, Y., He, J., Wang, Z., Wu, Z., and Ji, D.: In situ continuous hourly observations of wintertime nitrate, sulfate and ammonium
1548   in a megacity in the North China plain from 2014 to 2019: Temporal variation, chemical formation and regional transport,
1549   Chemosphere, 262, https://doi.org/10.1016/j.chemosphere.2020.127745, 2021.

1550 Tang, X., Zhu, J., Wang, Z., Gbaguidi, A., Lin, C., Xin, J., Song, T., and Hu, B.: Limitations of ozone data assimilation with adjustment of
1551   NOx emissions: mixed effects on NO_2 forecasts over Beijing and surrounding areas, Atmos. Chem. Phys., 16, 6395-6405,
1552   https://doi.org/10.5194/acp-16-6395-2016, 2016.

1553 Tang, X., Zhu, J., Wang, Z., Wang, M., Gbaguidi, A., Li, J., Shao, M., Tang, G. Q., and Ji, D. S.: Inversion of CO emissions over Beijing
1554   and its surrounding areas with ensemble Kalman filter, Atmos. Environ., 81, 676-686, https://doi.org/10.1016/j.atmosenv.2013.08.051,
1555   2013.

1556 Tegen, I., Lacis, A. A., and Fung, I.: The influence on climate forcing of mineral aerosols from disturbed soils, Nature, 380, 419-422,
1557   https://doi.org/10.1038/380419a0, 1996.

1558 van der Werf, G. R., Randerson, J. T., Giglio, L., Collatz, G. J., Mu, M., Kasibhatla, P. S., Morton, D. C., DeFries, R. S., Jin, Y., and van
1559   Leeuwen, T. T.: Global fire emissions and the contribution of deforestation, savanna, forest, agricultural, and peat fires (1997–2009),
1560   Atmos. Chem. Phys., 10, 11707-11735, https://doi.org/10.5194/acp-10-11707-2010, 2010.

1561 von Schneidemesser, E., Monks, P. S., Allan, J. D., Bruhwiler, L., Forster, P., Fowler, D., Lauer, A., Morgan, W. T., Paasonen, P., Righi,
1562   M., Sindelarova, K., and Sutton, M. A.: Chemistry and the Linkages between Air Quality and Climate Change, Chem. Rev., 115, 3856-
1563   3897, https://doi.org/10.1021/acs.chemrev.5b00089, 2015.

1564 Wang, S., Su, H., Chen, C., Tao, W., Streets, D. G., Lu, Z., Zheng, B., Carmichael, G. R., Lelieveld, J., Poeschl, U., and Cheng, Y.: Natural
1565   gas shortages during the "coal-to-gas" transition in China have caused a large redistribution of air pollution in winter 2017, Proc. Natl.
1566   Acad. Sci. U.S.A., 117, 31018-31025, https://doi.org/10.1073/pnas.2007513117, 2020a.

1567 Wang, S. S., Yu, Y., Zhang, X. X., Lu, H. Y., Zhang, X. Y., and Xu, Z. W.: Weakened dust activity over China and Mongolia from 2001 to
1568   2020 associated with climate change and land-use management, Environ. Res. Lett., 16, 12, https://doi.org/10.1088/1748-9326/ac3b79,
1569   2021.

1570 Wang, X., Liang, X.-Z., Jiang, W., Tao, Z., Wang, J. X. L., Liu, H., Han, Z., Liu, S., Zhang, Y., Grell, G. A., and Peckham, S. E.: WRF-
1571   Chem simulation of East Asian air quality: Sensitivity to temporal and vertical emissions distributions, Atmos. Environ., 44, 660-669,
1572   https://doi.org/10.1016/j.atmosenv.2009.11.011, 2010.

1573 Wang, X. G. and Bishop, C. H.: A comparison of breeding and ensemble transform Kalman filter ensemble forecast schemes, J. Atmos. Sci.,
1574   60, 1140-1158, https://doi.org/10.1175/1520-0469(2003)060<1140:Acobae>2.0.Co;2, 2003.

1575 Wang, X. Y., Lei, Y., Yan, L., Liu, T., Zhang, Q., and He, K. B.: A unit-based emission inventory of SO2, NOx and PM for the Chinese
1576   iron and steel industry from 2010 to 2015, Sci. Total Environ., 676, 18-30, https://doi.org/10.1016/j.scitotenv.2019.04.241, 2019a.

1577 Wang, Y. C., Li, X., Wang, Q. Y., Zhou, B. H., Liu, S. X., Tian, J., Hao, Q., Li, G. H., Han, Y. M., Ho, S. S. H., and Cao, J. J.: Response of
1578   aerosol composition to the clean air actions in Baoji city of Fen-Wei River Basin, Environ. Res., 210, 10,
1579   https://doi.org/10.1016/j.envres.2022.112936, 2022.

1580 Wang, Y. H., Gao, W. K., Wang, S., Song, T., Gong, Z. Y., Ji, D. S., Wang, L. L., Liu, Z. R., Tang, G. Q., Huo, Y. F., Tian, S. L., Li, J. Y.,
1581   Li, M. G., Yang, Y., Chu, B. W., Petaja, T., Kerminen, V. M., He, H., Hao, J. M., Kulmala, M., Wang, Y. S., and Zhang, Y. H.:
1582   Contrasting trends of PM2.5 and surface-ozone concentrations in China from 2013 to 2017, Natl. Sci. Rev., 7, 1331-1339,
1583   https://doi.org/10.1093/nsr/nwaa032, 2020b.

1584 Wang, Y. S., Li, W. J., Gao, W. K., Liu, Z. R., Tian, S. L., Shen, R. R., Ji, D. S., Wang, S., Wang, L. L., Tang, G. Q., Song, T., Cheng, M.
1585   T., Wang, G. H., Gong, Z. Y., Hao, J. M., and Zhang, Y. H.: Trends in particulate matter and its chemical compositions in China from
1586   2013-2017, Sci. China-Earth Sci., 62, 1857-1871, https://doi.org/10.1007/s11430-018-9373-1, 2019b.

1587 Wu, C. L., Lin, Z. H., Shao, Y. P., Liu, X. H., and Li, Y.: Drivers of recent decline in dust activity over East Asia, Nat. Commun., 13, 10,
1588   https://doi.org/10.1038/s41467-022-34823-3, 2022.

1589 World Health Organization (WHO): Ambient air pollution: a global assessment of exposure and burden of disease,
1590   https://www.who.int/publications/i/item/9789241511353, last access: 16 November 2023.

Wu, H., Tang, X., Wang, Z., Wu, L., Li, J., Wang, W., Yang, W., and Zhu, J.: High-spatiotemporal-resolution inverse estimation of CO and NOx emission reductions during emission control periods with a modified ensemble Kalman filter, Atmos. Environ., 236, 117631, https://doi.org/10.1016/j.atmosenv.2020.117631, 2020a.

Wu, H. J., Tang, X., Wang, Z. F., Wu, L., Lu, M. M., Wei, L. F., and Zhu, J.: Probabilistic Automatic Outlier Detection for Surface Air Quality Measurements from the China National Environmental Monitoring Network, Adv. Atmos. Sci., 35, 1522-1532, https://doi.org/10.1007/s00376-018-8067-9, 2018.

Wu, J., Kong, S. F., Wu, F. Q., Cheng, Y., Zheng, S. R., Qin, S., Liu, X., Yan, Q., Zheng, H., Zheng, M. M., Yan, Y. Y., Liu, D. T., Ding, S., Zhao, D. L., Shen, G. F., Zhao, T. L., and Qi, S. H.: The moving of high emission for biomass burning in China: View from multi-year emission estimation and human-driven forces, Environ. Int., 142, 17, https://doi.org/10.1016/j.envint.2020.105812, 2020b.

Xing, J., Li, S. W., Jiang, Y. Q., Wang, S. X., Ding, D., Dong, Z. X., Zhu, Y., and Hao, J. M.: Quantifying the emission changes and associated air quality impacts during the COVID-19 pandemic on the North China Plain: a response modeling study, Atmos. Chem. Phys., 20, 14347-14359, https://10.5194/acp-20-14347-2020, 2020.

Xu, Q., Wang, S., Jiang, J., Bhattarai, N., Li, X., Chang, X., Qiu, X., Zheng, M., Hua, Y., and Hao, J.: Nitrate dominates the chemical composition of PM2.5 during haze event in Beijing, China, Sci. Total Environ., 689, 1293-1303, https://doi.org/10.1016/j.scitotenv.2019.06.294, 2019a.

Xu, W., Sun, Y., Wang, Q., Zhao, J., Wang, J., Ge, X., Xie, C., Zhou, W., Du, W., Li, J., Fu, P., Wang, Z., Worsnop, D. R., and Coe, H.: Changes in Aerosol Chemistry From 2014 to 2016 in Winter in Beijing: Insights From High-Resolution Aerosol Mass Spectrometry, J. Geophys. Res.-Atmos., 124, 1132-1147, https://doi.org/10.1029/2018JD029245, 2019b.

Xu, Y., Huang, Z., Ye, J., and Zheng, J.: Hourly emissions of air pollutants and greenhouse gases from open biomass burning in China during 2016–2020, Sci. Data, 10, 629, https://doi.org/10.1038/s41597-023-02541-0, 2023.

Yan, X. Y., Akimoto, H., and Ohara, T.: Estimation of nitrous oxide, nitric oxide and ammonia emissions from croplands in East, Southeast and South Asia, Glob. Change Biol., 9, 1080-1096, https://doi.org/10.1046/j.1365-2486.2003.00649.x, 2003.

Yin, L., Du, P., Zhang, M., Liu, M., Xu, T., and Song, Y.: Estimation of emissions from biomass burning in China (2003–2017) based on MODIS fire radiative energy data, Biogeosciences, 16, 1629-1640, https://doi.org/10.5194/bg-16-1629-2019, 2019.

Zeng, Y., Wang, M., Zhao, C., Chen, S., Liu, Z., Huang, X., and Gao, Y.: WRF-Chem v3.9 simulations of the East Asian dust storm in May 2017: modeling sensitivities to dust emission and dry deposition schemes, Geosci. Model Dev., 13, 2125-2147, https://doi.org/10.5194/gmd-13-2125-2020, 2020.

Zhang, Z. Y., Guan, H., Luo, L., Zheng, N. J., and Xiao, H. Y.: Response of fine aerosol nitrate chemistry to Clean Air Action in winter Beijing: Insights from the oxygen isotope signatures, Sci. Total Environ., 746, 8, https://doi.org/10.1016/j.scitotenv.2020.141210, 2020.

Zheng, B., Chevallier, F., Yin, Y., Ciais, P., Fortems-Cheiney, A., Deeter, M. N., Parker, R. J., Wang, Y. L., Worden, H. M., and Zhao, Y. H.: Global atmospheric carbon monoxide budget 2000-2017 inferred from multi-species atmospheric inversions, Earth Syst. Sci. Data, 11, 1411-1436, https://doi.org/10.5194/essd-11-1411-2019, 2019.

Zheng, B., Tong, D., Li, M., Liu, F., Hong, C. P., Geng, G. N., Li, H. Y., Li, X., Peng, L. Q., Qi, J., Yan, L., Zhang, Y. X., Zhao, H. Y., Zheng, Y. X., He, K. B., and Zhang, Q.: Trends in China's anthropogenic emissions since 2010 as the consequence of clean air actions, Atmos. Chem. Phys., 18, 14095-14111, https://doi.org/10.5194/acp-18-14095-2018, 2018.

Zheng, Y. X., Xue, T., Zhang, Q., Geng, G. N., Tong, D., Li, X., and He, K. B.: Air quality improvements and health benefits from China's clean air action since 2013, Environ. Res. Lett., 12, 9, https://doi.org/10.1088/1748-9326/aa8a32, 2017.

Zhong, Q., Tao, S., Ma, J., Liu, J., Shen, H., Shen, G., Guan, D., Yun, X., Meng, W., Yu, X., Cheng, H., Zhu, D., Wan, Y., and Hu, J.: PM2.5 reductions in Chinese cities from 2013 to 2019 remain significant despite the inflating effects of meteorological conditions, One Earth, 4, 448-458, https://doi.org/10.1016/j.oneear.2021.02.003, 2021.

Zhou, M., Nie, W., Qiao, L., Huang, D. D., Zhu, S., Lou, S., Wang, H., Wang, Q., Tao, S., Sun, P., Liu, Y., Xu, Z., An, J., Yan, R., Su, H., Huang, C., Ding, A., and Chen, C.: Elevated Formation of Particulate Nitrate From N2O5 Hydrolysis in the Yangtze River Delta Region From 2011 to 2019, Geophys. Res. Lett., 49, e2021GL097393, https://doi.org/10.1029/2021GL097393, 2022a.

Zhou, W., Lei, L., Du, A. D., Zhang, Z. Q., Li, Y., Yang, Y., Tang, G. Q., Chen, C., Xu, W. Q., Sun, J. X., Li, Z. J., Fu, P. Q., Wang, Z. F., and Sun, Y. L.: Unexpected Increases of Severe Haze Pollution During the Post COVID-19 Period: Effects of Emissions, Meteorology, and Secondary Production, J. Geophys. Res.-Atmos., 127, 14, https://doi.org/10.1029/2021jd035710, 2022b.

1637   Zhou, W., Gao, M., He, Y., Wang, Q. Q., Xie, C. H., Xu, W. Q., Zhao, J., Du, W., Qiu, Y. M., Lei, L., Fu, P. Q., Wang, Z. F., Worsnop, D.

1638   R., Zhang, Q., and Sun, Y. L.: Response of aerosol chemistry to clean air action in Beijing, China: Insights from two-year ACSM

1639   measurements and model simulations, Environ. Pollut., 255, 11, https://doi.org/10.1016/j.envpol.2019.113345, 2019.

1640